Optical Properties of Capped Metallic Nanostructures, Grown on Silicon

Niall McAlinden

06128394

31st March 2010

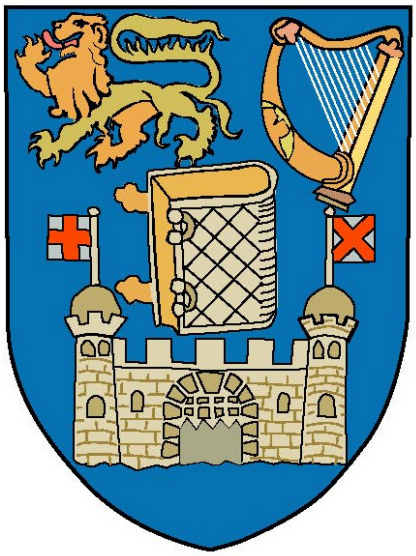

Declaration

This thesis has been submitted to the University of Dublin for examination for the degree of Doctor in Philosophy by the undersigned.

This thesis has not been submitted as an exercise for a degree to any other university.

With the exception of the assistance noted in the acknowledgments, this thesis is entirely my own work.

I agree that the Library of the University of Dublin may lend or copy this thesis upon request.

Niall McAlinden October 2010

School of Physics,
University of Dublin,
Trinity College,
Dublin

Abstract

Reflectance anisotropy spectroscopy (RAS) is a linear optical technique that measures the difference in the reflectance of two orthogonal polarisations at normal incidence. It achieves surface and interface sensitivity when the bulk material, such as a cubic semiconductor, is optically isotropic. The penetration depth of optical radiation allows RAS to probe buried interfaces. RAS has been used to probe various one-dimensional (1-D) structures grown on vicinal Si(111) surfaces under ultra-high vacuum (UHV) conditions. The RAS system response was extended into the IR, where important optical transitions occur, for both a photoelastic modulated system and a rotating sample system using a tuneable IR laser. RAS spectra of single domain Si(111)-5×2-Au, Si(557)-Au and Si(775)-Au structures showed large minima in the region around 2 eV and, in the case of Si(111)-5×2-Au a large maximum below 1 eV.

The monolayer (ML) coverage of Au required for the Si(111)-5×2-Au surface reconstruction has been extracted from the RAS response. Using the well known coverage of Au required for the Si(557)-Au reconstruction, the Au deposition rate was accurately calibrated. By analysis of the coverage required for several Si(111) vicinal off-cuts, taking into account the different step densities, a coverage for a "pure" Si(111)-5 × 2-Au surface was calculated. A value of 0.59 ML ± 0.08ML was found, in agreement with the recent work. The value supports a new three chain model for the Si(111)-5 × 2-Au surface reconstruction.

Upon deposition of small amounts of Si adatoms on the Si(111)-5 × 2-Au surface and subsequent annealing, the RAS spectra changed dramatically, as the adatom decorated "5×4" reconstruction was formed. Temperature dependent studies allowed 100% and a 0% adatom filled sites RAS spectra to be extracted. These spectra will be particularly useful for comparison with future *ab initio* optical response calculations. The optical signatures from this surface could prove to be very interesting in the study of defect induced charge density waves.

A strong optical anisotropy was also seen on the Si(775)-Au and Si(557)-Au surfaces. The RAS spectra showed a minimum around 2 eV but the maximum above 1 eV, seen on the Si(111)-5 × 2-Au surface was not present. A possible explanation is that the chain structures on these narrower terraces are more sensitive to the presence of kinks. The average length of the Au chains is expected to be significantly shorter on the Si(775)-Au and Si(557)-Au surfaces, as the kinks will terminate the Au chains more efficiently than on the lower angle offcuts, used for the Si(111)-5×2-Au studies.

The RAS response from Si(557) shows two peaks related to surface modified bulk states at 3.4 eV and 4.25 eV, and a surface state at 1.2 eV. The RAS signal was compared with preliminary *ab initio* optical response calculations. Reasonable results were found for a bulk terminated and relaxed Si(557) surface. However, the structure is known to consist of a triple step structure of approximately (112) orientation and the large terrace of the Si(111)-7×7 reconstruction. Calculations of the RAS spectra from Si(112) did not reproduce the features seen experimentally.

Elongated Pb islands with lengths of up to 430 nm and widths of 60 nm were grown on Si(557)-Au and their RAS spectra were recorded. The wires showed a strong RAS signal with a negative peak at 1.1 eV and a positive peak at 0.47 eV. The Pb islands could be capped with a-Si and their reflection anisotropy was retained, with both peaks shifted to the IR. The results showed that capping with a-Si was largely successful. The modelling of the RAS response was less successful. A nanoantenna approach gave reasonable values of the length of the Pb islands, using the wavelength of the maximum. Other models, which attempted to predict the line shape, could reproduce either the minimum or maximum accurately but not both. However, these models neglect both quadrupolar effects and dipole-dipole interactions between islands. The sensitivity of the RAS response to the detail of the island structure indicates that RAS could be a powerful probe of plasmonic structures if a suitable theoretical model can be developed.

Acknowledgments

First and foremost I would like to thank my supervisor Prof. John McGilp. He worked closely with me throughout the four years of my thesis, giving advice and guidance when needed. He always encouraged discussion and debate within the group which lead to a great working environment. I will miss the weekly coffee meetings where new results and ideas were shared and openly talked about.

I would also like to thank Dr. Conor Hogan for all the computational results on the Clean Si(557) surface. When he was told that I was submitting in 4 months he rose to the challenge, read up on a surface he had not studied before, worked through several problems with the code and in the end produced some nice results. I wish him all the best with the Gold modified Si(111) surfaces.

The IR-RAS results would not have happened without the help of Dr. Jing-Jing Wang. He helped setting up the DFG laser and always had good advice on alignment of the optics.

The whole group who I have worked with over the last 4 years all have had an input into this work. Lee and Julie for showing me the basics of UHV, and sample mounting and cleaning. Karsten for introducing me to the RAS system. John for helping me any time the UHV system was acting up, Lina for always giving a helping hand with the laser and Chris for his help with the optical analysis of almost everything. As with any thesis there are countless others who have had an input so I hope I don't forget anybody; Cormac, Nikos, Brian, Declan, Dannel, Martin, Iggy, Ming, Nina, Rugerro and the many summer and 4th year students that have come through the group in the four years I've been here.

I am very grateful of all the support I have received from the electronics and mechanical work shops in the school of physics. Nigel deserves special credit for getting everything back working after a flood in the lab in 2008. Joe, Dave, Mick, and Ken have also provide valuable help and advice during this thesis. And thanks to John Kelly for always making me laugh and solving any problems I asked him to.

No thesis would be possible with out all the help and encouragement received from outside of physics, I would like to thank my family, my mum and dad, Rita and Harry, and my sisters, Ciara and Amy and all my friends who ran, cycled, swam or drank (some who did all four) with me throughout the four years. I would like to especially thank the Triathlon club in Trinity for introducing me to so many new friends.

I would also like to thank the two funding bodies who supported this work, the IRCSET and SFI.

Publications

R. Verre, K. Fleischer, S. Sofin, N. Mc Alinden, J. F. Mc Gilp, and I. V. Shvets. In situ characterization of one-dimensional plasmonic Ag nanocluster arrays. *Phys Rev B*, Accepted Jan 11, 2011.

N. McAlinden and J.F. McGilp. New evidence for the influence of step morphology on the formation of Au atomic chains on vicinal Si(111) surfaces. *EPL*, **92**, 67008, 2010.

N. McAlinden and J.F. McGilp. Using surface and interface optics to probe the capping, with amorphous Si, of Au atom chains grown on vicinal Si(111). *Journal of Physics: Condensed Matter*, 21(47): 474208-13, 2009.

J. Jacob, N. McAlinden, K. Fleischer, S. Chandola, and J.F. McGilp. Reflectance anisotropy studies of 5×2-Au structures grown on Si(111) surfaces with different step formations. *Physica Status Solidi C*, 5(8): 2569-72, 2008.

List of acronyms

0-D	0-Dimensional
1-D	1-Dimensional
2-D	2-Dimensional
AES	Auger Electron Spectroscopy
AFM	Atomic Force Microscopy
a-Si	Amorphous Silicon
CDW	Charge Density Wave
DFG	Difference Frequency Generator
DFT	Density Functional Theory
FTIR	Fourier Transform Infrared
GW	Greens function and screened interaction
IR	Infrared
l-N_2	Liquid Nitrogen
LDA	Local Density Approximation
LEED	Low Energy Electron Diffraction
ML	Monolayer
MLWA	Modified Long Wavelength Approximation
MOKE	Magneto Optical Kerr Effect
OPA	Optical Parametric Amplifier
PBN	Poly-Boron Nitride
PEM	Photo-Elastic Modulator
RAS	Reflection Anisotropy Spectroscopy
RegA	Regenerative Amplifier
RFA	Retarding Field Analyser
SDW	Spin Density Wave
SEM	Scanning Electron Microscopy
STM	Scanning Tunneling Microscopy
STS	Scanning Tunneling Spectroscopy
TE	Thermoelectric
UHV	Ultra High Vacuum
UV	Ultraviolet
VLS	Vapour Liquid Solid

List of element abbreviations

Ag	Silver
Ar	Argon
As	Arsenide
Au	Gold
Ba	Barium
C	Carbon
Ca	Calcium
Cd	Cadmium
Cu	Copper
F	Fluorine
Ga	Gallium
H	Hydrogen
Hg	Mercury
In	Indium
K	Potassium
Mg	Magnesium
N	Nitrogen
Na	Sodium
O	Oxygen
Pb	Lead
Pr	Praseodymium
Si	Silicon
Te	Tellurium
Xe	Xenon
Zn	Zinc

Contents

1 Introduction

1.1 Opening remarks

As modern industry drives for ever smaller and faster electrical components they encounter both physical and processing limitations. The physical problems in some cases are related to strange new physics due to the reduced dimensionality of the structures [1]. For example Ag nanodots ($\sim$ 20 atoms) grown on Si(111)-3 $\times$ 1-Ag (figure 1.1) [2, 3] are not metallic, but are semiconducting [4]. The processing limitations are related to the difficulties in actually producing features that are smaller than $\sim$ 30nm.

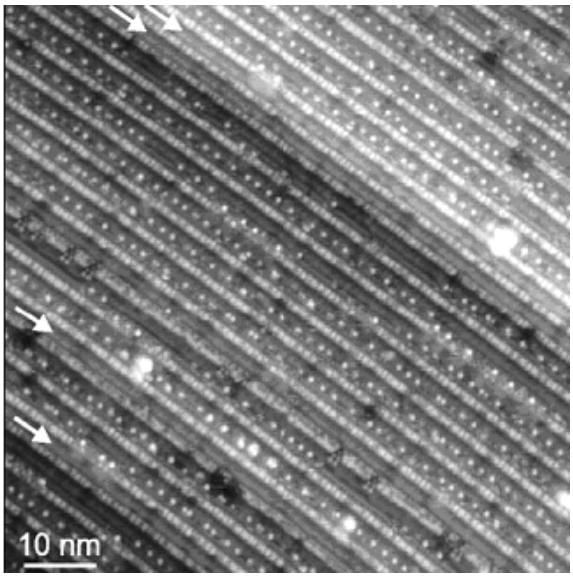

Figure 1.1: Ag Nanodots on a Si(111)-3 $\times$ 1-Ag (after [4]).

These nanostructures have a high surface to volume ratio. A 1 cm cube of Ag contains about 6×10^{22} atoms. Of these 7×10^{15} are surface atoms, or 1 in 10^7. In the silver nanodots the 20 atoms are in a single atomic layer, so they are all surface atoms. This problem is unavoidable, but with some clever device design these strange properties can be used to make devices that are faster than conventional electronics [5]. However, if the surface of the device is changed it can drastically alter the properties of the device. This is a major problem as exposure to the ambient will drastically alter the surface of most materials. To avoid these issues structures are often grown under ultra high vacuum (UHV) conditions at pressures $\leq 10^{-10}$ mbar. Structures can then be capped with a material to prevent the corrosion and contamination by the ambient on removal from the growth chamber.

After capping it is important to find out if the shape, composition or properties of

the structures have been altered in any way. Conventional surface science techniques, like scanning tunneling microscopy (STM), atomic force microscopy (AFM) and low energy electron diffraction (LEED), work extremely well with uncapped nanoscale systems, but due to the low penetration depth of electrons they cannot be used to study capped nanostructures. However, photons have a large penetration depth (figure 1.2). This means that optical techniques can "look under" the cap and provide important information about the properties of buried structures, provided the signal can be distinguished from the underlying bulk [6–9]. In addition, electrical conductivity can be measured optically [10], thus avoiding the contact problem when characterising nanostructure conductivity.

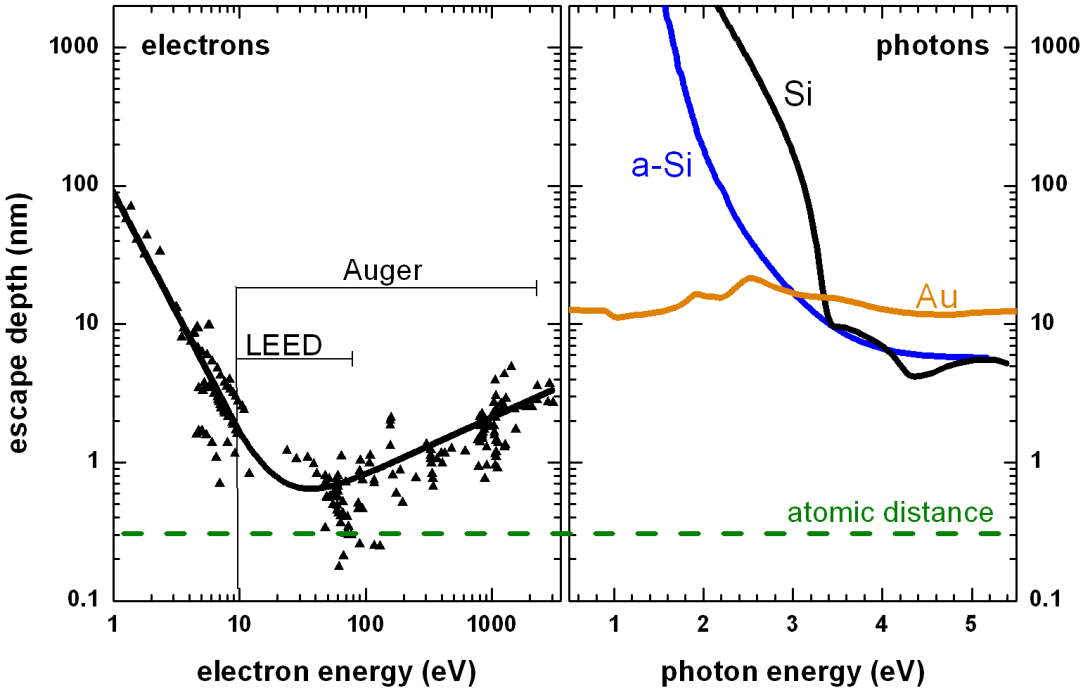

Figure 1.2: A comparison of escape depth between optical and electron based techniques (after [9]).

The processing limitations relate to the finite resolution that can be achieved by using photolithography. Photolithography is the most prominent technique for creating devices. It works by using a polymer that changes when exposed to ultraviolet (UV) light. Areas exposed to the light are then washed off and the rest is used as a mask to control the implantation of dopants, oxide removal etc. This technique has a minimum size due to the diffraction limit of light. By using clever techniques [11, 12] light of $\sim$ 190nm can produce features of about $\sim$ 30nm. This however seems to be a tough limit to get past. There is a push to use shorter wave-

length light or electrons but it is unclear what resolution this will be able to achieve in practice. A way around this problem is to use a technique called self-assembly or bottom up production [13]. This is when nanostructures grow themselves. An example of this is deposition onto a stepped surface. Generally, the most energetically favorable position for adatoms to sit is at the step edge [14]. This method can even produce single atomic chains which are very interesting model systems for 1-dimensional (1-D) physics [15] (chapter 2).

The main optical technique that was used during this project to study nanoscale surfaces and interfaces was reflection anisotropy spectroscopy (RAS), a linear optical technique. It uses symmetry to achieve surface and interface selectivity. RAS measures the difference in reflectivity between two orthogonal polarisations at near normal incidence and thus can be used to study surfaces and interfaces with in-plane optical anisotropy [16]. If the bulk is isotropic only the surface will produce a signal. A comprehensive review of RAS has been published recently [17]. Two different experimental set-ups were used. The first technique used a photo-elastic modulator PEM to effectively switch the polarisation of the light at a frequency of 56 kHz. The other technique used a sample rotation stage that spun at 20 Hz. Both techniques have advantages and disadvantages depending on the spectral range [18]. A detailed discussion of RAS is included in chapter 4.

1.2 Scope of the thesis and overview of the literature

The scope of this project is to produce and characterise wires grown by self-assembly that are less than 10 nm in two of their dimensions and then to investigate how capping changes their properties. Physics of *quasi* 0-, 1- and 2-dimensional material is an exciting area of research and with new processing techniques it has become possible to create systems that are at the limits of a single atom [19], single atomic chain [20] or single atomic layer (monolayer, ML) [21].

By depositing metal on a Si substrate many low dimensional structures can be formed. The clean Si surface has dangling bonds which will increase its surface energy. The surface will reconstruct to try to minimise these dangling bonds and hence surface energy [22]. When metal atoms are introduced they will interact strongly with the dangling bonds and cause different surface reconstructions to form [23]. Depending on the metal, Si surface orientation, amount of metal deposited and annealing temperatures surfaces that have *quasi*- 1- and 2-dimensionality can be formed. Of interest for this project are the 1-dimensional structures. Examples of these are Si(111)-5 $\times$ 2-Au [24], Si(111)-4 $\times$ 1-In [25] and Si(111)-3 $\times$ 1-Ag [26].

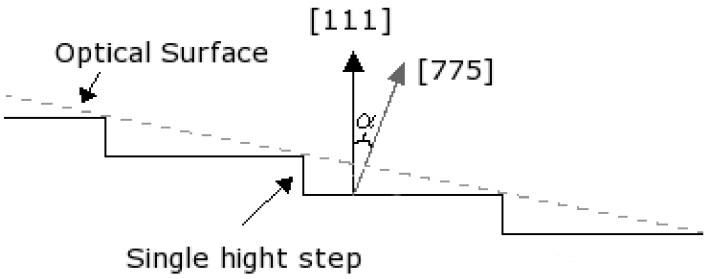

Figure 1.3: A simplistic picture of a vicinal surface, where α is the vicinal angle. In the example drawn, Si(775), the angle α is $\sim 8.5°$ in the $[11\overline{2}]$ direction. The dotted line represents the optical surface.

When grown on singular Si(111) these systems are multi-domain, because each of the 3 surface domains that are rotated from each other by 120° have equal energy of formation. For large area probes, including RAS, macroscopic averaging will result in an overall 3-fold symmetry, hiding the lower symmetry of the individual domains. Vicinal substrates cut close to the [111] direction (see figure 1.3) can produce perfectly aligned step structures with suitable heat treatment [27, 28] (figure 1.4) . Deposition can then lead to a single domain, as the domain aligned with the steps generally has a lower energy of formation [29].

The systems of interest to this project were Au on Si(111) and its vicinal off-cuts. Several structures can be formed on this surface depending on off-cut angle, annealing temperatures and Au coverage. The Si(111)-5 × 2-Au and its related structures are particularly interesting due to the one-dimensional nature of the surface states [30]. This family of surfaces has been quite controversial. Si(557)-5 × 1-Au was initially claimed to show spin-charge separation [31], but this was found to actually be a spin split state [32]. Si(111)-5 × 2-Au was shown to have adatoms sitting on top of its chains [33]. These adatoms were initially thought to be Au [34] but have now been shown to be Si [35, 36]. Also, most interestingly, there is ongoing debate about the structure of the Si(111)-5 × 2-Au surface, with recent papers claiming that both a 2-chain [37] and 3-chain model [24] are energetically stable and match experimental data. Only one RAS study of Si(111)-5 × 2-Au has been reported previously [38] (figure 1.5) and more detailed studies are presented in chapter 5. It has also been shown recently on the Si(111)-4 × 1-In surface that RAS can provide new information which can help in determining the surface structure. It can achieve this as the optical transitions involve both valance and conduction states, giving additional sensitivity over conventional surface techniques [25].

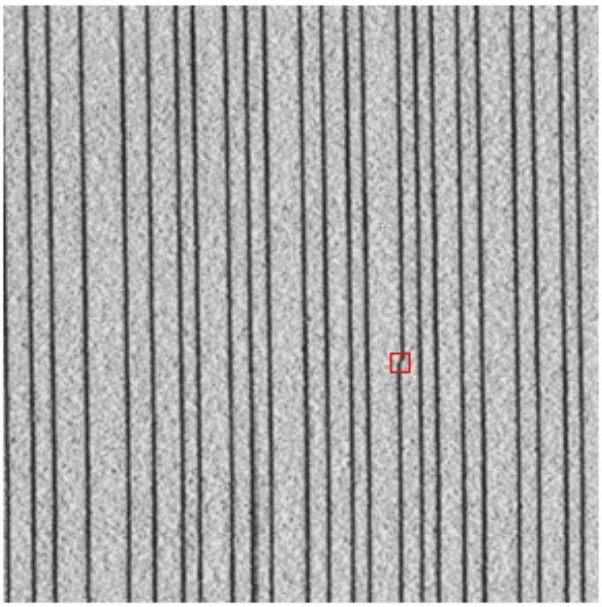

Figure 1.4: Step array on a Si(111)-7 × 7 surface. The image contains a single kink in about 20,000 step edge sites; the location is highlighted by the red square. The image is 340 × 390 nm. (after[28]).

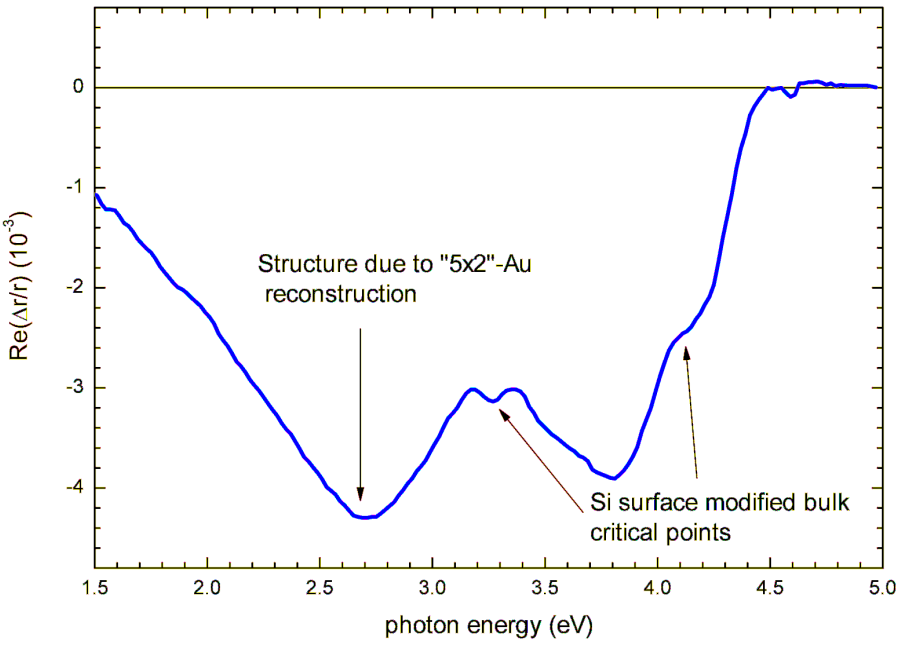

Figure 1.5: RAS spectra from Si(111)-5 × 2-Au (after [38]). The surface modified bulk critical points for Si are marked, 3.4 eV and 4.25 eV. The structure at 2.7 eV is believed to come from the 5 × 2 reconstruction.

Another method of producing 1-dimensional structures is to deposit on a substrate that has a strong anisotropic diffusion. Atoms can diffuse in one direction only and long metallic islands can be formed. Two examples of this type of growth are Ag deposited on Si(111)-3×1-Ag [7] and Pb deposited on Si(557)-5×1-Au [39]. Various attempts have been made to model the infrared (IR) optical anisotropy of these metallic structures including an antenna model [40], anisotropic Drude dielectric model [7] and a Bruggeman type model [41]. These models are discussed further in chapter 7.

Finally capping such structures with amorphous silicon (a-Si) is explored. It was hoped that depositing about 10 nm of a-Si would protect structures from the ambient. Si forms a self-limiting oxide of about 1 nm in thickness after a few days exposure to the atmosphere, preventing corrosion and contamination of the sample. a-Si is chosen as a capping material as it is transparent in the IR, the region where effects due to metallic conductivity changes are expected. Also, the band gap of a-Si ($\sim$1.5 eV) indicates that there should be little or no coupling between the metallic states of the wires and the capping layer. Of particular interest is that recent surface x-ray diffraction studies have shown that capping the Si(111)-5×2-Au structure with a-Si does not perturb the position of the Au atoms [42].

2 Physics in one dimension

One dimensional (1-D) physics has captivated theoretical physicists for generations. Many problems can be solved analytically in 1-D that do not have an analytical solution in higher dimensions. While a true 1-D material is purely a theoretical construct several materials approaching 1-D can now be routinely manufactured in the lab. These materials have hinted at some strange new properties of materials, such as exotic types of superconductivity and unusual *quasi*-particles. It is very important that these materials are understood and hopefully new technologies will emerge due to their unique properties.

2.1 Properties of metals in 1-D

In two and three dimensions electrons can easily avoid each other but in 1-D they can't and become strongly correlated. This implies that the single electron Fermi liquid model for weakly interacting electrons is no longer adequate and must be replaced by models involving collective excitations, such as the Tomonaga-Luttinger liquid model [43, 44]. Even without considering these collective excitations, physics in 1-D will be drastically different to physics in higher dimensions, as the next four sections outline.

2.1.1 1-D density of states

In solid state physics, the density of states of a system is the number of states at each energy that are available to be occupied. The density of states is related to the curvature of the bands at that particular energy. The flatter the curvature the greater the density of states. For a 3-D free electron metal the density of states is given by:

$$g(E)\ dE = \frac{1}{2\pi^2}\left(\frac{2m}{\hbar^2}\right)^{3/2}\sqrt{E}\ dE \tag{2.1}$$

where $g(E)$ is the density of states and m is the mass of the electron. For a 1-D free electron metal the density of states is drastically different and is given by [45]:

$$g(E)\ dE = \frac{1}{2\pi^2}\left(\frac{2m}{\hbar^2}\right)^{1/2}\sum_i \frac{n_i H(E-E_i)}{(E-E_i)^{1/2}}\ dE \tag{2.2}$$

where H is the Heaviside step function ($H(x) = 0$ when x is negative, $H(x) = 1$ when x is positive). E_i is the onset energy for each energy level and n_i is the degeneracy factor. Figure 2.1 shows the difference between the 3-D and 1-D free electron density of states. The 3-D density of states simply shows a $\sqrt{E}$ behavior,

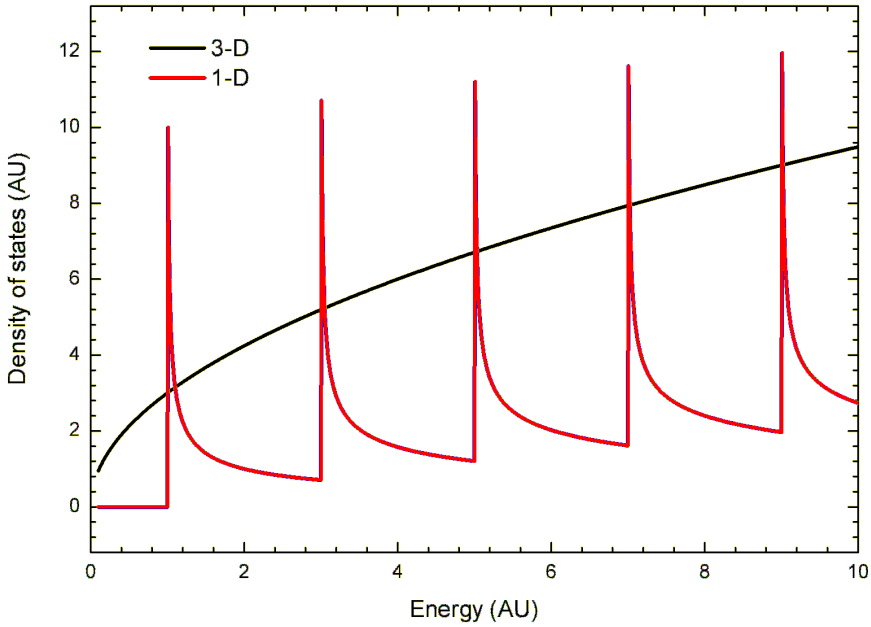

Figure 2.1: The 3-D free electron gas density of states compared to the 1-D free electron gas density of states

while 1-D density of states shows a series of spikes called van Hove singularities. These van Hove singularities are important in optical spectroscopy as they will give strong absorption spikes at energies where an electron can be promoted from one van Hove singularity to the next. They will also show strong fluorescence as electrons decay down from one singularity to the next. This 1-D density of states behavior has been recorded for single wall carbon nanotubes [46].

2.1.2 Peierls instability

The best way to describe the Peierls instability is to consider a system with just one parabolic metallic band. If the atoms of this system are arranged in a periodic 1-D wire, with lattice constant a, they will have a band structure similar to figure 2.2 a. However Peierls showed that every 1-D system can reduce its total energy if the periodicity of the system alters slightly [47]. The simplest Peierls instability is a doubling of the atomic periodicity along the chain length, with the lattice constant doubling to $2a$. This causes a back-folding of the bands and a gap opening (figure 2.2 b). The energy gain is shown by the light gray shaded area. This instability means that an unsupported 1-D chain of metallic atoms will always have a semiconducting ground state. The transition is most favorable when electrons are close to their ground state and as such is normally seen at low temperature. However,

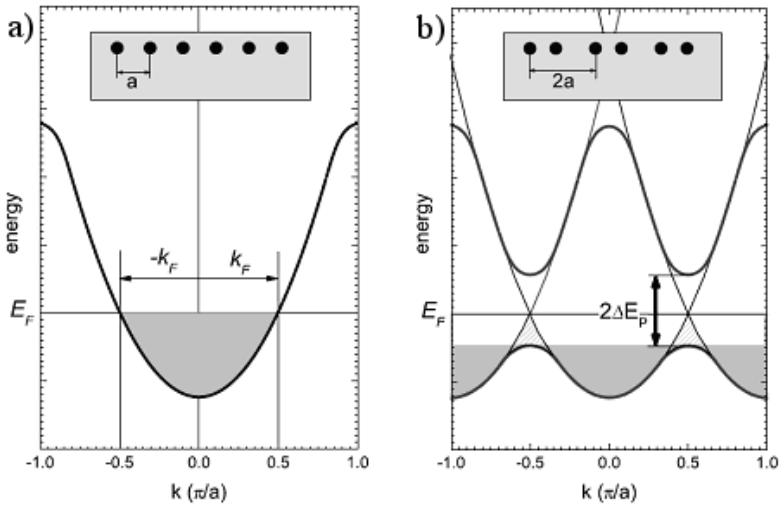

Figure 2.2: A schematic of the Peierls instability. a) A half-filled parabolic band structure for a 1-D chain of electrons. b) The same chain after a periodicity doubling along the chain direction, which induces a back-folding of the band structure with a band gap opening. The light gray shaded area shows the energy gain associated with the transition.

if the metallic chain is supported on a substrate, such as Si, this transition can be suppressed due to the interaction of the chain with the rigid lattice of the substrate, and will only be seen at very low temperatures. The transition between room temperature Si(111)-4×1-In and low temperature Si(111)-8×2-In is an interesting example of the complexity of Peierls transitions in surface structures [48–51].

2.1.3 Charge density waves

Charge density waves (CDWs) are a general term for a sinusoidally modulated charge distribution in space. A Peierls instability is one example of a CDW, but most charge density waves will form by a mechanism that is not strictly a Peierls mechanism. A Peierls distortion is strictly a phonon-electron interaction (involving a single metallic band) [47], while many CDWs can be induced by defects and can involve several bands and interchain interactions. A CDW will have the same effect as a Peierls distortion in that it will cause the 1-D metallic chain to have an insulating ground state. Unfortunately, CDWs and Peierls distortions prohibit the formation of a ground state Tomonaga-Luttinger liquid. The doubling/tripling of the periodicity in the Si(553)-Au system at low temperature [52, 53] is one example of CDW formation, while the adatoms on Si(111)-5×2-Au are an excellent example of defect mediated CDW formation [24, 54, 55]. A variation of a charge density wave is a spin density

wave (SDW) where the spin will be sinusoidally modulated in space. SDW are seen in several 1-D materials such as Bechgaard salts [56–58] and high T_c superconductors [59]. They have also recently been predicted to occur on Si(553)-Au and Si(557)-Au [60], but have not been observed.

2.1.4 Ballistic electron transport

Ballistic transport is the motion of electrons with negligible electrical resistivity due to scattering through the material. It occurs for materials where the mean free path of the electron is significantly greater than the length of the wire containing the electron. When this happens the resistance in the wire will depend solely on the contact resistance. The contact resistance G_c can be calculated and is a universal constant for a 1-D conductor. The number of transverse modes in the wire is given by $N = 2W/\lambda_f$ where W is the width of the wire and λ_f is the Fermi wavelength. Each mode can carry a current of $I_m = Ve^2 g_m \, \upsilon_m$ where V is the voltage between the two ends of the wire, e is the charge of an electron, g_m is the density of states of the mode and υ_m is the group velocity of the mode. The group velocity is related to the density of states by $g_m = 1/(\hbar \upsilon_m)$. Substituting into the previous equation gives:

$$I_m = \frac{e^2}{\hbar} V \tag{2.3}$$

As new modes are introduced the conductance will jump in steps of $2e^2/\hbar$ (the factor of two is introduced because each mode can carry two electrons, one up-spin and one down-spin). This result has been shown experimentally for several different types of samples [61–63].

2.1.5 Spin-Charge separation

If a ground state Tomonaga-Luttinger liquid could be formed what would its properties be? There are several interesting phenomena that would be seen. For example, when an electron is removed from the system, for example by photoemission, it forms a positively charged hole with a spin exactly opposite to the electron that was removed. In a Tomonaga-Luttinger liquid the charge associated with the hole and the spin associated with the hole will have different group velocities and will separate into two *quasi* particles, a spinon and a holon. Figure 2.3 gives two different pictures of this spin-charge separation, one for delocalised electrons and one for localised electrons. This behavior can lead to strange transport properties, as detailed in the comprehensive review by Voit [64]. Some evidence for Tomonaga-Luttinger liquid behavior has been seen in photoemission experiments on Bechgaard salts [65],

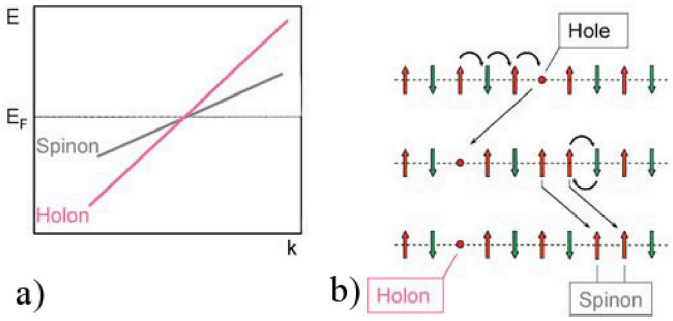

Figure 2.3: Two models of spin-charge separation. a) The delocalised Tomonaga-Luttinger liquid model predicts that a partially filled band will split into a spinon and holon band, that are degenerate at the Fermi level. b) The localised Hubbard model gives a clearer picture of what is happening, and consists of a antiferromagnetic array of electrons. When a hole is created by photoemission a neighboring electron can hope into it, in this case causing the hole to move to the left. This leaves two electrons of equal spin beside each other creating a spinon (after [15]).

carbon nanotubes [66, 67], indium atomic wires [68] and chains of $PrBa_2Cu_4O_8$ [69]. The evidence for non-Fermi electron gas behavior comes from the width (lifetime) of angle resolved photoemission transitions [70].

2.1.6 Fermi contours, a measure of 1-D character

The Fermi surface of a crystal structure is an abstract boundary in reciprocal space, marking the boundary between the filled and empty electron states. Its shape depends on the periodicity and symmetry of the crystalline lattice, and on the electron density, which determins the length of the Fermi vector. Figure 2.4 shows the Fermi surface for a 3-D noble metal.

For a 2-D metal, the Fermi surface becomes a circle with necking at points were it meets neighboring circles and, in a 1-D metal, the surface becomes a line. A slice of these Fermi surfaces can be measured using angle resolved photoemission [70, 71], referred to as a Fermi contour. In surfaces where there is an array of 1-D chains, with the possibility of interchain interactions with neighboring chains the system has a dimensionality somewhere between 1 and 2. This will show in the Fermi surface as deviations from a straight line in the Fermi contours [15] (figure 2.5). By studying the degree of a deviation from a straight line, the ratio of the intrachain to interchain interaction strength can be calculated.

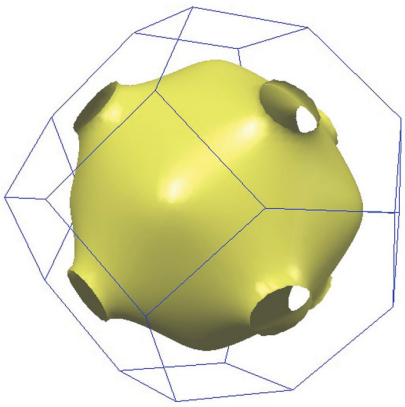

Figure 2.4: The Fermi surface for a perfect face centered cubic noble metal. It consists of a sphere with necking points, where the sphere will be in contact with neighboring spheres.

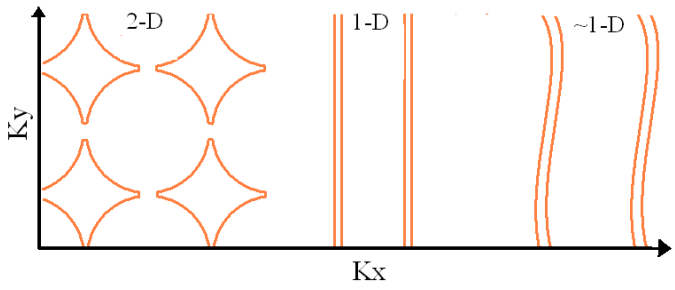

Figure 2.5: The Fermi contours for a 2-D metal with a single band, a 1-D metal with 2 spin split bands, and an almost 1-D metal with 2 spin split bands.

2.2 Examples of 1-D systems

Material scientists have been able to produce a large variety of inorganic and organic compounds, which exhibit highly anisotropic electronic properties and effectively behave as 1-D conductors. They range from organic polymers to superconductors. Some of these materials are discussed here and, where their anisotropic optical properties have been studied, these will also be discussed.

2.2.1 Bechgaard salts

Bechgaard salts were discovered in 1979 by Klaus Bechgaard [72]. They showed superconductivity at very low temperatures and had highly anisotropic conductivity at room temperature. They consist of a tetrathiafulvalene building block (figure 2.6) which is a planar molecule. In a crystal the tetrathiafulvalene molecules will stack and inorganic ions can form chains between the stacks. They show several instabilities as they are cooled and can form both CDWs and SDWs. Reflection properties of some of the Bechgaard salts have been studied both along the stack direction and perpendicular to it, but not with RAS [56, 58, 73]. These reflectance properties show a huge anisotropy, equivalent to a RAS signal of $\geq$500, although it is a bulk effect compared to the surface effect seen on metallic chains on Si surfaces. The reflectance measurements were carried out from the far IR to the visible (0.001 eV to 2 eV) and were able to detect details about the metal-to-insulator CDW transition that occurs at around 100 K [73] and metal to insulator SDW transition that occurs at around 10 K [56, 58]. Details about the vibrational modes in the salt were also studied. Bechgaard salts normally have a intrachain to interchain coupling strength of $\sim$10 indicating that they still have significant 2-D/3-D character.

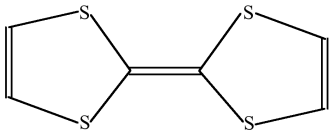

Figure 2.6: The main building block for a Bechgaard salt. When the molecules are crystalised they stack leaving channels where the cations can sit and form long conducting chains.

2.2.2 Conducting polymers

Conducting polymers are considered a key discovery of the 20th century. Heeger, MacDiarmid and Shirakawa were awarded the Nobel prize for their work on con-

ducting polymers in the year 2000. They have the potential to combine the positive properties of polymers, such as ease of processing, flexibility and elasticity, with electrical conductivity. They also show some 1-D metallic properties, as they have much greater conductivity along the polymer chain than perpendicular to it. However, there is significant interchain interaction, which suppresses the formation of a truly 1-D metal. Conducting polymers show a temperature behavior more like a disordered metal than a true 1-D conductor [74]. In some systems, where the polymer is made into thin wires ∼30 nm in diameter, CDW have been seen and can be used to create interesting switching devices [75]. Reflectance and absorption studies have been completed on some conducting polymers [76, 77] and have given some new insights into the metal-to-insulator transition that is observed at high doping levels.

2.2.3 Carbon nanotubes

Carbon nanotubes can be either metallic and semiconducting, depending on how they are "wrapped" or more correctly their chiral vector. While this means that there is a wealth of new possible materials with different electronic properties, it creates problems in their manufacture as it is difficult to produce a single chirality of nanotube in significant quantities. The presence of multiwall nanotubes and nanotube bunching will also affect the properties of the material. An interesting effect seen in carbon nanotubes is ballistic conduction [61, 62, 78]. Nanotubes have a 1-D density of states with strong optical absorptions and fluorescence between van Hove singularities [46, 79]. Little reflectance difference or RAS work has been completed on carbon nanotubes, as they are almost perfect blackbody absorbers [80], and they are difficult to align. Some reflectance difference data have been collected by using very strong magnetic fields to align nanotubes [81]. Using their data it is possible to predict the RAS spectra from aligned carbon nanotubes (figure 2.7) but, as is discussed in the paper, their data could be affected by the strong magnetic fields used to align the nanotubes. Although the reflectance may be almost 100% polarised below 0.5 eV, the low reflectivity of the perpendicular component may limit the signal-to-noise ratio. The spectra were fitted by Kamaras *et al* using a DrudeLorentz oscillator, where it was found that each of the Lorentz oscillations was shifted in the perpendicular case compared to the parallel case. When the difference between the perpendicular and parallel case is taken this shift producess the two derivative structures seen in the RAS simulation.

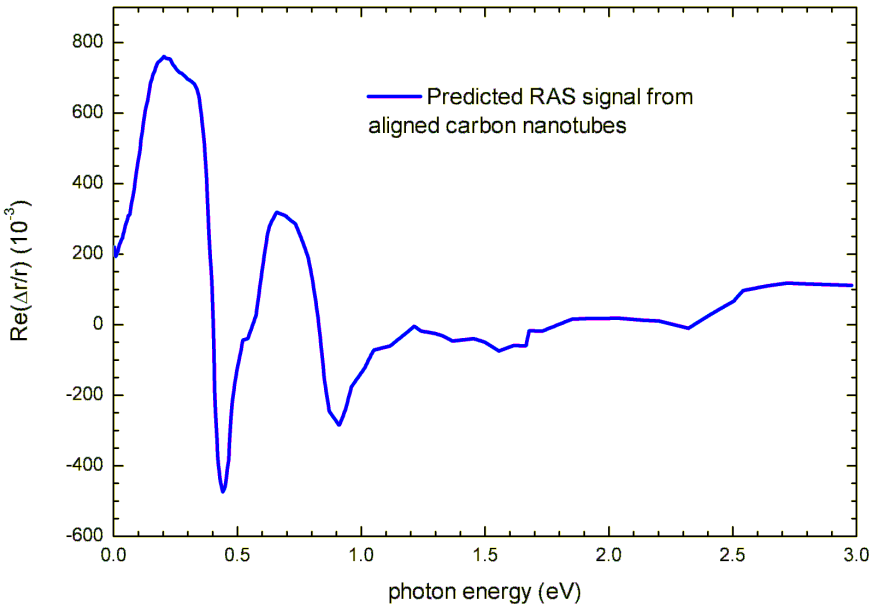

Figure 2.7: Predicted RAS signal from aligned single wall nanotubes, data was taken from [81].

2.2.4 Wires grown by the vapour liquid solid method

The vapour-liquid-solid (VLS) growth method involves growing very thin nanowires by depositing droplets of metal onto a substrate, then increasing the vapour pressure of the material to be deposited. The metal acts as a nucleation site/catalyst for the material and long wires are produced with a diameter roughly equal to the size of the original droplet [82]. This method produces long wires aligned vertically from the substrate and, because of this geometry, no reflectance spectra have been published for light polarised parallel and perpendicular to the wires. The properties of these wires can be quite different from the bulk material. For example, Si nanowires with a diameter of around 2 nm depending on the crystallographic orientation of the wire may have a direct band gap [83]. Technologically, this is a very promising approach. This method, however, is currently limited to wires of $\geq$ 2 nm, which means that they do not show significant 1-D metallic properties.

2.2.5 Wires pulled using a break junction method

By crashing an STM tip into a metal surface and slowly pulling it out, a single atomic chain several atoms long can be created (figure 2.8), sometimes called a break junction. As the wire is pulled the conductance is found to go down in discrete steps. These steps in conduction are related to the points where the chain

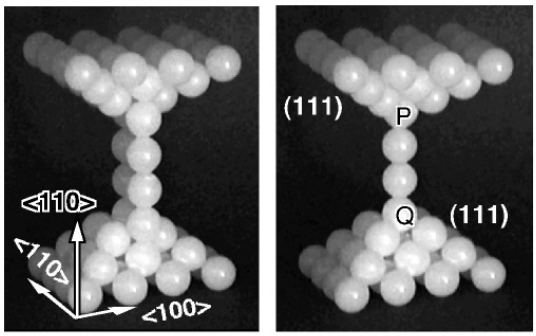

Figure 2.8: Schematic of two STM break junctions a double atomic wire (left) and a single atomic wire (right). The wires are created by crashing a STM tip into a metallic surface and slowly withdrawing it (after [86])

looses a conduction path, for example going from a triple to double atomic wire or a double to a single atomic wire. This phenomena is called quantised conductance and is related to ballistic conductance discussed previously. The field is dominated by the creation of Au wires [63, 84] but other metals such as Fe and Cu have also been studied [85]. These short wires are surprisingly stable and will survive different ambient conditions including liquids and atmospheric pressure. They can survive incredibly high current densities due to the ballistic conduction of electrons through the wire. Instabilities are seen in these wires and they can never be more than a few atoms long before breaking. However, they provide some very interesting test systems. Agrait *et al* have published a comprehensive review of the topic of break junctions [63]. Optical properties of these wires would be extremely difficult to study as the wires are created individually. It may be possible in the future to create arrays of these wires using a method similar to that of Kiguchi *et al* [84], allowing their optical properties to be studied.

2.2.6 Metals on stepped semiconductor surfaces

When metals are deposited on a stepped semiconductor surface they can form arrays of atomic wires by self assembly at the step edges. The metallic bands of the atomic wires may sit in the band gap of the semiconductor and hence their bands may be decoupled from the bulk semiconductor bands. This allows 2-D surface states to be formed. The chain-like structure of the atomic wires means that the surface bands may have an almost 1-D nature and, by changing the distance between the steps (and hence atomic chains) on the surface, the ratio of intrachain to interchain coupling strength can be increased to greater than 100 [30]. The system that has

received most attention, due to the relative ease by which it can be produced and the vast array of possible stepped Si(111) surfaces, is the Si(111)-Au system. Aspects of this system are discussed extensively in chapter 5 and so only some details of the surfaces will be given here.

Si(111)-5×2-Au is an extensively studied, but controversial system which consists of a double or triple chain chain of Au atoms and a stable Si honeycomb chain on a Si(111) surface [24]. The surface is decorated with Si adatoms that sit on top of the chains in a 5×4 lattice [36, 55]. Only about 50 % of the lattice sites are ocupied and the surface segregates into regions covered with adatoms and regions without adatoms. From angle resolved photoemmision (ARPES) results it has been established that the covered regions are semiconducting with a band gap of about 0.6 eV and the uncovered regions are metallic [55, 87]. The adatoms appear to cause a CDW to form on the chains in a similar manner to the defect mediated CDW formation on the Si(553)-Au surface [88] or the absorbate induced CDW that is formed when Na is deposited on Si(111)-4×1-In [89]. The optical response of Si(111)-5×2-Au is discussed in detail in chapter 5.

The Si(557)-Au system has received a lot of attention due to the paper by Segovia *et al* [31] which mistakenly attributed the spin-orbit splitting of the S_1 and S_2 bands as spin-charge separation [32]. Si(557)-Au has a intrachain to interchain coupling strength that is greater than 60 [30]. The surface structure (figure 5.26) consists of a single Au chain in the middle of a terrace, and has some perfectly 1-D electron states. The behavior of the S_1 and S_2 bands is quite complex. It is believed that the S_1 band undergoes a phase transition at around 260 K but the mechanism for this is not understood. The S_2 state is reported as having a small band gap at room temperature [90, 91] but, other ARPES experiments have contradicted this band gap opening [30, 92] so there is still significant work to be done to understand this system. STM images of the surface at room temperature show two bright chains running parallel to the steps [93]. One of the chains, associated with a Si adatom chain, appears to have a ×2 periodicity even at room temperature, while the other, associated with a chain of dangling bonds from the step edge, shows no distortions [90, 93, 94]. Upon cooling below ∼270 K this second chain doubles its periodicity and forms a CDW [95]. Defects in this system play a significant role in its long range transport properties and as such four point probe techniques have not been able to confirm the CDW phase transitions [71]. At very low temperatures this surface is predicted to have a antiferromagnetic ground state, as a SDW forms with every second adatom having spin up and the other having spin down. A similar

SDW is thought to form on the step edge [60]. The RAS spectra from Si(557)-Au are discussed in detail in section 5.6.

The Si(553)-Au system has received a lot of interest in the last 5 years [96]. This reconstruction forms when 0.48 ML of Au is deposited on the clean Si(553) surface [97]. The structure consist of two Au chains running parallel to the step edge [98]. The surface has 3 fractionally filled bands (called S_1, S_2 and S_3) that cross the Fermi energy. The surface shows some wiggling in the Fermi contours, indicating that there is significant interchain coupling. Two of the bands that cross E_f are spin-orbit spit bands, S_1 and S_2, similar to Si(557)-Au. It is thought that the third band, S_3, is related to a row of unsaturated dangling bonds on the terrace [53]. When this surface is cooled several distortions are seen. STM images show a $\times 3$ periodicity along the step edge and a $\times 2$ periodicity on the terrace [53]. LEED images show a $\times 3$ periodicity indicating a lattice distortion, but this has not been confirmed [53, 71]. four point probe measurements clearly show a metal to insulator transition occurring at around 150 K [71]. Defects in this system have a profound effect on the the CDWs seen in STM. Their transition temperature and their correlation length are affected, and the defects can pin CDW fluctuations [88, 96]. Reproducibility in this system is difficult to achieve and analysis of results becomes difficult. A SDW has also been predicted to form on this surface at low temperature [60], but has yet to be confirmed experimentally. RAS spectra from Si(553)-Au have not been recorded, however the Si(775)-Au surface, which has a similar structure to the Si(553)-Au surface [70], is discussed in section 5.5. The main differences between the two reconstructions will be a greater interchain interaction for the Si(553)-Au surface compared to the Si(775)-Au surface [30].

The Si(111)-4×1-In is another example of a metallic chain on Si(111) [99, 100]. It forms when ∼1 ML of In is deposited on a Si(111) surface [101]. It has been extensively studied for many years, as it shows a reversible Peierls-like distortion from a metallic room temperature 4×1 reconstruction to a 4×2 reconstruction at 120 K, and finally to a 8×2 reconstruction at lower temperatures [48]. The distortion is much more Peierls-like than on the Si(111)-Au systems, as defects are only thought to be of secondary importance [102]. The surface has 3 *quasi* 1-D metallic bands, M_1, M_2 and M_3, which are almost parabolic along the wire direction [103, 104]. When the system is cooled the 3 bands show back-folding and gap opening [104]. A gap of 0.34 eV is opened [96]. The structure of the cool 8×2 reconstruction was heavily debated for years but recent RAS studies combined with DFT calculations have helped confirm one of the structures, the hexagon arrangement [105]. For this

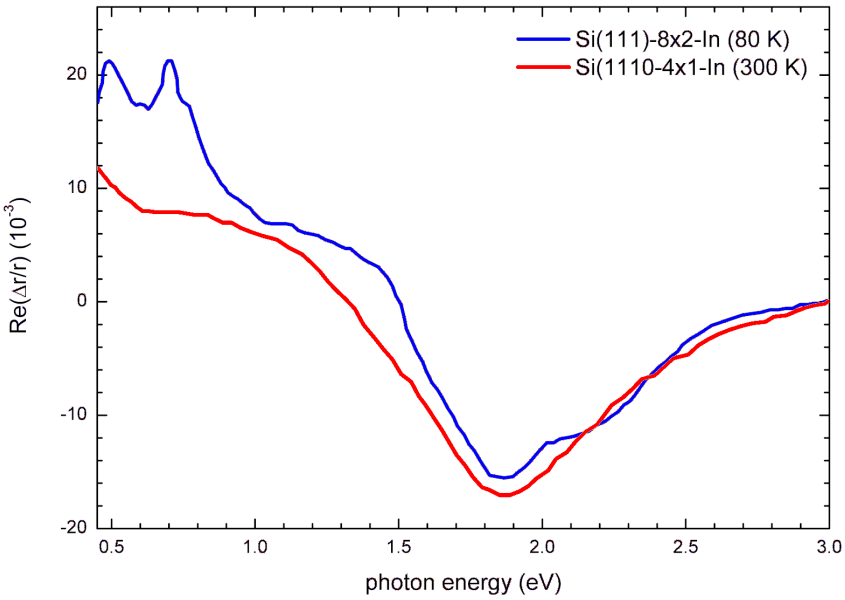

Figure 2.9: RAS spectra from Si(111)-4×1-In at room temperature and at 80K, after [105]

system the RAS response has proved to be critically important in determining the structure of the low temperature phase. The RAS signals for Si(111)-4×1-In and Si(111)-8×2-In are shown in figure 2.9. The structure for the room temperature phase consists of a a broad minimum around 1.9 eV and a large positive signal below 1 eV. The low temperature phase has a similar minimum around 1.9 eV with two positive peaks below 1 eV. It is these peaks that were found to match to predicted optical transitions in the hexagonal model [106, 107] but not the trimer model [99, 108] of the 8×2 phase. Four point probe measurements of this surface show a clear anisotropy in conduction, and a phase transition from a metallic to an insulating state at around 120K [71].

3 Experimental Details

3.1 Sample preparation

All of the samples produced during the course of this work used commercially available vicinal off-cuts of Si(111) as the substrate. Si(111) has two stable off-cut directions, $[11\bar{2}]$ and $[\bar{1}\bar{1}2]$ [23, 28]. Unreconstructed steps in the $[11\bar{2}]$ direction have 1 dangling bond per step atom while steps in the $[\bar{1}\bar{1}2]$ direction have 2 dangling bonds per step atom (figure 3.1). This affects the stability of each of the surfaces. The step density of the surface also affects its stability. Highly unstable surfaces will tend to facet if kinetics allow them to. This means that steps will bunch and the surface will have large step-free terraces [109, 110]. In order to use stepped surfaces as templates for producing single domain surfaces, it is essential to start with regular step arrays which exhibit atomically straight step edges and low kink densities. Samples are cleaned by firstly degassing at 600°C for several hours until the pressure is below 10^{-10} mbar and then flash heating a number of times to 1200°C in ultra high vacuum (UHV) [109, 111]. UHV is defined in this work as a pressure below 10^{-10} mbar.

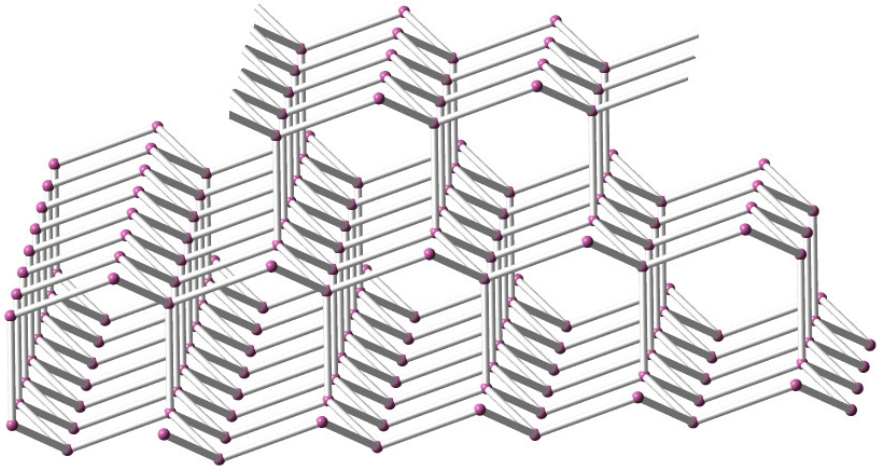

Figure 3.1: This figure shows two steps on unreconstructed Si(111), the right hand step is towards the $[11\bar{2}]$ direction, the left hand step is towards the $[\bar{1}\bar{1}2]$ direction. The steps towards the $[11\bar{2}]$ direction have a single dangling bond per step atom while steps towards the $[\bar{1}\bar{1}2]$ direction have two dangling bonds per step.

Sample heating in UHV can be achieved by a number of different methods. A filament can be used behind the sample to radiatively heat the sample. A similar method is electron bombardment heating using thermionic electrons emitted from

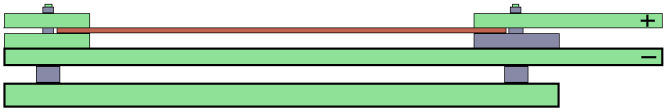

Figure 3.2: The sample mount used for UHV experiments. The green pieces are tantalum, the gray pieces are Al_2O_3 and the orange piece is the Si sample.

a filament and accelerated by an electric field to high energies to heat a sample by transfer of kinetic energy on collision. A third method, used in this work, involves passing a high current through the sample, called resistive heating. In the case of Si the resistive heating method is the most convenient because Si, like all semiconductors, has a negative thermal coefficient of resistance. This means that as Si gets hotter its conductance goes up due to an increase in thermal charge carriers. The first stage of resistive heating is to apply a high voltage across the sample to breakdown the native oxide layer and to create enough thermal carriers for current to begin flowing. When a current is established the sample can be uniformly heated from around 150°C to its melting point. It is important for these experiments that the current always flows parallel to the steps on the Si(111) surface. If the current flows perpendicular to the steps it can cause electromigration of the steps and step bunching will result [112–114]. Each sample can go through several cleaning cycles but eventually the sample degrades due to microscopic roughness called blooming.

Samples are mounted in UHV using a simple clamp (Figure 3.2). Current can then be passed through the sample by applying a voltage between the terminals marked positive and negative.

The sample temperature was measured using optical pyrometry. Pyrometry calculates the temperature of a sample based on the colour of light it emits (the peak of its blackbody radiation spectrum). It was used for centuries by blacksmiths and glass blowers to tell if their furnaces were at the correct temperature. An important property of the material that needs to be known before pyrometry can be used is its emissivity. This is a measure of how similar to a true blackbody the material is. A value of 1 indicates a perfect blackbody. During the course of this work 2 pyrometers were used, one that operated in the range of 600°C to 3000°C and detected wavelengths in the range from 950 nm to 1050 nm, the other that operated in the range from 20°C to 600°C and detected wavelengths in the range of 8000 nm to 14000 nm. Figure 3.3 shows the emissivity of Si in the range of the two pyrometers. For the high temperature pyrometer the emissivity of Si is stable over a broad range of temperatures and has a value of 0.66.

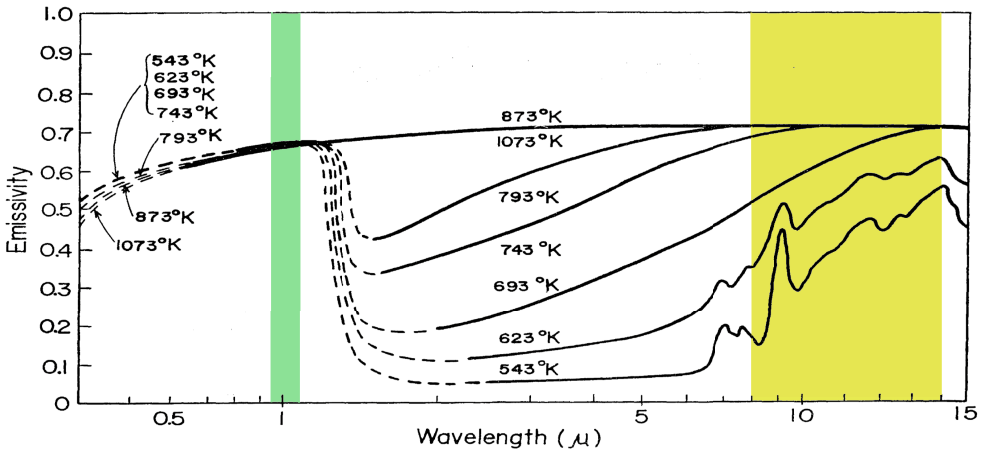

Figure 3.3: The emissivity of Si. The green region are the wavelengths detected by the high temperature pyrometer and the yellow region are the wavelengths detected by the low temperature pyrometer (after [115]).

For the low temperature pyrometer this is not the case. Also, there is another complication with the low temperature pyrometer. A special UHV MgF_2 window must be used for this pyrometer, as fused silica will absorb in its wavelength range. To get around these problems a calibration curve was established using a platinum resistor attached to the back of a Si sample. This platinum resistor could read in the range from -50°C to 800°C but was destroyed by heating above 800°C and so could not be attached to the sample during sample cleaning. The emissivity on the pyrometer was fixed at 0.1 and the recorded temperature could be converted into a real sample temperature. The errors associated with pyrometry are relatively large and with the calibration curve they become larger again. The error on the high temperature pyrometer was established to be ±20°C while on the low temperature pyrometer the error was ±50°C.

Si(111) surfaces off-cut in the $[11\bar{2}]$ direction by small angles will have single height steps if the heat treatment discussed at the start of this section is followed (figure 1.4). Si(775) is Si(111) off-cut by 8.5° in the $[11\bar{2}]$ direction from (111), it will consist of single height steps separated by 2.13 nm. Si(111) surfaces off-cut in the $[\bar{1}\bar{1}2]$ direction by small angles will again have single height steps, however for higher off-cuts step bunching can occur as the surface tries to minimise its surface free energy by forming surface reconstructions. For example on Si(557) (off-cut by 9.5° in the $[\bar{1}\bar{1}2]$ direction) triple height steps are formed with a doubled 7×7 reconstruction on the terraces [116, 117]. Initially surface cleanliness and reconstruction

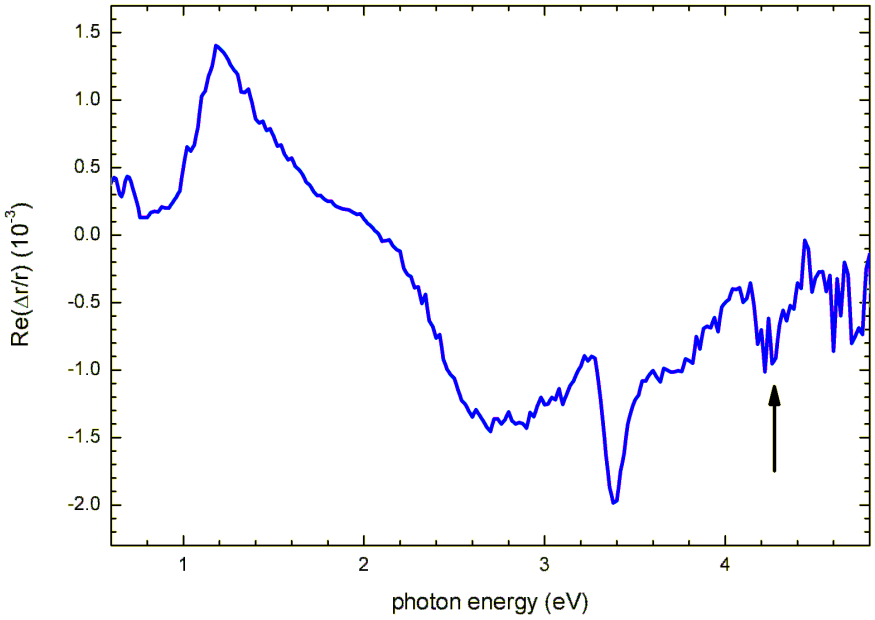

Figure 3.4: RAS spectra of clean Si(557): The structure marked at 4.25 eV is only seen when the surface is clean and well ordered.

were confirmed using low energy electron diffraction (LEED) and Auger electron spectroscopy (AES) (section 3.3). However, it was found that RAS could act as a good fingerprint method to confirm that the surface was clean and well ordered (figure 3.4).

3.2 Molecular beam epitaxy

Metals are deposited using a molecular beam epitaxy (MBE) Knudsen cell. A High Temperature Effusion cell (HTEZ-40) from MBE-Komponenten (figure 3.5a) designed for clean UHV operation up to 1600°C was used for the evaporation of Au. Due to the high operation temperature the filament is made of tungsten and direct contact between filament insulation parts is avoided. Additional insulating PBN ceramic plates are shielded by tantalum plates to prevent outgassing during operation. The HTEZ provided very clean evaporation (background pressure of 5×10^{-10} mbar) and precise temperature control. The crucible material used for the evaporation was Al_2O_3. A WCK-2 Knudsen cell from WA technology was used for evaporating Pb on to the substrates. A crucible made of fine graphite coated with pyrolytic boron nitride (PBN), which showed minimal interaction with the Pb, was used. The crucible is heated using a tantalum foil element, which is insulated with a PBN thermal shield. This Knudsen cell can operate up to temperatures of $\sim$ 1000°C with a low

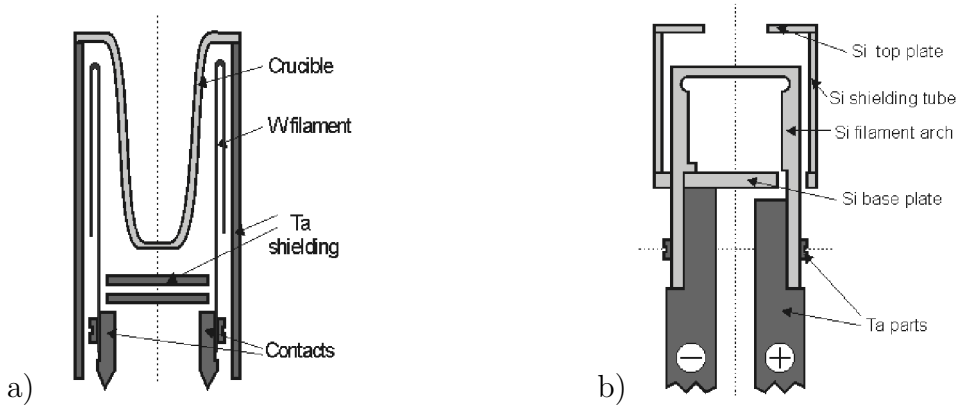

Figure 3.5: a) Schematic of the HTEZ-40 from MBE-Komponenten. b) Schematic of the SUSI from MBE-Komponenten

background pressure of $\sim 5 \times 10^{-10}$ mbar. A Si Sublimation Source (SUSI) from MBE-Komponenten (figure 3.5b) was used for the evaporation of Si for capping studies on Si(111)-Au and Si(557)-Au-Pb systems. The SUSI allowed growth of high quality ultra-thin Si layers. It provided a very clean (background pressure of 1×10^{-9}, this background pressure was confirmed to be H_2 using a quadrapole mass spectrometer) and constant Si flux. The SUSI is commonly used for Si-doping of GaAs epilayers in MBE growth facilities. The specially designed free standing silicon filament arch is directly heated by electrical current up to 50 A and is surrounded by high purity silicon shielding parts. Heating of metal and ceramic parts is minimised by very effective water cooling of the electrical contacts. No insulating ceramic parts are used in the hot zone.

These cells heat the materials to a temperature where they have significant vapour pressure. When this occurs there will be a flux of metal atoms out of the MBE cell. Adsorption occurs when the sample is placed in the beam of atoms. Deposition rates are typically very slow, $\sim$1 ML in 10 min, or 2 nm/hr, allowing for accurate coverages in the submonolayer regime. Deposition rates are measured using a quartz crystal oscillator and, for low coverages, are cross-calibrated using AES, LEED and RAS. The resonant oscillation frequency of the quartz crystal decreases as the mass of the crystal increases due to deposition. For example a ML of Pb would reduce the crystal frequency by about 22 Hz when the resonant frequency is 6 MHz. Different materials require a different temperature for deposition. The temperatures and rates are shown in table 3.1 for the materials used:

Table 3.1: Evaporation temperatures and evaporation rates.

Metal	Temperature	Approximate deposition rate
Au	1200°C	0.0002 ML s^{-1}
Pb	650°C	0.01 ML s^{-1}
Si	$>$ 1200°C	0.011 ML s^{-1}

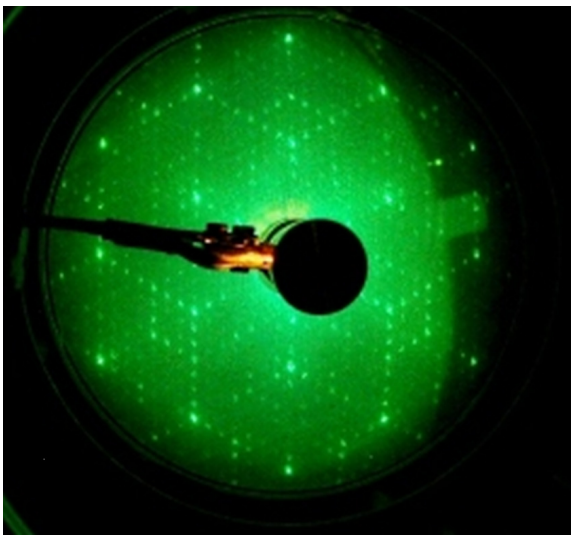

Figure 3.6: LEED image, viewed from the rear, taken from the clean Si(111)-7×7 surface.

3.3 Low energy electron diffraction and Auger electron spectroscopy

Low energy electron diffraction (LEED) is an electron based technique for determining the surface structure of crystalline materials [118]. It has surface sensitivity due to the low penetration depth of electrons in the region from 10 eV to 200 eV (figure 1.2). LEED can provide detailed measurements of surface atomic position by monitoring the spot intensity as the beam energy is scanned [119]. However, LEED was used in this project purely to confirm well ordered surfaces. A LEED image is an image of the reciprocal lattice of the surface. Figure 3.6 is an example of a LEED image from a clean Si(111)-7×7 reconstructed surface. On ordered stepped surfaces spot splitting is sometimes seen, but on the low angle off-cuts that are used in this work spot splitting was not seen due to the large terrace width and low coherence length of the electron beam

LEED images are formed using an electron gun emitting electrons that are back-scattered from the surface onto a fluorescent screen. Low energy electrons ($<$200eV) are used because they will have a de Broglie wavelength similar to that of the surface

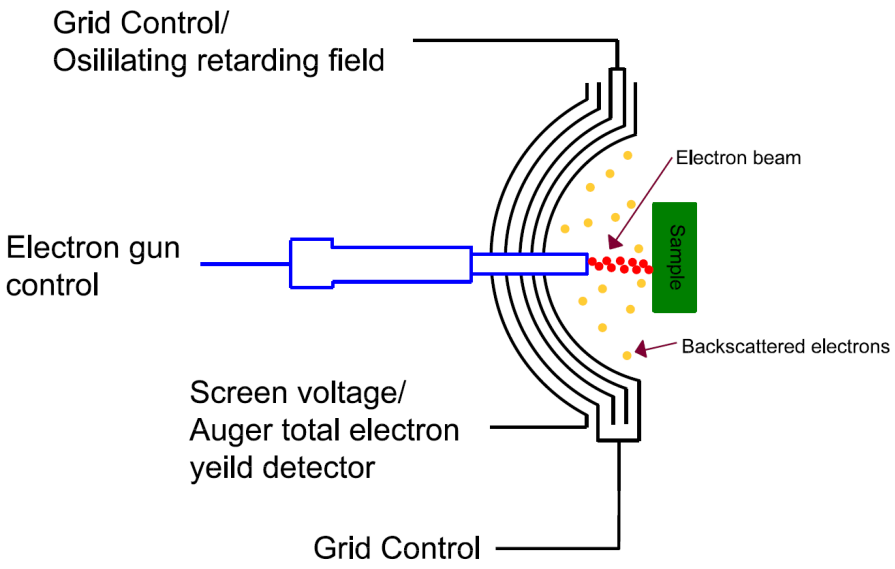

Figure 3.7: Schematic of the LEED-Auger system. To change from LEED to AES the inner grids are switched to an oscillating retarding field and the drain current from the screen is measured with a lock-in amplifier.

atom spacing and they have a very small inelastic scattering mean free path, giving surface sensitivity. A schemitic of the LEED/AES system is shown in figure 3.7.

Auger electron spectroscopy (AES) is a complimentary technique to LEED which can be used to study surface composition and monitor the cleanliness of a surface. Auger electrons are emitted from an atom as it relaxes after a core electron has been ejected. They have a unique energy spectrum for each atom and are used to determine the chemical composition of the surface.

Both LEED and AES were carried out using the same apparatus, an Omicron SpectaLEED rear view LEED/AES system (figure 3.7). It consists of a front mounted electron gun, four high transparency grids, and a phosphor screen. For AES experiments the grids are switched to an oscillating retarding field the drain current on the screen was measured, this type of apparatus is called a retarding field analyser (RFA).

3.4 Scanning electron microscopy

Scanning electron microscopy (SEM) is an electron based imaging tool. It scans a surface with a high energy electron beam using a raster scan pattern. The electrons are generated using an electron gun and accelerated to high energy. They then pass

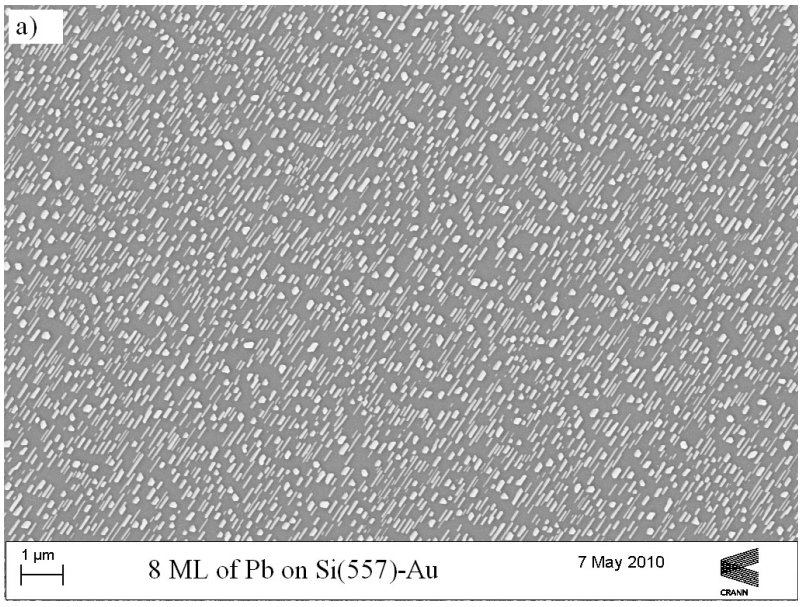

Figure 3.8: SEM image of Pb nanoislands on a Si(557)-Au surface.

through focusing optics to create a very small spot. The electrons are scattered off the surface of the material being imaged and into a electron detector. A resolution of $\sim$1 nm can be achieved using a 30 keV beam. This resolution is limited by the electron beam radius. To prevent charging effects samples must be in good electrical contact with earth. This is archived using conducting carbon tape to hold the sample to the manipulator. Images are analysed using special software to extract average length and width of islands. An example of a SEM image of Pb nanoislands is shown in figure 3.8.

As well as detecting backscattered electrons, most scanning electron microscopes have a x-ray detector. When the high energy electron beam interacts with the surface it can cause core electrons to be ejected. X-rays are generated as the atoms relax back to their ground state. These x-rays have a characteristic wavelength depending on the atomic composition of the surface. Using the x-ray detector it is possible to make atomic maps of the surface.

4 Reflection Anisotropy Spectroscopy

Reflection Anisotropy Spectroscopy (RAS) is a versatile optical technique. It measures the difference in reflectance between light polarised in orthogonal directions in the surface plane (Δr) at near normal incidence, normalised by the mean reflectance r. The RAS signal can be simply described by:

$$\frac{\Delta r}{r} = \frac{2(r_x - r_y)}{r_x + r_y} \tag{4.1}$$

where r_x and r_y are the complex Fresnel reflectance coefficients for light polarised in the x and y direction respectively. RAS can achieve surface and interface sensitivity in systems where the bulk is isotropic and the surface or interface is optically anisotropic.

RAS was first described by Aspnes *et al* and Berkovits *et al* in 1985 [16, 120]. This early work was mainly interested in the study of III-V semiconductors [120, 121] and the recently discovered high temperature superconductors [122]. It was understood early on that RAS had the potential to be a quick and cheap method of studying growth of III-V semiconductors [18, 123–128] because it could operate in environments where electron based techniques could not [129]. However, in recent times RAS has found applications in a broad range of material systems. These include clean single crystal metals [130–135] and semiconductors [16, 136], self-organisation of organics on surfaces [137, 138], surface reconstructions [139–141], aligned nanostructures on surfaces [4, 6, 7, 38, 142, 143] and systems which have been strained along one axis [144–147] (figure 4.1).

At present there are no standard methods for interpreting RAS spectra. With the advent of more powerful supercomputers, RAS spectra can be calculated from first principles. When RAS spectra are analysed from first principles they can provide quite strict limits on the surface structure. Small differences in surface structure can lead to significant changes in the band structure near the Fermi level. As any direct optical measurement probes both the ground and excited state additional computational power is required to calculate optical spectra compared to techniques which only prob the ground state. It is well known, for example, that the widely used density functional theory (DFT) approach significantly underestimates the band gap of semiconductors. However, if these problems can be overcome, RAS can be used to confirm one structural model ahead of others, as has been shown recently for the Si(111)-4 $\times$ 1-In surface [25].

There are several methods of recording RAS spectra. They differ in the mechanism by which they switch the polarisation of the light. There are two main meth-

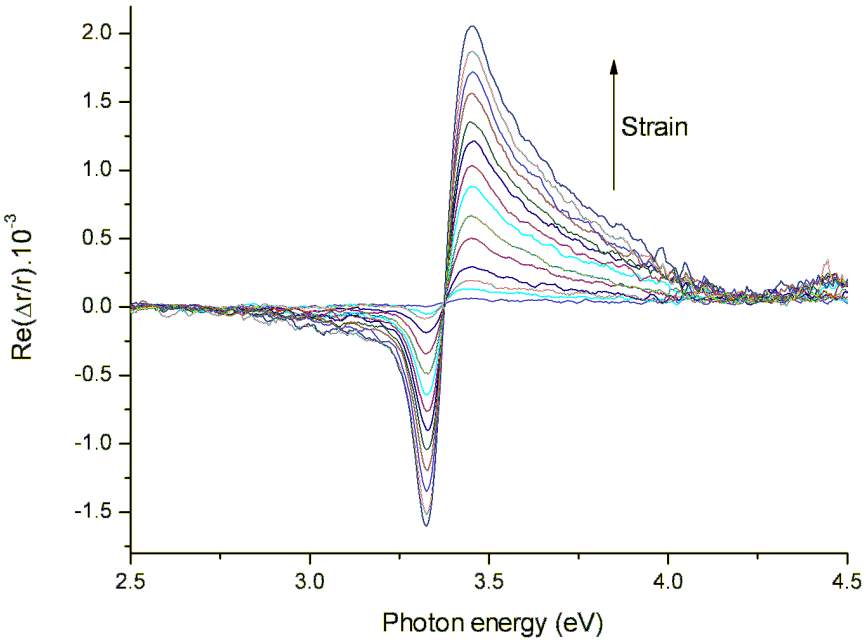

Figure 4.1: The dependence of the RAS signal as Si(100), an isotropic surface, is strained along the [001] direction is shown here. The maximum strain reached before the sample broke was 3.9×10^{-4}.

ods, mechanical rotation of the sample or polarisation and photoelastic modulator (PEM) switching of the polarisation. The most common is now the PEM method, as it offers the opportunity of excellent signal to noise due to the high modulation frequency. During the course of this project a rotating sample setup and 2 PEM instruments were developed.

4.1 Rotating sample/polariser RAS

The simplest way to measure a RAS spectra is to rotate the polarisation of the light with respect to the sample. In this sense both sample rotation and input polarisation rotation are equivalent. For this discussion the Jones matrix formalism will be used (see appendix A). Under the Jones formalism the reflectance of the sample can be described by:

$$\begin{pmatrix} r_x & 0 \\ 0 & r_y \end{pmatrix} \tag{4.2}$$

If we assume a rotating input polarisation given by:

$$\begin{pmatrix} E_0 e^{i\phi} \cos \omega t \\ E_0 e^{i\phi} \sin \omega t \end{pmatrix} \tag{4.3}$$

where ω is the rotational frequency of the input light, the output after reflection from the sample is given by:

$$\begin{pmatrix} r_x E_0 e^{i\phi} \cos\omega t \\ r_y E_0 e^{i\phi} \sin\omega t \end{pmatrix} \tag{4.4}$$

The magnitude of this vector squared then gives the signal recorded at the detector ($V \propto I \propto E^2$, where V is the voltage on the detector, I is the intensity and E is the electric field)

$$V \propto \mid r_x \mid^2 \cos^2\omega t + \mid r_y \mid^2 \sin^2\omega t \tag{4.5}$$

This can be rewritten as:

$$V \propto \frac{\mid r_x \mid^2 + \mid r_y \mid^2}{2} + \frac{\mid r_x \mid^2 - \mid r_y \mid^2}{2} \cos 2\omega t \tag{4.6}$$

In this equation $(\mid r_x \mid^2 + \mid r_y \mid^2)/2$ can be replaced by R and $\mid r_x \mid^2 - \mid r_y \mid^2$ by ΔR giving:

$$V \propto R + \frac{\Delta R}{2} \cos 2\omega t \tag{4.7}$$

This means that there are two components of the signal, a DC component and a component at a frequency of 2ω. By measuring both of these components the RAS signal can be extracted

$$\frac{V_{2\omega}}{V_0} = \frac{\Delta R}{2\sqrt{2}R} \tag{4.8}$$

To show that a rotating sample gives a similar response, the condition that a component with Jones matrix M rotated by θ about the x axis can be represented by a new Jones matrix $M(\theta)$.

$$M(\theta) = R(-\theta)MR(\theta) \tag{4.9}$$

$R(\theta)$ is given by:

$$R(\theta) = \begin{pmatrix} \cos\theta & \sin\theta \\ -\sin\theta & \cos\theta \end{pmatrix} \tag{4.10}$$

A sample rotating at a frequency of ω has a Jones matrix:

$$\begin{pmatrix} r_x \cos^2\omega t + r_y \sin^2\omega t & (r_x - r_y)\cos\omega t \sin\omega t \\ (r_x - r_y)\cos\omega t \sin\omega t & r_x \cos^2\omega t + r_y \sin^2\omega t \end{pmatrix} \tag{4.11}$$

With linear input polarisation this gives an output Jones vector:

$$\begin{pmatrix} r_x \cos^2\omega t + r_y \sin^2\omega t \\ (r_x - r_y)\cos\omega t \sin\omega t \end{pmatrix} \tag{4.12}$$

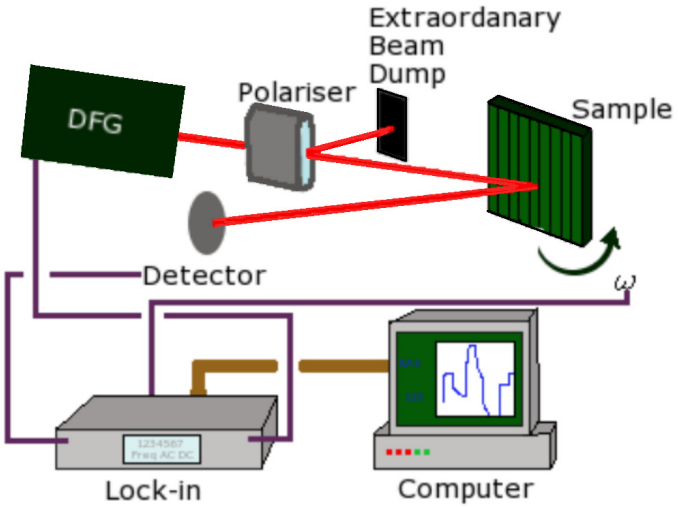

Figure 4.2: A rotating RAS set-up. The sample is rotated at a frequency of ω.

which neatly simplifies to equation 4.5 by again using trigonometric identities. Hence the measured signal can again be described by equation 4.8.

There are several problems with a mechanically rotating system. In the rotating polariser setup the difficulty lies in getting perfectly rotating linear light with no intensity fluctuations. To achieve this the original light must be either circularly polarised or completely depolarised. Circularly polarised light is difficult to realise over a broad spectral range, and depolarising light to less than 1 part in 10^{-4} over a broad spectral range is almost impossible. This means that a rotating polariser setup is confined to looking at changes in a RAS spectrum or overall line shape but cannot in practice give an absolute value of RAS signal. Rotating a half-waveplate is another potential method of creating rotating linear polarised light, but again this is difficult over a broad spectral range. With a rotating sample set-up these issues are removed. By using a Glan-Taylor or Rochon polariser linear polarised light can be created over a large spectral range, depending on the prism material. However problems of beam wobble after the rotating sample can cause artificial RAS signals, especially if the beam path is quite long (for example through a monochromator). It can also be quite difficult to rotate a sample in certain environments, such as UHV.

A rotating sample laser RAS setup was designed to allow the spectral range of the RAS work to be extended below 0.5 eV. This simple set-up consisted of a single MgF_2 Rochon polariser, sample rotation stage and HgCdZnTe thermoelectric (TE) cooled detector (Vigo Systems,PVI-2TE Series) (Figure 4.2). The laser used was a difference frequency generator (DFG) (Coherent, DFG) which is tunable in the region from 0.5 eV to 0.12 eV. This was pumped by a regenerative amplifier (RegA)

(Coherent, RegA 9000) and the seed beam was from a optical parametric amplifier (OPA) (Coherent, OPA 9800) which is tunable in the region from 1.3 eV to 0.54 eV. The laser has a bandwidth of $\sim$ 12 nm which means that a monochromator was not needed. The lasers have a pulse width of $\sim$ 200 fs and the pulse frequency is 100 kHz. The I_0 signal is replaced by I_{100kHz} which can be detected with a good signal-to-noise using a lock-in amplifier. Spectra were recorded by first tuning the laser to the desired energy, then recording $I_{2\omega}$ and I_{100kHz} up to 100 times in about 3 minutes. An average of these points was taken and the RAS signal was calculated.

The program for reading from the lock-in was written in LabView. It consisted of the following logic:

1. Set time constant.
2. Set the Lock-in to read 100kHz
3. Set to 1^{st} harmonic.
4. Wait 5 times the time constant.
5. Read the signal at 100 kHz.
6. Set the Lock-in to read at ω
7. Set to 2^{nd} harmonic
8. Wait 5 times the time constant.
9. Read the signal at 2ω.
10. Repeat from 2. until the required number of points has been recorded.

4.2 Photoelastic modulator RAS

To avoid the problems associated with a mechanical rotation a PEM can be used. A PEM is a device that modulates the phase of the light in one optical axis (hence changing the polarisation state of the light). It is essentially a dynamic waveplate. It works by applying an electric field to a piezoelectric crystal which is coupled to a suitable transparent material, such as quartz or CaF_2. The piezoelectric induces a stress in the material which changes its birefringent properties. Light polarised along the modulation axis will undergo a phase modulation of Γ, while light polarised perpendicular to the modulation axis will be unchanged.

$$\Gamma = \Gamma_0 \sin \omega t \tag{4.13}$$

Half-wave modulation will rotate the plane of polarisation and it can be shown that a value of $\Gamma_0 = 2.405$ rad produces this. The crystal must be driven at its resonance frequency, which will be $\sim 10^5$ Hz for most materials. Another advantage of PEM phase modulation is that both the real and imaginary parts of $\Delta r/r$ can be measured,

not just the real part as in the rotation (intensity modulation) experiments discussed in section 4.1.

In the Jones matrix formulation a PEM can be described by:

$$\begin{pmatrix} \cos\frac{\Gamma}{2} & i\sin\frac{\Gamma}{2} \\ i\sin\frac{\Gamma}{2} & \cos\frac{\Gamma}{2} \end{pmatrix} \tag{4.14}$$

If an experiment is constructed such that the PEM axis and input polarisation are at 45° to the anisotropic axis of the sample, the amplitude of the electric field output (A) is proportional to:

$$A \propto \begin{pmatrix} \cos\frac{\Gamma}{2} & i\sin\frac{\Gamma}{2} \\ i\sin\frac{\Gamma}{2} & \cos\frac{\Gamma}{2} \end{pmatrix} \begin{pmatrix} r_x & 0 \\ 0 & r_y \end{pmatrix} \begin{pmatrix} 1 \\ 1 \end{pmatrix} \propto \begin{pmatrix} r_x\cos\frac{\Gamma}{2} + ir_y\sin\frac{\Gamma}{2} \\ r_y\cos\frac{\Gamma}{2} + ir_x\sin\frac{\Gamma}{2} \end{pmatrix} \tag{4.15}$$

This would produce a phase modulation at the detector. In order to turn the phase modulation into an intensity modulation an analyser polariser is used, at 45° to the PEM axis (parallel to the sample axis). This means the amplitude at the detector is:

$$A \propto \begin{pmatrix} 1 & 0 \\ 0 & 0 \end{pmatrix} \begin{pmatrix} r_x\cos\frac{\Gamma}{2} + ir_y\sin\frac{\Gamma}{2} \\ r_y\cos\frac{\Gamma}{2} + ir_x\sin\frac{\Gamma}{2} \end{pmatrix} \propto \begin{pmatrix} r_x\cos\frac{\Gamma}{2} + ir_y\sin\frac{\Gamma}{2} \\ 0 \end{pmatrix} \tag{4.16}$$

The voltage on the detector is proportional to $|A|^2$, and is a harmonic series of V_0, V_ω, $V_{2\omega}$ etc. By performing a Fourier transform we find that each term depends on a Bessel function J_n, where n is the order of the Bessel function. Odd harmonics are found to depend solely on the imaginary part of $\Delta r/r$ while even harmonics depend solely on the real part of $\Delta r/r$:

$$\frac{V_\omega}{V_0} \propto \quad J_1(\Gamma_0) Im(\tfrac{\Delta r}{r}) \sin(\omega t) \tag{4.17}$$

$$\frac{V_{2\omega}}{V_0} \propto \quad J_2(\Gamma_0) Re(\tfrac{\Delta r}{r}) \cos(2\omega t) \tag{4.18}$$

$$\frac{V_{3\omega}}{V_0} \propto \quad J_3(\Gamma_0) Im(\tfrac{\Delta r}{r}) \sin(3\omega t) \tag{4.19}$$

The PEM RAS system, as well as giving excellent signal-to-noise and access to both real and imaginary parts of the RAS signal, allows us to perform some very simple calibration measurements. If the input polariser is misaligned with respect to the PEM axis there will be a constant offset in the signal. This can be used to check for nonlinearities in the PEM or other components.

For general RAS studies two PEM RAS systems were developed: A broad band RAS system (figure 4.4) and a compact system which can easily be transported.

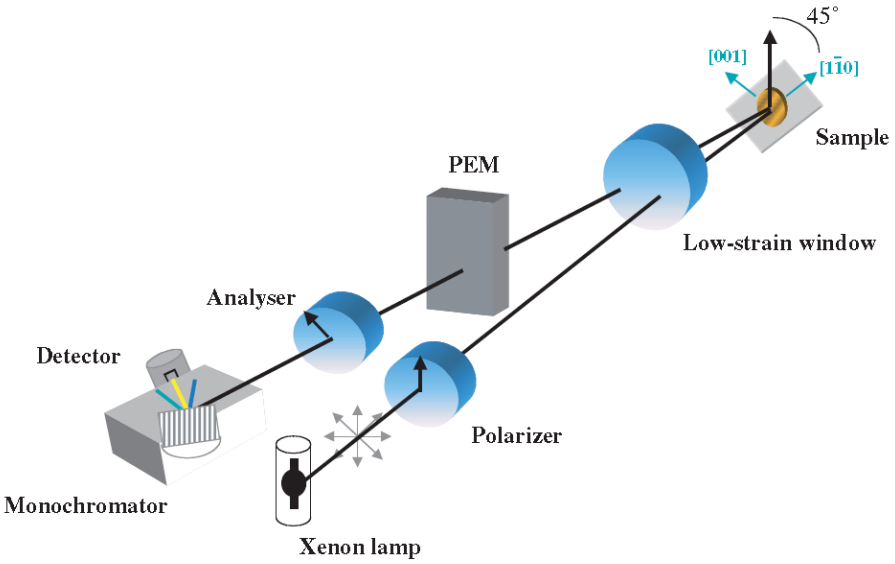

Figure 4.3: A schematic of a PEM RAS system, after [17].

Both systems are of a similar design (figure 4.3). The broad band system consists of a high pressure Xe lamp, MgF_2 coated Al mirrors, a filter wheel, MgF_2 Rochon polarisers, CaF_2 PEM (Hinds instruments, II/CF57), a three grating monochromator (Bentham Instruments, TMc300-USB), a Si-InGaAs detector (Elektronik-Manufaktur Mahisdorf) and a liquid N_2 (l-N_2) cooled InAs detector (Hamamatsu). Detectors were changed using a micro stepper motor. The DC signal was read using a sensitive analogue to digital converter and the AC signal was read with a lock-in with a reference frequency of twice the PEM frequency. The components that differed in the compact system are the polarisers (quartz Glan-Taylor), the PEM (fused silica) (Hinds instruments, I/FS50), there is no InAs detector and the monochromator had two gratings. A flexible LabView program was written to allow interchangeability between several different components and could be used with both systems. The program also allowed several types of measurement. These include spectral RAS, time dependent RAS (to monitor growth), magnetic field dependent RAS (essentially measuring the magneto optical Kerr effect, MOKE), PEM voltage dependent RAS (to calibrate the PEM) and alignment mode where the DC and AC signals are plotted for alignment of samples and other components. A description of the LabView code is included in Appendix B

High pressure Xe bulbs have been on the market for 50 years. They work by using a high voltage to ignite a plasma and then only require a modest power (75W) to maintain the light output. They produce light over a very broad range from 0.25 eV to 5.5 eV. In a Xe lamp the majority of the light is produced in a tiny ($\leq$

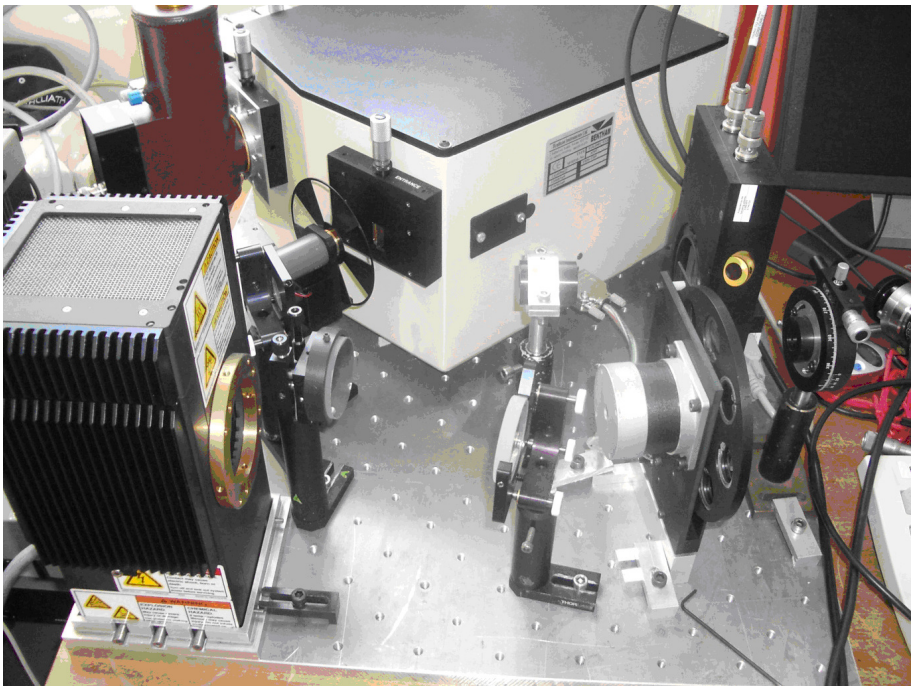

Figure 4.4: The broad-band RAS system

1 mm^2) area around the electrodes, which means the focal size can also be small. Even though the Xe is at high pressure the lamp still produces strong emission lines, especially around 1.2 eV (figure 4.5). Intensity is limited in the IR and UV mainly because of light being absorbed in the bulb material.

Focusing and beam alignment in the RAS systems was performed using MgF_2 coated Al mirrors. These mirrors have a good reflectance over a large spectral range and are resistant to corrosion. They offer $\geq 90\%$ reflectance from 3 eV to 0.12 eV, and a $\geq 85\%$ reflectance from 5 eV to 3 eV. The main focusing mirror had a focal lenth of 1 m for both systems, which alowed the beam to be directed through a low strain quartz window into the vacuum chamber. A secondary focusing mirror was used to focus into the monocromator.

MgF_2 Rochon polarisers were used in the broad band system. They separate the light into two beams with an angular separation of about 3°, varying slightly with wavelength. They have an extinction ratio of at least 10^{-5} and work in the region from 9 eV to 0.2 eV. On the compact system quartz Glen-Taylor polarisers were used. They are crystals cut close to Brewster's angle so that the refracted and reflected beams are polarised. The refracted beam has an extinction ratio better than 10^{-5}. They work in the region from 5.5 eV to 0.6 eV.

The PEM on the broad band system is an IR optimised CaF_2 PEM. It is designed to work in the region from 0.65 eV to 0.22 eV but by writing a calibration file for

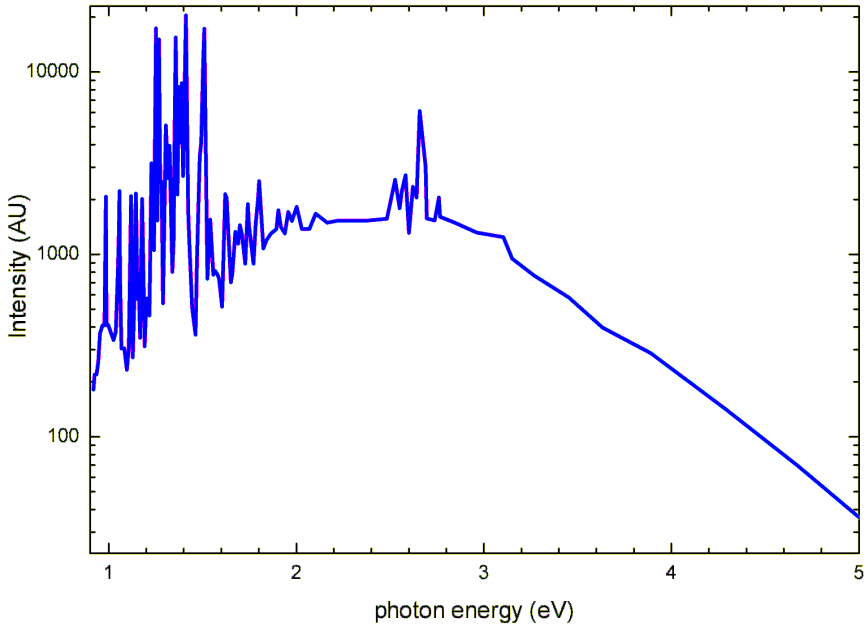

Figure 4.5: The emission from a high pressure Xenon bulb

the PEM using LabView it is possible to use it from 5 eV. This PEM modulates the light at 57 kHz. The PEM for the compact system is made from fused silica and is optimised in the region from 5 eV to 1.5 eV. Again by using a calibration and LabView this range can be extended to 1 eV easily and 0.75 eV if a damping factor is included. The PEM on the compact system operates at 50 kHz.

The monochromator and filter wheel select the energy of the light. The monochromator for the broad band system has 3 gratings, one for $\geq$2.1 eV, one for 2.1 eV to 0.8 eV, and the 3rd for $\leq$0.8 eV. Under normal conditions the slit width on the monochromator is 1 mm, giving resolutions of 1.35 nm, 5.4 nm and 10.8 nm respectively, for the different energy ranges. The filter wheel is used to prevent 2nd order effects in the monochromator. There are 4 filters for different energy ranges. A neutral density filter was also incorporated to help prevent detectors overloading in the region of the strong lamp lines. For the compact system a much smaller monochromator is used. It consists of two gratings, one for above 3 eV and one for 3 eV to 0.75 eV. Due to the small size of the monochromator the resolution is much poorer than the broad band system, a resolution of $\sim$ 10 nm is recorded on the first grating and $\sim$ 25 nm is recorded on the second grating.

Three detectors were used to cover the spectral range. For the region above 1.4 eV a Si detector was used, which had a $\times$30 DC amplifier for the region above 4 eV. An InGaAs detector covered the range 0.75 eV to 1.4 eV, using the same electronics as the Si detector. The electronics for these detectors consisted of a filter

to split the DC and AC signals, which were then connected to the analogue to digital converter and lock-in, respectively. To switch between these two detectors a micro stepper-motor was used. The signal cables into the lock-in were switched using solid state relays. There was a small damping of $\sim 5\%$ of the AC signal coming from the InGaAs detector. The third detector was an InAs liquid N_2 cooled detector. It was designed to work in the region from 0.75 eV to 0.42 eV. It was shipped with a filter on the signal line that damped the AC signal by a factor of ~ 10000, but the lock-in could still read an AC signal, albeit with significantly more noise than the Si and InGaAs detectors. This problem was resolved by recording the AC several times and using a long time constant. Recording a much higher density of points in the region of this detector and post measurement averaging of points also helped. The detectors on the compact system were the same as the Si-InGaAs detectors on the broadband system.

4.3 Origins of a RAS spectrum

The optical transitions probed by RAS are determined by both the bulk and surface dielectric function of the material. To be useful for surface science RAS must be sensitive to the surface structure of the material at the atomic scale. This can be achieved if the bulk crystal is isotropic. For cubic and amorphous materials it is clear that there is no bulk anisotropy so any RAS signal must come from the surface. Unreconstructed (111) and (100) surfaces of cubic materials are isotropic and show no RAS signal, however the (110) surface is anisotropic and will have a RAS signal (figure 4.6). Reconstructed (111) or (100) surfaces from cubic materials can give a RAS signal but normally they will be in a number of equivalent domains, and domain averaging will mean no RAS signal is recorded. This is because RAS will sample over a macroscopic area due to the size of the beam spot and domain averaging will mean no RAS signal is seen.

The Jones matrix method explains how different experimental set-ups can detect small anisotropies in the reflectance from a sample, but the question of where this anisotropy comes from has not been addressed. Phenomenological models have been developed to relate the optical anisotropy to the surface dielectric function.

The 3 phase model assumes a sample consisting of an isotropic bulk (with dielectric function ϵ_b), thin anisotropic surface layer (ϵ_s^x and ϵ_s^y) and then a vacuum layer. It is assumed that there is an abrupt change between each of these layers. It was derived from Fresnel theory of reflection [148] and was originally used to analyse

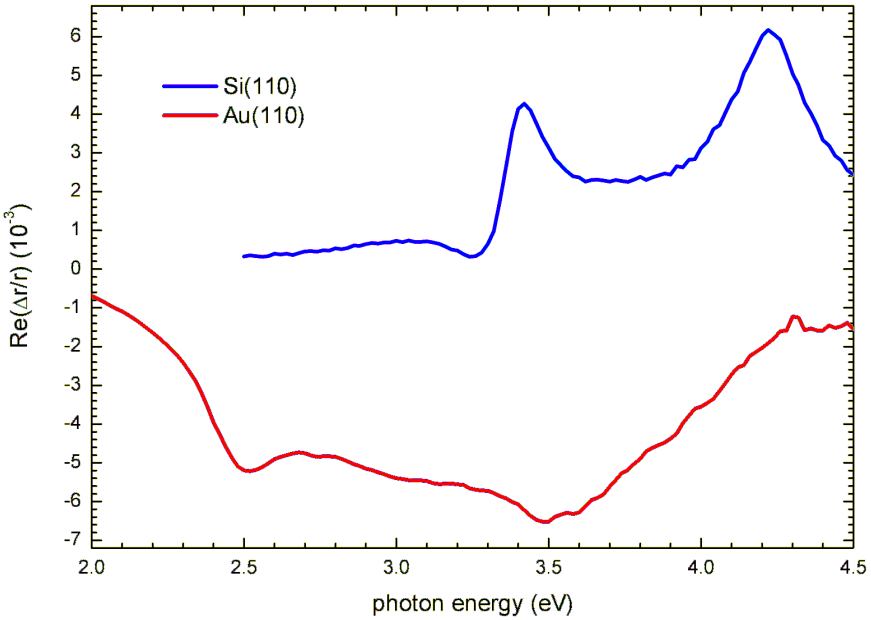

Figure 4.6: RAS signal from two different (110) surfaces of cubic materials, Si and Au.

differential reflectance measurements:

$$\frac{\Delta r}{r} = \frac{4\pi i d}{\lambda} \frac{\epsilon_s^x - \epsilon_s^y}{\epsilon_b - 1} \tag{4.20}$$

where d is the thickness of the anisotropic layer, λ is the wavelength of the light, ϵ_b is the bulk dielectric function of the substrate and ϵ_s^i is the dielectric function of the surface layer in the i direction. While equation 4.20 is useful as it relates $\Delta r/r$ to $\Delta\epsilon$ it still does not explain where the anisotropy originates. A number of different phenomenological models have been used [17]. These include a Lorentzian describing an optical transition that is only active when light is polarised in one direction (equation 4.21), a surface modified bulk state [139, 149, 150] (equation 4.22) and anisotropic conductivity [10] (equation 4.23). During the course of this work a model involving a Bruggeman type dielectric function was also developed for large anisotropic metallic islands (section 7.2.2). The formula used are:

Lorentzian;

$$\epsilon_s^x = 1 + \frac{S/\pi}{\omega_t - \omega + i\Gamma/2} \qquad \epsilon_s^y = 1 \tag{4.21}$$

where S is the amplitude, ω_t is the energy of the transition and Γ is the full width at half maximum height (FWHM);

Surface modified bulk state;

$$\Delta\epsilon_s \approx (\Delta E_g - i\Delta\Gamma)\frac{d\epsilon_b}{dE} \tag{4.22}$$

where ΔE_g and $\Delta\Gamma$ are the relative shifts in energy and line width for x and y polarisation;

Anisotropic conductivity;

$$\frac{\Delta r}{r} = \frac{2d}{\epsilon_0 c}\frac{\Delta\sigma}{\epsilon_b - 1} \tag{4.23}$$

where $\Delta\sigma$ is the difference in optical conductivity between the x and y directions of the surface.

Each of these models give some phenomenological understanding of the physics underlying the RAS spectra, however in many cases none of these methods will suffice and sometimes more than one method is required, depending on the spectral region. A first principles approach is necessary for a fundamental understanding of RAS spectra. Optical measurements have always been a challenge to calculate. Until the late 1990s most RAS calculations used an empirical adjustment so that the experimentally measured band gap matched the calculated gap [151, 152]. However, this approach is clearly limited [153].

An optical transition in the visible or near IR region of the electromagnetic spectrum involves the excitation of an electron from its ground state to an excited state above the Fermi level. In order to calculate an optical spectrum from first principles both states must be accurately described and the matrix element linking them must be calculated. Within the independent particle model the imaginary part of the dielectric function is given by:

$$\mathrm{Im}[\epsilon_M(\omega)] \propto \sum_{v,c} \int_{BZ} \left|\langle \varphi_{v,\underline{k}} \left| q_i \right| \varphi_{c,\underline{k}} \rangle\right|^2 \delta(\in_c - \in_v - \hbar\omega) d\underline{k} \tag{4.24}$$

where $\epsilon_M(\omega)$ is the frequency dependent dielectric function, $\varphi_{v,\underline{k}}$ is a function describing the valance band, q_i describes the matrix element linking the valance and conduction band and $\varphi_{c,\underline{k}}$ is a function describing the conduction band.

Density functional theory (DFT) is currently the main approach for electronic structure calculation and is a very good method for calculating the ground state properties of a system [154]. Calculations can be made in a reasonable time frame by using the local density approximation (LDA). This assumes that the contribution to the exchange correlation, arising from the electron density at a certain distance, is equal to that of a homogeneous electron gas with the same density.

Surface DFT calculations have an additional complication in that the surface breaks the periodicity of the system so that Bloch's theorem cannot be used in the direction perpendicular to the surface. This is generally overcome by using a slab approach. A slab of about 10-20 atoms thickness is used, together with a vacuum layer thick enough to minimise interactions between the slabs when the unit is

repeated in the surface normal direction. Molecular dynamics calculation are often used to adjust the atomic positions in the surface region to obtain a minimum in the potential energy of the system prior to calculating the optical response.

The optical properties of a system are expressed through its dielectric function. To calculate this both the valance band and conduction band should be known (equation 4.24). The error in the conduction band energies associated with DFT are often corrected by using a rigid band offset based on the experimental bulk values. For Si, this correction is $\sim$ 0.6 eV [155]. Quite small adjustments in the atomic positions can have drastic effects on the predicted RAS spectra, showing that RAS can be an extremely useful surface structure probe [25]. In the 1960s a new method of calculating the exchange correlation energy was described, called the GW approximation[156]. It is computationally very expensive, but the development of high performance computing has allowed the GW approach to be used to produce much more satisfactory calculation of optical properties of surfaces. For a bulk system the GW correction has a similar effect to the rigid band offset, but for surfaces it leads to a non-uniform shift in optical transition energies, producing a change in RAS line shape as well as shifting the spectrum.

In some cases even the GW approximation is not sufficient to produce a satisfactory RAS spectrum. In particularly local field and excitonic effects may have significant effects and multi-particle effects then have to be addressed. Of these the excitonic effect appears to be more important [157–160]. It is important to point out that these calculations are very computationally expensive and most calculations involving large structures still use DFT-LDA [161, 162]. The three step approach (DFT followed by GW followed by excitonic effects) represent the current state of the art [160]. By using a combination of RAS and optical response calculations the value of RAS as a surface science technique especially in the IR, has clearly been shown [25] and significant progress has been made to show that RAS can be used to resolve similar issues on other controversial surfaces (Chapter 6).

5 Si(111)-5×2-Au and related surfaces

5.1 Early work

Initial studies involving Au deposited on Si single crystals were trying to find out if Au was a suitable dopant for microelectronic components [163, 164]. These experiments gave some interesting results and similar systems involving Si nanowires are still studied today as potential solar cell materials [165, 166]. During the course of these early studies it was found that Au would form different surface reconstructions depending on the thickness of the Au layer. Figure 5.1 shows a surface phase diagram of these reconstructions. The lowest coverage reconstruction was found, by Bishop and Riviere in 1969, to be a "5×1" reconstruction [167]. For the next decade studies on this "5×1" surface were concerned with discovering its structure [168]. An assumption was made that the Au was simply weakly absorbed on an unperturbed Si(111)-1×1 surface. It was not until an experiment by Perfetti et al in 1980 that it was discovered that the surface layer was in fact Si rich [169], leading to new models where the Si(111)-1×1 surface was perturbed.

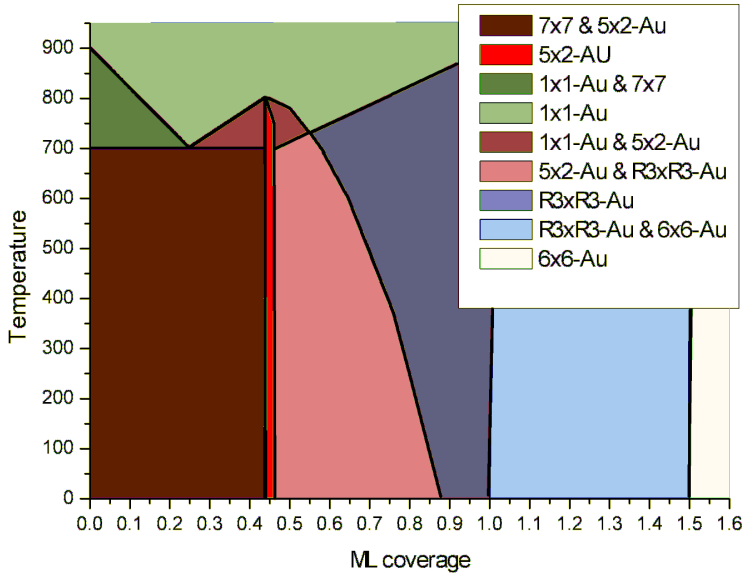

Figure 5.1: Surface phase diagram of the Si(111)/Au system (after [170]).

5.2 Development of a structural model for Si(111)-5×2-Au

The initial idea that the Au sat above an unperturbed Si(111) surface was shown to be incorrect when energy loss spectroscopy studies showed that the Au was em-

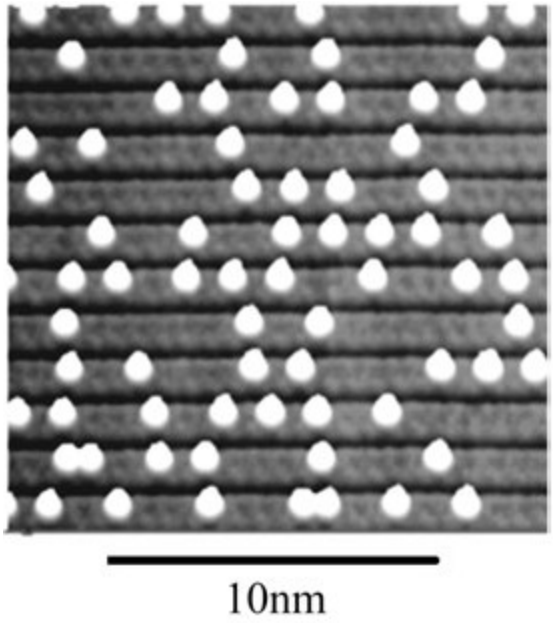

Figure 5.2: Si adatoms on top of Si(111)-5×2-Au. The bright white spots are the Si adatoms (after [36]).

bedded in the surface layer [169]. However, there is still debate about the structure of this widely studied system. Even the Au coverage is controversial [98].

Early structural models relied on X-ray standing wave measurements [171, 172] and low energy ion scattering [173] to determine atomic positions. These early experiments identified that the Au was embedded in the 1st atomic layer of the Si(111). The studies also showed that the Au was in an unusual site. On Si(111) there are three common bonding sites identified, a 6-fold coordinated site in between layers of Si(111) and a 1- and 3-fold coordinated site above the surface plane. The Au sat in none of these sites [172, 174].

When atomic resolution STM images were recorded in the early 1990s they should have helped resolve the surface structure but instead they added more complications. Images of the Si(111)-5×2-Au were covered in bright spots of high electron density, labeled protrusions (figure 5.2) [33, 175, 176]. Initially these protrusions were labeled as Au adatoms [177] because the two chain model of the 5×2 reconstruction required ∼0.4 Ml of Au but it was always found that the optimum reconstruction was formed at slightly higher coverages, often above 0.5 ML [38, 178]. By accounting for one adatom per two 5×2 unit cells this meant that the optimum coverage for Au would be ∼0.45ML, a better agreement with experiment. However, when these adatoms were identified as Si [36], the coverage discrepancy was largely ignored.

Determining that the protrusions were Si was challenging but was eventually

confirmed both experimentally [36] and theoretically [35]. It was discovered that the adatoms are key to the stability of Si(111)-5×2-Au. They sit on a site between two Au chains and form a 5×4 superlatice [24, 35, 37, 54, 179]. The adatoms will act as an electron donor for the chains, causing them to change from metallic to semiconducting. The mechanism of the band gap opening is not due to the individual adatom but more to a collective change in the structure of the chains on the surface [55, 180]. The adatoms drive a *pseudo* Peierls transition causing a doubling of the periodicity along the chain direction and subsequent band gap opening. The coverage of one adatom per two 5×2 unit cells is not normally observed over the whole surface. The as deposited coverage is about one adatom per four unit cells. The surface segregates into two regions, adatom-free 5×2 and adatom-decorated 5×4 (figure 5.2). The reason behind this segregation are unclear but it is thought to relate to the hopping potential of adatoms between neighboring sites and the relatively low binding energy of the Si adatoms [54, 181]. It is possible to saturate all the adatom sites by depositing Si onto the Si(111)-5×2-Au [55]. By annealing the surface to various temperatures the adatoms can then be removed.

The Si honeycomb chain, a graphitic chain of Si atoms (figure 5.3), is a key component of many metal on Si(111) structures. It is seen on all the Si(111)-3×1 reconstructed surfaces, such as Si(111)-3×1-Ag, -Na, -Ca and -K [182, 183]. Si(111)-5×2-Au also contains this structural feature. The honeycomb chain is a very stable structure. It is almost perfectly latticed matched with Si(111) in one direction (along its length) but does not lattice match in the other. The metal atoms act as a re-bonding row between honeycomb chains. In the case of Si(111)-5×2-Au the Au is thought to form a double [37] or, very recently, a triple chain between honeycomb chains [24]. Different theoretical models, as well as disagreeing on the number of Au chains, also disagree on the placement of the Au chains. In total there are 36 possible chain locations for the double chain model [37] and then there are different methods of shifting the phase of the chains to generate the ×2 seen in the structure. No structure matches all the available experimental data, the best candidates would seem to be the structure by Chuang [37] (does not fit STM, but has lowest computed surface energy), Riikonen [179] (fits STM and XPS, but not the lowest energy) and Erwin [24] (figure 5.4) (fits STM and XPS, but unconventional three chain model). Significant progress has been made in using reflection anisotropy spectroscopy combined with theoretical calculations to provide answers as to which of these models is most likely.

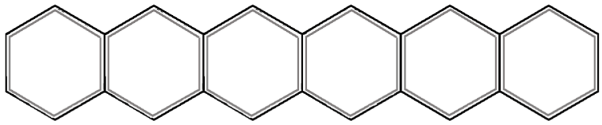

Figure 5.3: Si honeycomb chain.

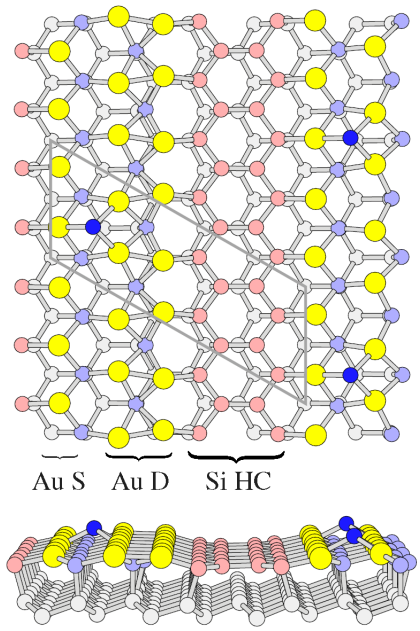

Figure 5.4: The three Au chain model for the Si(111)-5×2-Au (after [24]). Au atoms are yellow, the Si honeycomb chain is pink, and the Si adatoms are dark blue.

5.3 Faceting

Surfaces will normally reconstruct to minimise their surface free energy, and one way for them to do this is to pair up dangling bonds and form surface reconstructions (such as Si(111)-7×7 [184]). Another way is to rearrange surface atoms so that, instead of one high energy surface, two lower energy surfaces are formed. This was first discussed by Herring in 1951 [110]. For singular Si(111) this does not occur, but when steps are introduced it has been found that the steps will bunch at certain temperatures, forming facets. When Au is deposited on the surfaces it can change the faceting behavior drastically [175, 185–189].

Two examples of this Au-induced faceting are described. Si(111) off-cut in the $[11\bar{2}]$ direction, after appropriate heat treatment (section 3.1), will consist of equally spaced single height steps (figure 1.4), but when Au is deposited at 600°C the surface changes into Si(111)-5×2-Au and Si(775)-Au facets [175, 185, 186]. Clean Si(557) will facet into $(\bar{1}\bar{1}2)$ triple height steps and Si(111) terraces with a doubled 7×7 reconstruction. The step and terrace forms a repeating structure that is 5.73 nm wide [116, 117]. When Au is deposited at 600°C the surface reorganises into a perfect Si(557)-5 × 1-Au surface [188].

5.4 RAS results and discussion for Si(111)-5×2-Au

RAS spectra were recorded for Au deposited on Si(111) samples off-cut in both the $[\bar{1}\bar{1}2]$ direction and $[11\bar{2}]$ direction at various vicinal angles. Si was then deposited on top of the 5×2 reconstruction to firstly examine the effects of adatoms on the surface and then, after further deposition, to see if the electronic structure was significantly perturbed by the capping process.

Clean surfaces were obtained by the procedure described in section 3.1, and LEED images and Auger spectra were recorded. Substrates were, n-type, doped with P, and had a typical resistivity in the range 1-10 Ω cm. The Auger spectra (figure 5.5 A) clearly show the large Si peak at 92 eV. By examining the spectra carefully in the region between 150 eV and 520 eV a residual carbon peak can be seen at 271 eV and no oxide peak can be seen (an oxide peak would be expected around 500 eV). Allowing for the AES cross-section and the response of the RFA, $\sim$ 0.02 ML of C is present on the surface. The LEED image shown in figure 5.5 B shows the 7×7 reconstruction associated with clean Si(111).

RAS spectra were also recorded to give a fingerprint of a clean Si surface (figure 5.6). It was found that there were two peaks at bulk critical points for Si, at 3.4 eV

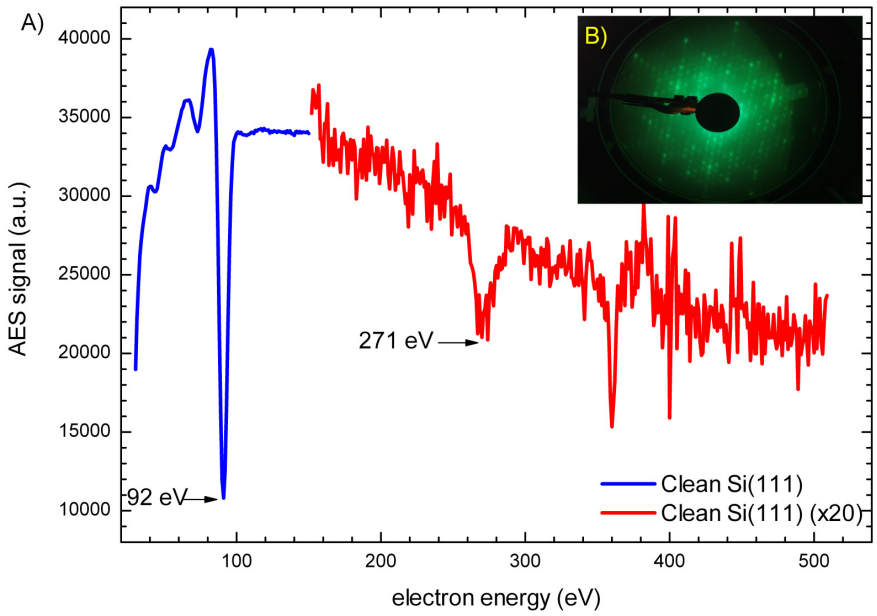

Figure 5.5: A) AES of clean Si. B) LEED of clean Si(111), showing the 7×7 reconstruction.

and 4.25 eV. These peaks are a step modified bulk signal which has an anisotropy due to the aligned steps [190]. It was found in general that the peak at 4.25 eV, was only seen on a clean well-ordered surface. Due to the relative simplicity of recording a RAS spectra compared to Auger and LEED, normal procedure was to clean the Si until the peak at 4.25 eV was optimised. Figure 5.6 shows a typical limit of RAS sensitivity of $\sim 2 \times 10^{-5}$, although the zero line error may be an order of magnitude larger.

5.4.1 Si(111)-5×2-Au RAS signal

The RAS signal recorded from a Si(111)-5×2-Au off-cut by 2° in the $[\bar{1}\bar{1}2]$ direction is shown in figure 5.7. The RAS signal has several key features. The features around 3.4 and 4.25 eV, have been discussed for the clean surface. Features lower in energy are related to the surface phase. The broad minimum between 1.8 and 2.8 eV shows that, in this spectral region, the dominant surface polarizability is in the direction perpendicular to the chains. The dominant surface polarizability lies along the chains between 0.7 and 1.0 eV, as shown by the large maximum in this region. The sharpness of the onset, combined with the downturn below 0.7 eV, suggests that the structure originates from dominant interband transitions aligned along the chains, rather than the intraband transitions that can produce a Drude IR

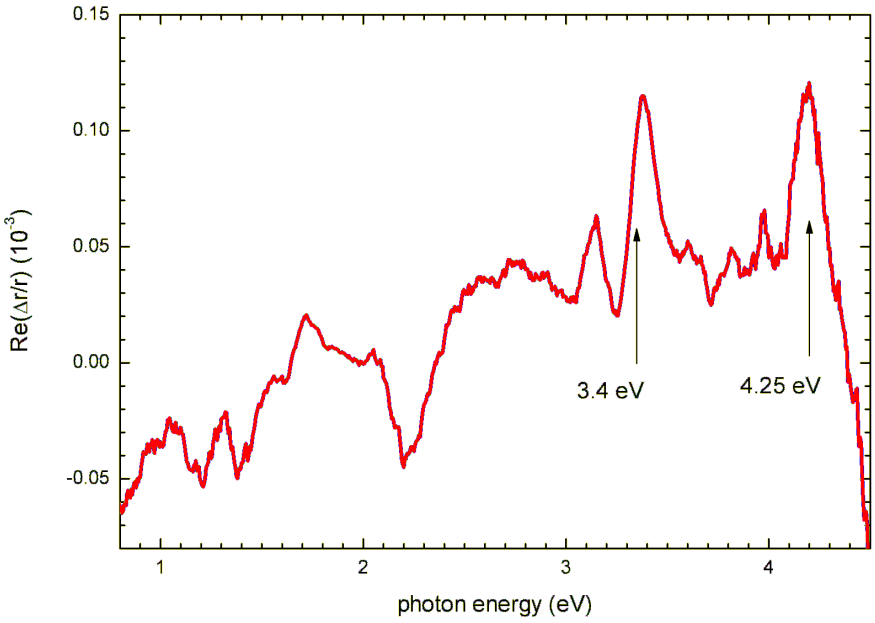

Figure 5.6: RAS of clean Si(111) off-cut by 2° in the $[\bar{1}\bar{1}2]$ direction. This RAS spectra also shows the limit of the sensitivity of the RAS setup: the structure at 2.2 eV is related to a large change in the DC signal when the grating is changed and the structures at 1.2 eV and 1.4 eV are related to emission lines from the xenon lamp.

tail in metallic nanostructures [10]. LEED and Auger were used to confirm that a Si(111)-5×2-Au surface had been formed (figure 5.8). As well as the Si and C peaks seen on clean Si(111), peaks are seen at 45 eV, 56 eV and 72 eV, which correspond to Au.

5.4.2 Si(111)-5×2-Au coverage

During Au deposition the RAS signal was monitored at a particular energy. When the RAS signal reached a minimum/maximum it gave an indication that the surface reconstruction was optimised. For the Au on Si(111) surfaces the RAS was monitored at 2.5 eV, deposition was started at a known time and stopped when the signal reached a minimum. During deposition the sample was held at 600°C and, after deposition was stopped, the sample was annealed at 600°C, over a period of typically 30 minutes, until no further changes were seen in the RAS at 2.5 eV (figure 5.9). This method allowed the accurate calibration of the deposition rate of the Au. For the Si(557)-Au reconstruction the coverage of the Au is known to be 0.176 ML [98]. By using this value an optimum coverage is found for Si(111)-5×2-Au off-cut by 4° in the $[11\bar{2}]$ direction, Si(111)-5×2-Au off-cut by 3° in the

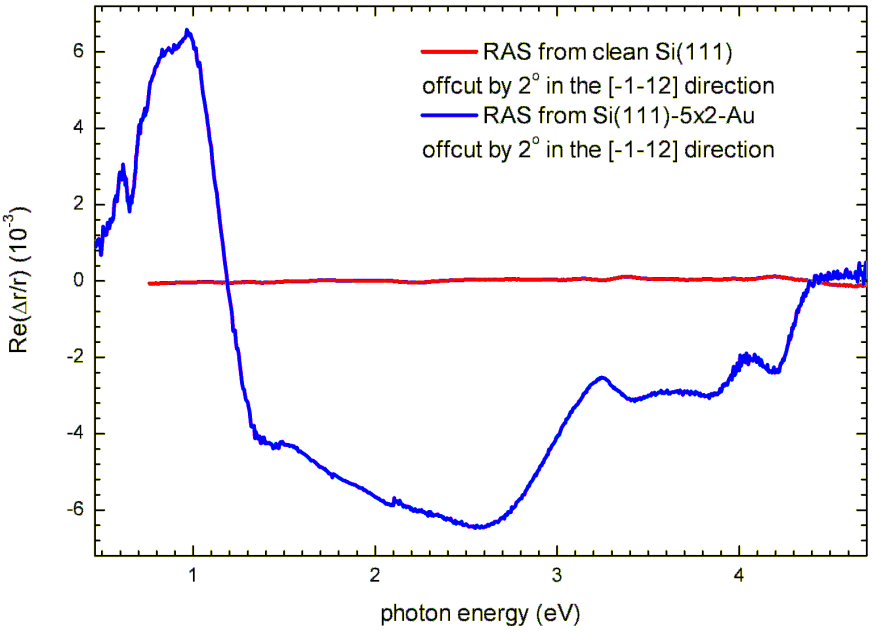

Figure 5.7: RAS of Si(111)-5×2-Au off-cut by 2° in the $[\bar{1}\bar{1}2]$ direction.

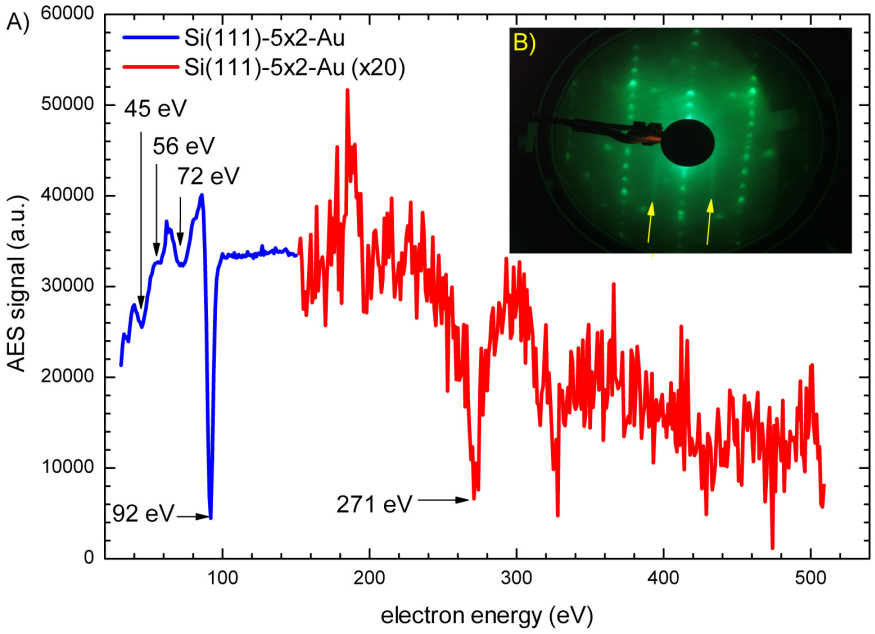

Figure 5.8: A) Auger of Si(111)-5×2-Au. B) LEED of Si(111)-5×2-Au. The yellow arrows mark the ×2 streaks.

Table 5.1: Coverages of Au required for the optimum "5×2" reconstruction.

Surface	**Coverage (ML)**	**Error (ML)**
Si(557)-Au [98]	0.18	0.01
Si(111)-5×2-Au (3° to $[\bar{1}\bar{1}2]$)	0.44	0.04
Si(111)-5×2-Au (4° to $[11\bar{2}]$)	0.46	0.04
Si(775)-Au [191]	0.32	0.02

$[\bar{1}\bar{1}2]$ direction and Si(775)-Au. These results are shown in table 5.1. Evidence supporting the new three Au chain model for Si(111)-5×2-Au [24] comes from detailed analysis of these coverages. By assuming that the Si(111)-5×2-Au structure, grown on Si(111) 4° off-cut in the $[11\bar{2}]$ direction, is a simple geometric combination of the singular Si(111)-5×2-Au and the Si(775)-Au surfaces, values of 47% Si(775)-Au and 53% Si(111)-5×2-Au are obtained. The coverage in table 5.1 then produces a value of optimum coverage for the singular Si(111)-5×2-Au of 0.58 ± 0.06 ML, agreeing within error with the value of 0.60 ML for the new three Au chain model [24].

Figure 5.10 shows that the full spectrum of Si(111)-5×2-Au, off-cut by 4° towards $[11\bar{2}]$ can be reasonably reproduced by taking 47 % of Si(775)-Au and 53 % of Si(111)-5×2-Au, off-cut by 2° towards $[\bar{1}\bar{1}2]$. A "pure" Si(111)-5×2-Au RAS spectrum cannot be measured by RAS because the singular surface will normally produce three domains of equal population, giving no RAS signal due to macroscopic averaging.

The step structure and faceting nature of samples off-cut in the $[\bar{1}\bar{1}2]$ direction are not as well known as in the $[11\bar{2}]$ direction, so to calculate the ideal coverage for the Si(111)-5×2-Au surface it is assumed that, in the region of the step, a chain structure similar to that on Si(557) will form (figure 5.26). This would mean that the 3° sample will consist of 32% step-related structures. The coverage of Au needed for a perfect Si(111)-5×2-Au can then be calculated. From the 3° sample a figure of 0.56 ± 0.06 ML is calculated. For Si(775)-Au, table 5.1 shows a value of 0.32 ± 0.02 ML, consistent with current structural models [191].

5.4.3 Annealing temperature dependence on the formation of Si(111)-5×2-Au

Figure 5.11 shows the effect of annealing temperature on ∼ 0.43 ML of Au, corresponding to a complete 5×2 phase deposited on Si(111) 4° off-cut in the $[11\bar{2}]$ direction at room temperature, together with the result of optimized deposition and annealing at 425 °C. The sample was held at these various temperatures for about

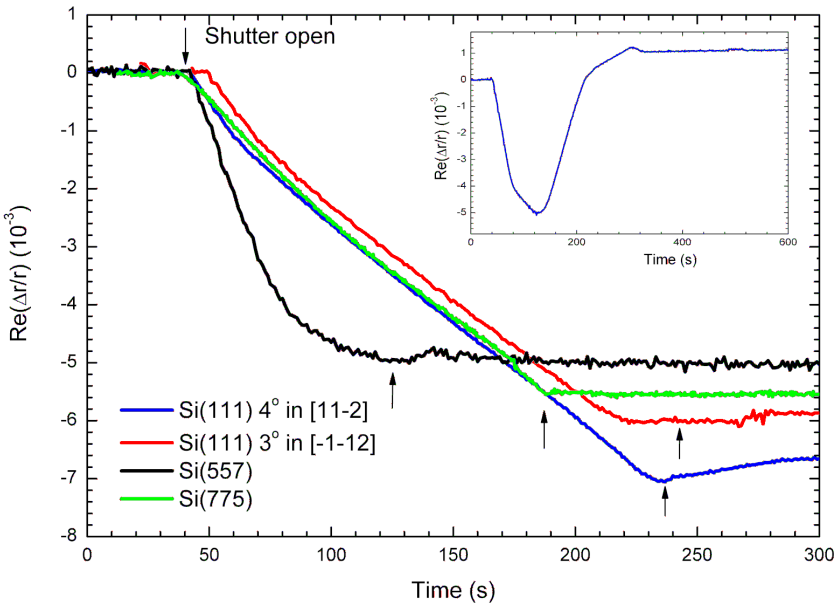

Figure 5.9: 2.5 eV transient of Au deposition on Si(111) off-cut by 4° in the [11$\bar{2}$] direction, Si(111) off-cut by 3° in the [$\bar{1}\bar{1}$2] direction, Si(557) and Si(775). This demonstrates RAS's usefulness as an *in situ* surface probe and has been used to calculate the optimum coverage of Au for various Si(111) off-cuts. The inset shows Si(557) during continuing Au deposition where a well defined minimum associated with the completion of the Si(557)-Au chain structure is clearly seen.

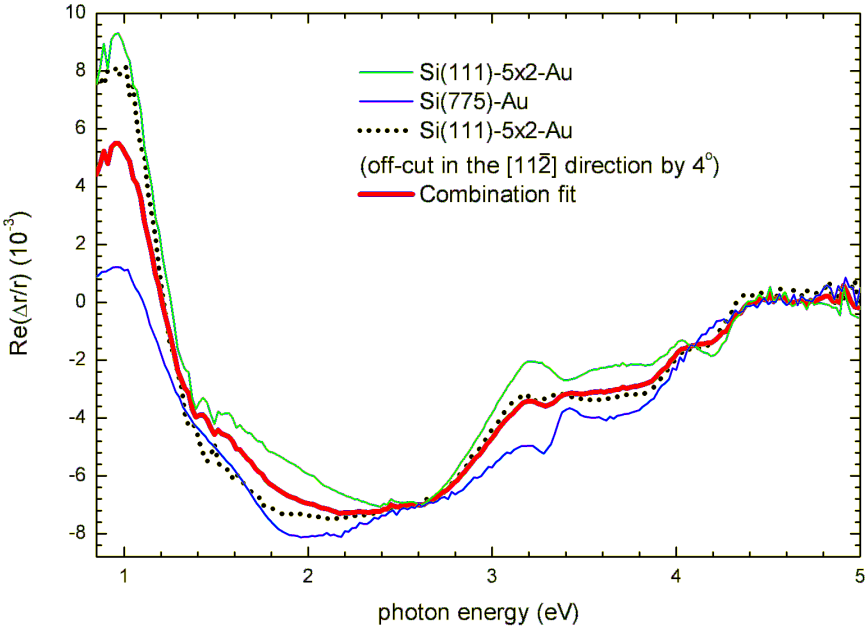

Figure 5.10: A combination of 47% Si(775)-Au and 53% Si(111)-5×2-Au giving a good fit for Si(111)-5×2-Au off-cut by 4° in the [11$\bar{2}$] direction

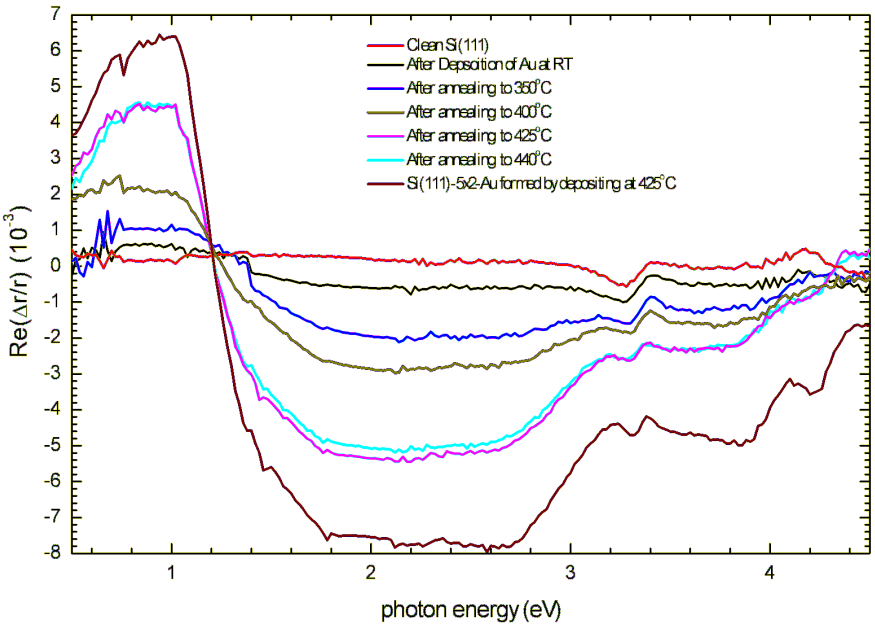

Figure 5.11: RAS spectra recorded on Si(111) sample off-cut by 4° in the [11$\bar{2}$] direction after annealing at various temperatures.

20 min, until no further change in the RAS response was observed. The amplitude of the anisotropic surface and interface RAS signal will, in general, be reduced by defects, disorder and by domain averaging.

It can be seen that annealing at 425 °C is necessary to produce a well ordered surface phase, but that the combination of both deposition and annealing at 425 °C produces the best result. This is consistent with previous STM work that indicated that Si atoms become mobile above about 250 °C [192], and that deposition at 400 °C allows the formation of the equilibrium 5×2 structure, which contains an average of one Si adatom per four unit cells [193]. Figure 5.11 shows that significant ordered regions are formed as low as 350 °C. In figure 5.12 the amplitude of the minimum at 2.2 eV is plotted against the amplitude of the maximum at 1 eV, using the data of figure 5.11. The linear fit indicates that only one anisotropic ordered structure is being formed.

5.4.4 Adatoms on Si(111)-5×2-Au

It has been shown by Choi *et al* that by depositing Si adatoms on the Si(111)-5×2-Au surface and subsequently annealing that adatom sites can be populated in a range from 100% to 30% [55]. RAS spectra were recorded for the as deposited 5×2, a 100% adatom filled "5×4" and after varous annealing temperatures. RAS spectra

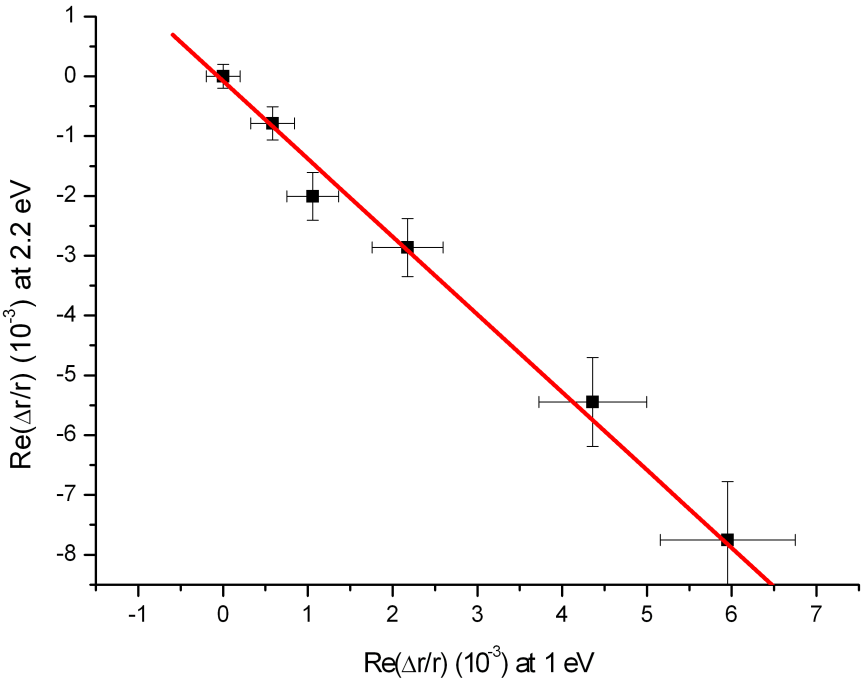

Figure 5.12: The amplitude of the minimum at 2.2 eV plotted against the amplitude of the maximum at 1 eV. The linear fit indicates that only one anisotropic structure is forming, within experimental error.

were also recorded for a sample where double the amount of adatoms required to fill all the available sites was deposited.

It is known that as deposited Si(111)-5×2-Au has a population of approximately 0.025 ML of Si adatoms [36, 55, 175]. Figure 5.13 shows the RAS signal after depositing an additional 0.025 ML of Si and 0.075 ML of Si, equivalent to the ideal amount for the "5×4" or one adatom per two 5×2 [24, 35, 37, 54, 179] unit cells and to double the ideal amount or one adatom per 5×2 unit. It can be observed that the RAS structure is significantly dampened but there are only minor changes in the shape of the RAS signal with mainly some loss of the fine structure around 1.5 eV. These changes can be explained by assuming that the adatoms stick where they land on the 5×2 surface and do not find their minimum potential energy position. They will be randomly distributed throughout the surface removing some of the surface anisotropy.

When this adatom decorated structure is annealed at 350°C for 15 min the RAS signal changes drastically (figure 5.14). The broad minimum from 1.5 eV to 2.6 eV is replaced by a maximum at 1.6 eV with a large shoulder at 2.2 eV. The maximum at 1 eV is replaced by a minimum at 1.1 eV. Upon heating to 415°C for 15 min these

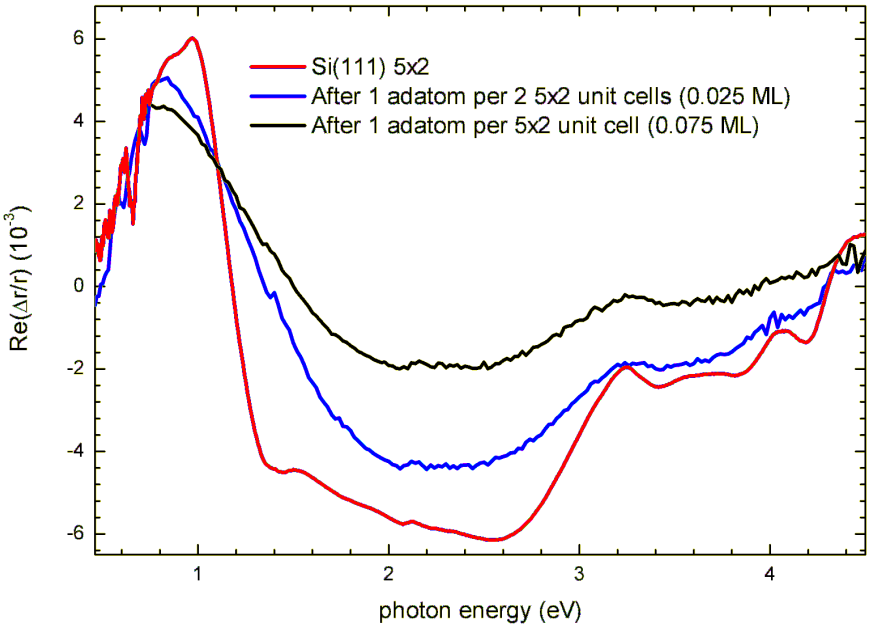

Figure 5.13: RAS signal of Si(111)-5×2-Au, Si(111)-5×2-Au with 0.025 ML of additional adatoms and Si(111)-5×2-Au with 0.075 ML of additional adatoms.

structures become larger and more defined. Both these results would indicate that the Si adatoms now have enough energy to become mobile and find their minimum potential energy positions. This large change in RAS signature has been hinted at in band structure calculations for this surface, which show that chains with no adatoms are metallic while chains covered with adatoms become semiconducting (figure 5.16). The surface where one adatom per 5×2 unit cell was deposited shows very similar behavior, but with all the structures reduced in intensity (figure 5.15). This would indicate that, at these temperatures adatoms are not being desorbed but simply diffuse across the surface. When there are too many adatoms they sit in sites not associated with the "5×4" adatom reconstruction and remove some of the surface anisotropy.

Upon annealing to higher temperatures adatoms are removed from the surface and the RAS signal comes back to the original signal seen for Si(111)-5×2-Au (figure 5.14). However, when the sample is flash heated for 10 s to 990°C the RAS signal changes slightly in the region of the maximum at 1 eV (figure 5.17). Adatoms are removed by flashing to these high temperatures [55] so these small changes can be explained as the surface going from ∼45% adatom sites filled to ∼30% adatom sites filled. After flashing to 1050°C some Au is removed from the surface and the RAS signal is reduced.

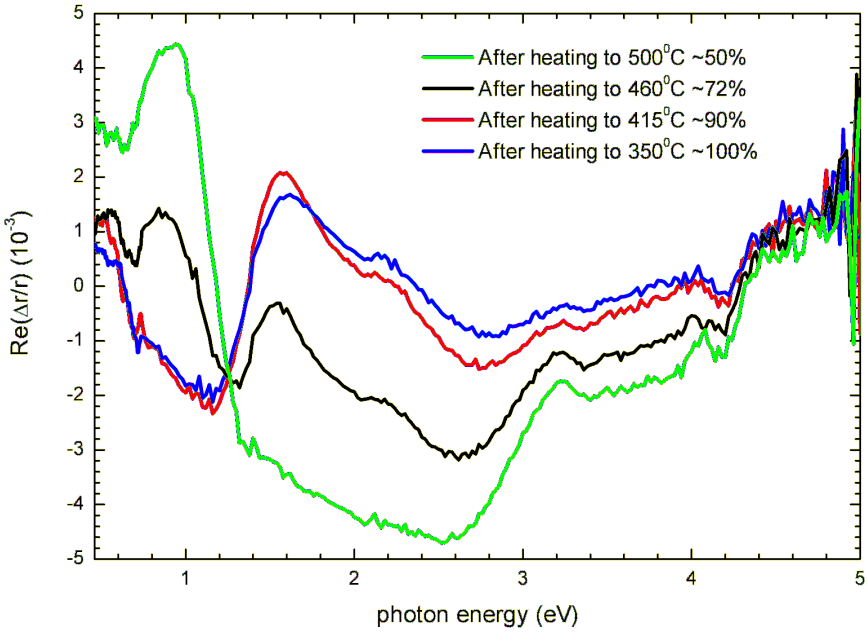

Figure 5.14: RAS signal from Si(111)-5×2-Au with 0.025 ML of additional adatoms after annealing to various temperatures. At these temperatures, the pyrometer error is estimated at ±50°C. The estimates of adatom site filling come from the method illustrated in figure 5.19.

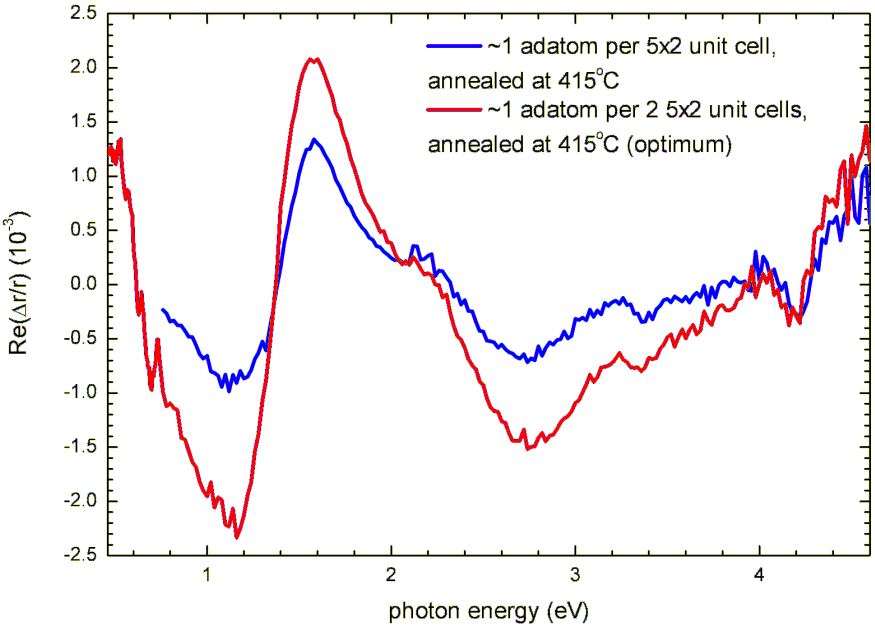

Figure 5.15: RAS signal after depositing 0.025 ML of Si (optimum) and 0.075 ML of Si and annealing to 415°C.

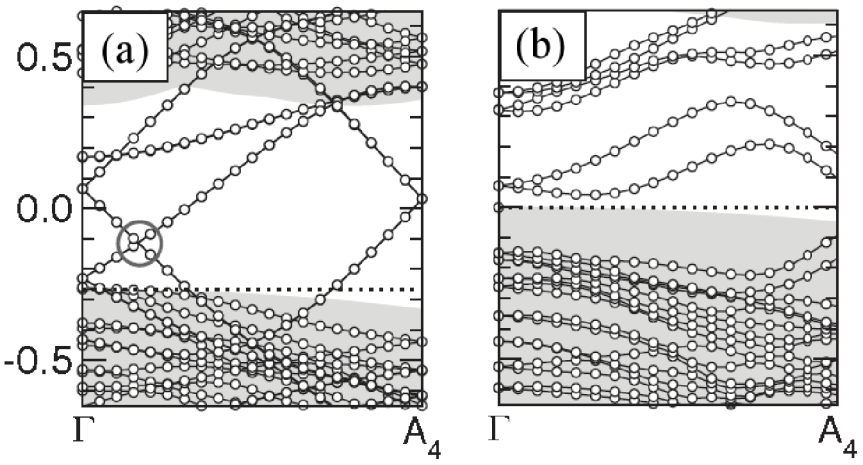

Figure 5.16: (a) Bandstructure of an undecorated Si(111)-5×1-Au surface from first principles *ab initio* calculations. (b) Bandstructure of adatom covered Si(111)-5×4-Au. The large circle shows the band crossing in the Si(111)-5×1-Au surface which causes it to have metallic behavior. In the adatom covered Si(111)-5×4-Au bandstructure, a gap has clearly been opened due to the electron doping by the Si adatoms (after [24]).

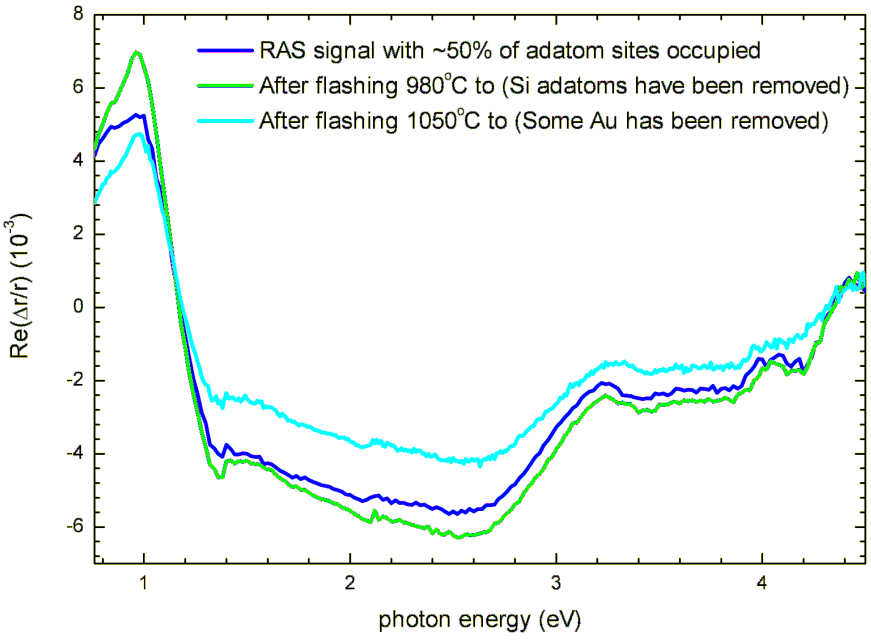

Figure 5.17: RAS signal from Si(111)-5×2-Au after flashing to high temperatures. The error on the temperatures is ±25°C.

By assuming that the RAS signal from the sample that had been annealed at 415°C has 90% of its adatom sites occupied, and that the as-deposited Si(111)-5×2-Au has 45% [36, 55, 175] of its sites occupied it is possible to extract a 100% adatom sites occupied and a 0% adatom sites occupied RAS signal (figure 5.18). As a test, the RAS signal from the sample annealed with adatoms at 460°C was fitted using a least squares fit where the percentage of filled adatom sites was allowed to vary. A value of 72% gave an excellent fit to the RAS signal (figure 5.19). The signal from the 0% adatom coverage shows a broad flat minimum from 1.4 eV to 2.8 eV, with a sharp transition to a narrow maximum at 1 eV. The signal from the 100% adatom coverage has a maximum at 1.6 eV with a large shoulder at 2.1 eV and a minimum at 1.1 eV. The dramatic difference in the spectral signatures of the 0% and 100% adatom-filled structures represents a severe challenge for *ab initio* calculations of the RAS response. Some progress is being made and this is discussed in chapter 6. A bandgap of ∼0.3 eV for the 100 % adatom-filled structure has been predicted by Ren *et al* [194], while Yoom *et al* [180] and Erwin *et al* [24] predict a gap of ∼0.6 eV. Choi *et al* have observed the top of the valence band at 0.3 eV below the Fermi level, giving a gap of 0.6 eV if the valence and conduction band are positioned symmetrically areound the Fermi level. Figure 5.15 and 5.18 suggest that the gap could be ∼ 1.0-1.4 eV, but this would require a conduction band 0.7-1.1 eV above the Fermi level. It is more likely that the band gap opening will not be seen until the spectral range of the RAS system is extended to ∼0.3 eV.

5.4.5 Capping of Si(111)-5×2-Au

The Si(111)-5×2-Au was capped with up to 4.6 nm of amorphous Si (a-Si) at room temperature to see if the RAS signature remained. This was to extend the results obtained by Iwasawa *et al* [42], who showed that the Au retains its 5×2 reconstruction under the a-Si cap. Figure 5.20 shows the RAS signal from Si(111)-5×2-Au before capping, after 0.5 ML of a-Si and after 4.6 nm (∼15 ML). It can clearly be seen that the RAS signal is removed by capping even with just 0.5 ML of a-Si. This indicates that the technologically interesting anisotropic behavior is related to surface states that are quenched by the capping material. This is an interesting result showing that the retention of crystallographic structure at the interface on capping does not provide evidence that the principle features of the electronic structure are maintained: epioptic probes like RAS can provide this information [9].

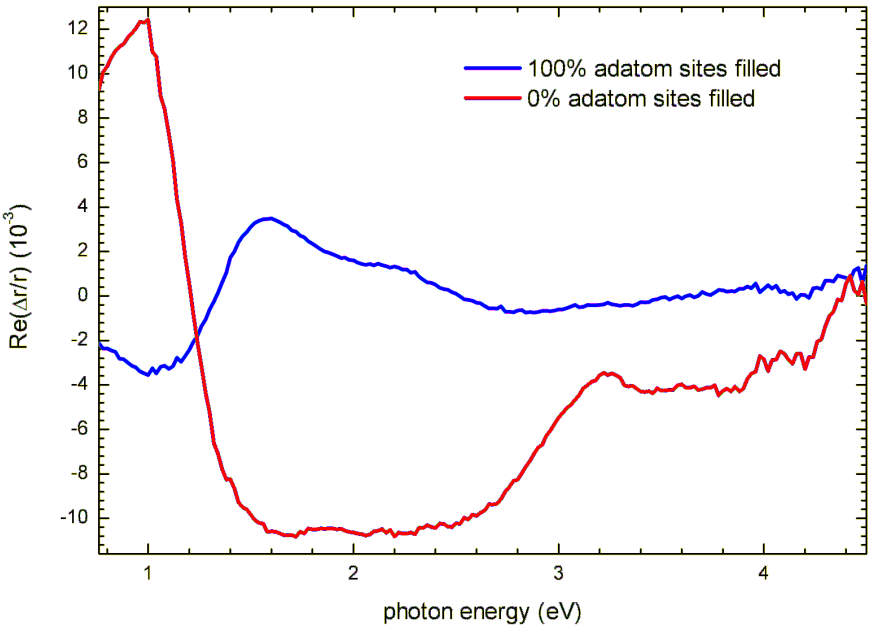

Figure 5.18: Calculated RAS signal from 0% adatom sites filled and 100% adatom sites filled, for Si(111)-5×2-Au formed on Si(111) off-cut by 2° towards [$\bar{1}\bar{1}2$].

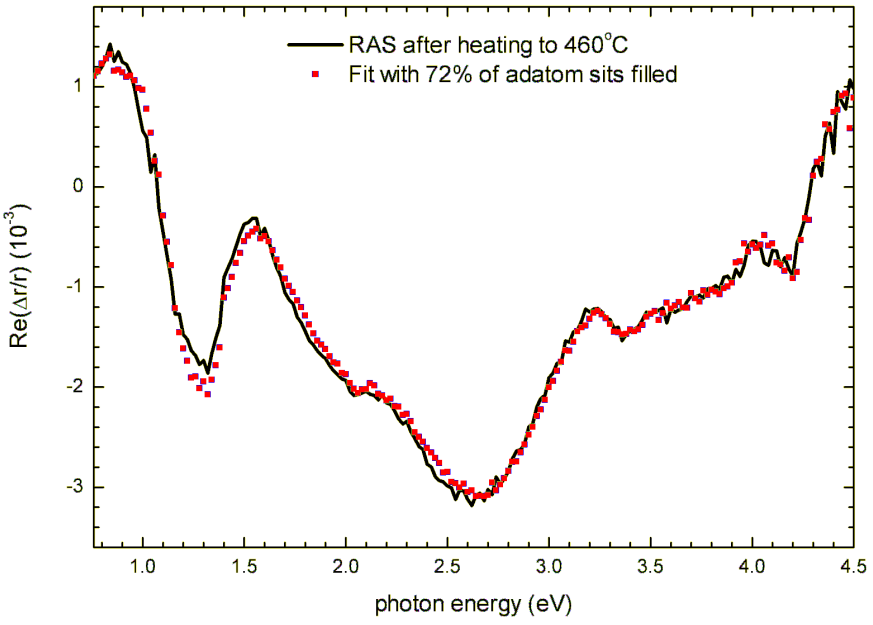

Figure 5.19: RAS signal from adatom decorated Si(111)-5×2-Au annealed at 460°C, fitted by using a combination of 72% adatam sites filled, 28% unfilled.

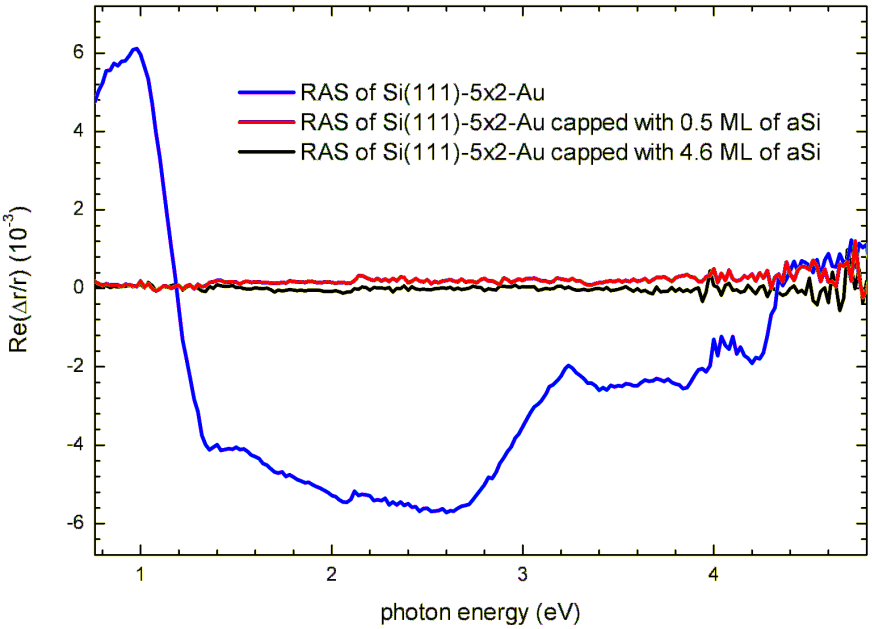

Figure 5.20: RAS spectra from Si(111)-5×2-Au, Si(111)-5×2-Au capped with 0.5 ML and Si(111)-5×2-Au capped with 4.6 ML of a-Si.

5.4.6 Comparison with previous work

The only other RAS work on the Si(111)-5×2-Au system was reported by Power *et al* in 1997 [38]. Their RAS spectra (figure 5.21), Si(111)-5×2-Au off cut by 4° in the $[11\bar{2}]$ direction shows significant differences from the RAS spectra presented here for the same surface. The features at 3.4 and 4.25 match but they did not see the broad minimum between 1.4 eV and 2.8 eV and, due to the limits on their spectral range, could not see the maximum at 1.1 eV. However, the work here has shown that the RAS signal is strongly dependent on processing conditions (figure 5.11), off-cut direction and angle, faceting (figure 5.10) and number of adatom sites filled (figure 5.18). It is likely that the surface they produced was quite different to those discussed here.

5.5 The Si(775)-Au reconstruction

The Si(775)-Au reconstruction occurs after deposition of 0.32-0.35 ML of Au [30, 191, 195]. The current model (figure 5.22) consists of a Si honeycomb chain with a double Au chain both running parallel to the steps on the surface [30]. Adatoms are not found to stabilise this structure, unlike the Si(111)-5×2-Au reconstruction. The surface reconstruction is believed to be semimetallic with only the band maximum touching the Fermi level [30]. There have been no studies of this surface at low

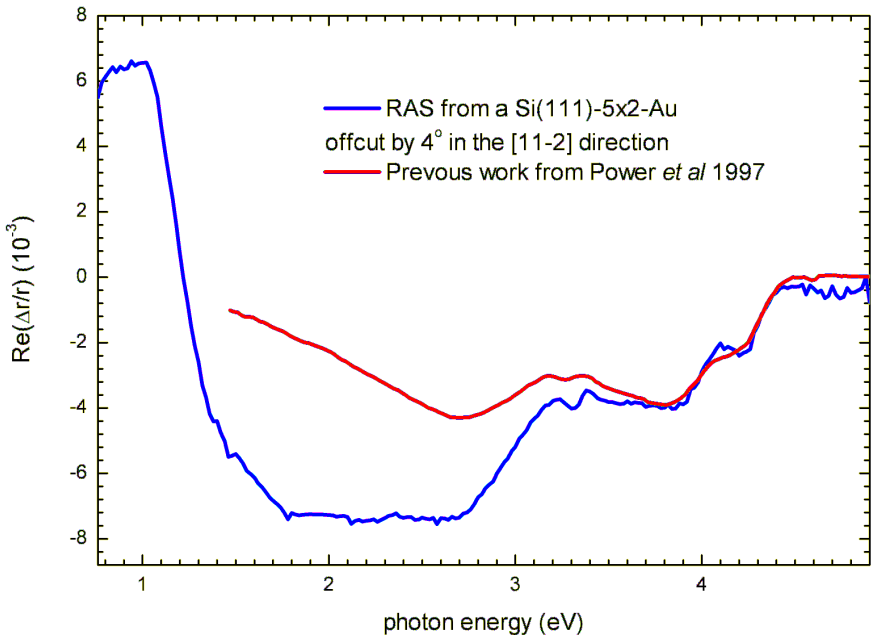

Figure 5.21: A comparison between previously published RAS spectra on Si(111)-5×2-Au, off-cut by 4° in the [11$\bar{2}$] direction, and the this work.

temperature so no conclusions have been drawn about whether it will undergo a Peierls distortion. The surface bands are strongly one dimensional and there is an inherent buckling of the Au chains, so it might be expected. The ratio of intrachain to interchain coupling strength is over 100 for Si(775)-Au, compared to ∼10 for three-dimensional chain structures, such as the Bechgaard salts [196].

5.5.1 RAS results and discussion for Si(775)-Au

The RAS spectrum from Si(775)-Au is shown in figure 5.23. The RAS spectrum has the same features as Si(111)-5×2-Au, but the line shape is quite different. The minimum between 1.8 and 2.8 now has a clear minimum position at 1.9 eV. RAS spectra of similar surfaces such as Si(111)-3×1-Ag and Si(111)-4×1-In show the same minimum in a similar energy position (figure 3 in [143]). In the case of Si(111)-4×1-In recent *ab initio* calculations have shown that the minimum is due to both Si-In and pure In states [197]. If this is also true of the Si(111)-5×2-Au surface, the change in distribution of Si-Au and pure Au states, as we move from the three chain Si(111)-5×2-Au system to a two chain Si(775)-Au system, would effect the line shape of the RAS spectra in the region around the minimum.

It is also of note that the maximum between 0.7 and 1.0 eV, while quite reproducible, is much less pronounced for these substrates than for the 4° or 2° off-cut.

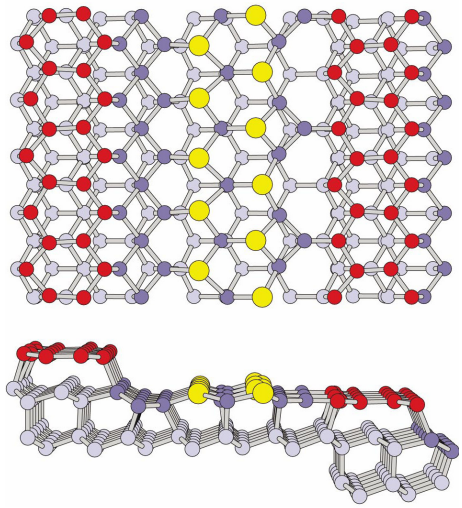

Figure 5.22: Structural model for Si(775)-Au (after [30]). Gold atoms are yellow and the Si honeycomb chain is red.

The width of the terraces in figure 5.22 is roughly half that of the 4° off-cut, making the chain structures on these narrower terraces more sensitive to the presence of kinks. The average length of the Au chains is thus expected to be significantly shorter on the Si(775)-Au, as the kinks will terminate the Au chains more efficiently than on the 4° off-cut. It thus appears possible that the size of the maximum between 0.7 and 1.0 eV is related to the length of the Au chains. If confirmed, this will raise interesting possibilities for the *in situ* monitoring of nanowire growth and, possibly, process control.

5.5.2 Ad-atoms on Si(775)-Au

The effect of depositing a-Si on the Si(775)-Au system was investigated. Figure 5.24 shows the Si(775)-Au RAS response, together with the effect of a-Si deposition at room temperature. The Si(775) was chosen because, as mentioned above, it has one-dimensional (1-D) metallicity and its equilibrium structure is not normally perturbed by intrinsic adatoms. Deposition of 0.05 ML (0.5 adatoms per 5×2 unit cell) reduces the size of the minimum by about a factor of two, while the maximum increases by a similar factor. The spectral shape now resembles the RAS from the 4° off-cut in the $[11\bar{2}]$ direction (figure 5.11). The Si atoms are not expected to diffuse on deposition at room temperature and thus the average population of Si adatoms per unit cell can be estimated [193]. The error in coverage due to the thermal drift of the quartz crystal oscillator (cross-calibrated against Si(557)-Au, Table 5.1) can be estimated at about 0.02 ML, meaning an error of ∼0.25 atoms per 5×2 unit cell.

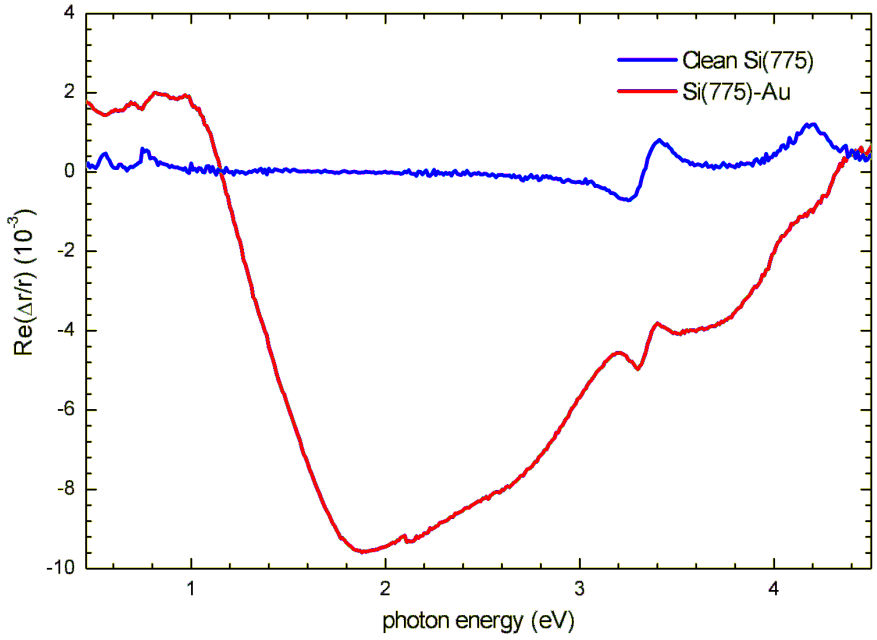

Figure 5.23: RAS spectra from clean Si(775) and Si(775)-Au.

Above the 0.5 adatoms/unit cell no further changes in shape of the RAS spectra are seen, the structure is simply damped. At 1/3 of a monolayer all of the anisotropic structure due to the wires are gone and all that is left is the step modified bulk states of Si.

5.5.3 Capping of Si(775)-Au

As discussed in the previous section, above 1/3 ML coverage of a-Si there is no anisotropy due to the Au wires on the Si(775) surface. Deposition continued until the coverage of 4.6 nm, that used by Iwasawa *et al* [42], was reached. Only the step-modified bulk optical transitions remain (figure 5.25). These features progressively reduce in size and red-shift, most likely due to the optical absorption and the strain increasing with capping layer thickness [198]. While surface X-ray diffraction shows that the crystal structure of the 5×2 phase is largely unchanged by capping with a-Si at room temperature [42], it is clear from these results that the technologically important anisotropic properties of the metallic chains have been destroyed.

5.6 The Si(557)-Au structure

A lot of the interest in vicinal Si(111)-Au systems has come from the fact that they are excellent test systems for 1-D physics (chapter 2). Si(557) is considered to be

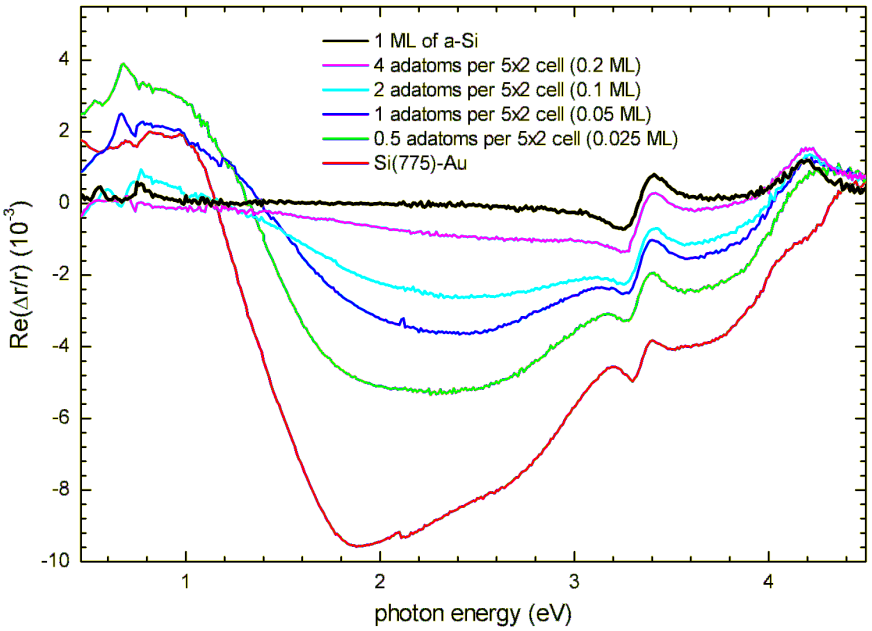

Figure 5.24: RAS spectra from Si(775)-Au as Si adatoms are added up to 1 ML of Si.

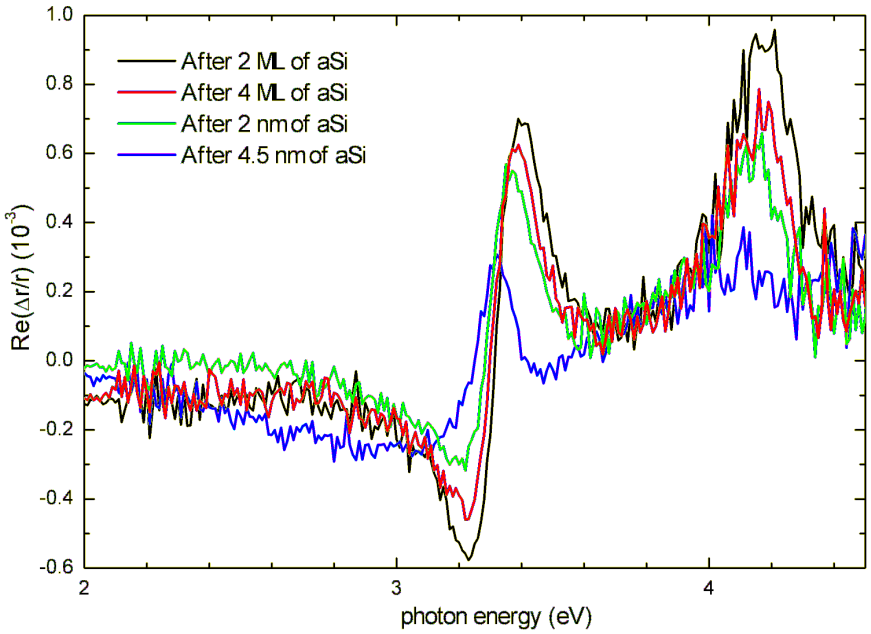

Figure 5.25: RAS spectra from Si(775)-Au as it is capped with a-Si.

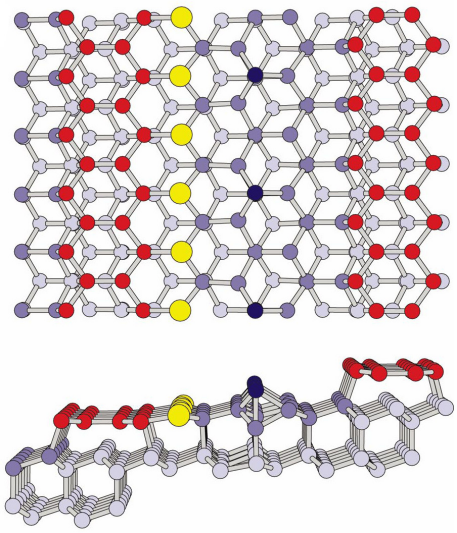

Figure 5.26: Structural model for Si(557)-Au , after [30].

a very good 1-D system, as measured by considering the ratio of the strength of intrachain to interchain interactions (over 60 for the Si(557)-Au surface) [15, 30]. Its structure is well understood and consists of a Si honeycomb chain, a re-bonding row of Au and a row of Si adatoms (figure 5.26 [30, 199, 200]). The system is believed to be conducting in the region from 80K to 300K and no Peierls distortion can be reproducibly seen [92, 201]. Some STM experiments have claimed to see a Peierls distortion [90] at low temperature but these results have now been explained as simply an increase in resolution [95]. The system has two 1-D bands that cross the Fermi level and initially these were believed to be a sign of spin charge separation [31]. Later this claim was disproved and the bands were assigned to a spin-orbit split state [32, 202]. The STM of Si(557)-Au shows 2 bright rows [93], neither of which is related to the Au chain [200] (figure 5.27). The bright rows are in fact related to the Si adatoms and Si step atoms.

5.6.1 RAS results and discussion for Si(557)-Au

RAS on clean Si(557) is very interesting, consisting of the normal peaks at 3.4 eV and 4.25 eV ,associated with the step modified bulk states, and a unusual peak at 1.2 eV (figure 5.28). It is possible that the Pandey chains that form on the Si(111)-2×1 surface [203] also form on this surface. However, the optical response of these chains is seen at much lower energy (∼0.5 eV [204]) and a more likely explanation is that it is a surface state related to the $[\bar{1}\bar{1}2]$ oriented triple step structure [117] (chapter 6).

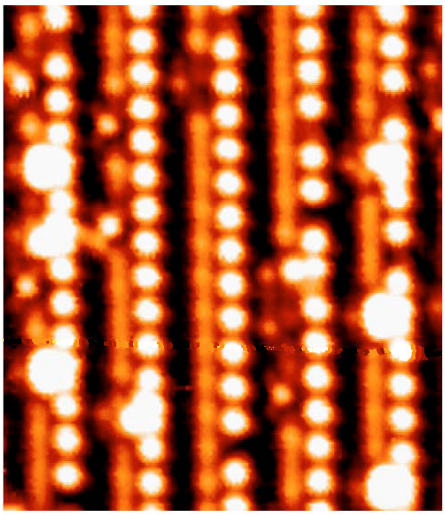

Figure 5.27: STM of Si(557)-Au, two distinct chains are visible related to the Si adatoms and Si step sites, the image is 9.75 × 13.5 nm, after [93]

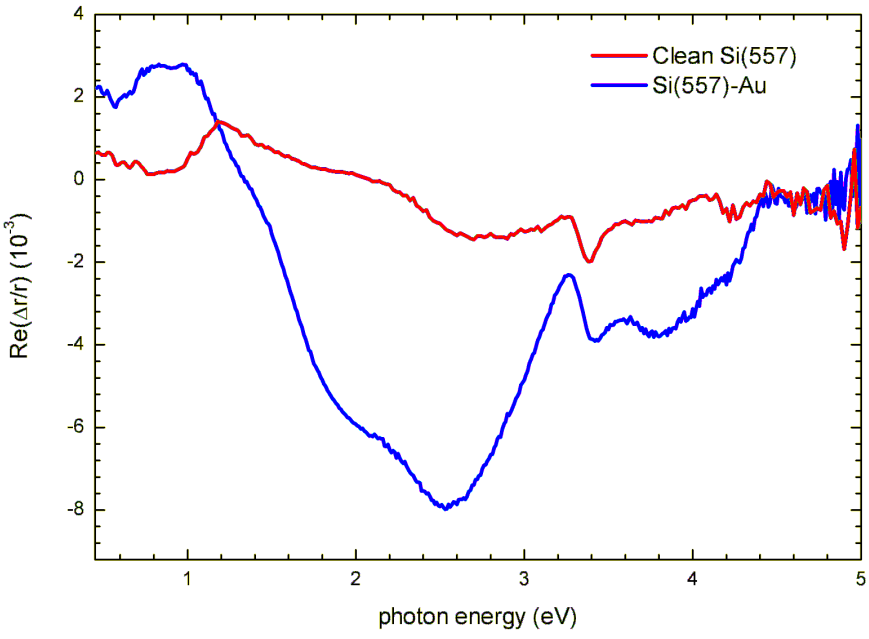

Figure 5.28: RAS of clean Si(557) and Si(557)-Au.

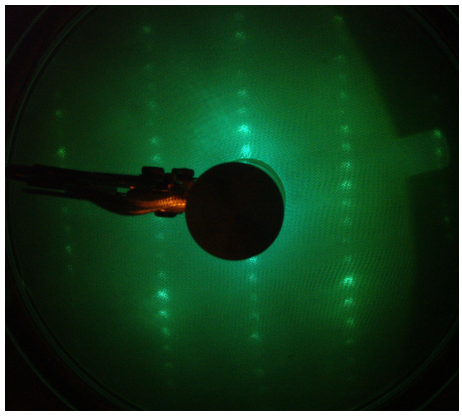

Figure 5.29: LEED of Si(557)-Au.

The RAS signal on Si(557)-Au again has the same features as the Si(111)-5×2-Au surface but the line shape is quite different (figure 5.28). The minimum has its peak at 2.8 eV with a large shoulder at 2 eV. The maximum below 1 eV is only about 25% of the singnal seen on lower angle off-cut Si(111)-5×2-Au. As discussed for the Si(775)-Au surface, the change in line shape of the minimum would be expected due to the change in proportion of Si-Au and Au-Au states, as the sample goes from a triple chain Si(111)-5×2-Au system to a single chain Si(557)-Au surface. The lack of a peak in the IR could be again explained by kinks preventing long chains from forming.

The LEED pattern on Si(557)-Au is interesting as it does not show the ×2 lines that are seen on the Si(111)-5×2-Au surface (figure 5.29). The Crain model [30] predicts this and often the Si(557)-Au surface is called Si(557)–5×1-Au. In this work the term Si(557)-Au has been used to prevent confusion with the early Bishop and Riviere work which mistakenly called the Si(111)-5×2-Au, "5×1".

5.7 Summary

A strong optical anisotropy was seen on the Si(111)-5×2-Au surface, which is related to the chain structures on the surface. By taking into account the areas of the surface associated with steps, the coverage for a perfect singular Si(111)-5×2-Au surface has been calculated. Coverages of $\sim$ 0.6 ML were found, consistent with the new three chain model proposed by Erwin *et al* [24]. The RAS signal from a Si(111)-5×2-Au off-cut by 4° in the $[11\bar{2}]$ direction surface could be reasonably reproduced by combining 53% of the pure 5×2 signal with 47% Si(775)-Au signal, in good agreement with the geometric proportions. The minimum temperature for the formation of Si(111)-5×2-Au was found to be 425°C. When adatoms were

deposited on the Si(111)-5×2-Au surface at room temperature the RAS spectra was consistent with their being immobile. Subsequent heating caused the RAS signal to change drastically, as that the adatom decorated "5×4" reconstruction was formed. Temperature dependent studies allowed a 100% adatom sites filled RAS spectra and 0% adatom sites filled RAS spectra could be extracted. Upon capping the Si(111)-5×2-Au surface the optical anisotropy was removed

A strong optical anisotropy was also seen on the Si(775)-Au surface. It had many of the same features as the Si(111)-5×2-Au RAS signature but the line shape was significantly different. Upon capping the Si(775)-Au surface the optical anisotropy was also removed, however the signal around the bulk critical points of Si remained and shifted to lower energy as the capping layer got thicker. Clean Si(557) shows a strange optical anisotropy in the region of 1.2 eV the origin of which may be the triple step structure. Si(557)-Au shows a similar optical anisotropy to Si(775)-Au and Si(111)-5×2-Au, but again the line shape is visibly different.

The RAS line shapes of these related Au chain structures are likely to provide a severe test for *ab initio* optical response calculations.

6 *Ab initio* calculations of the optical response of Si(557) and Si(775)

Preliminary optical response calculations have been undertaken in a collaboration with Dr. Conor Hogan, under the auspices of the European Theoretical Spectroscopy Facility.

Clean Si(557) forms an interesting structure with a (111) terrace separated by a series of steps. The terrace is expected to have a 7×7 reconstruction, possibly with some minor modifications due to it being confined on a narrow terrace. These terraces are separated by a triple-step structure. The surface can be uniform over a long range, forming an almost grating like structure with a period of 5.73 nm [116]. After joint STM and DFT studies were carried out [117], the triple step structure was initially thought to have a (112) orientation. However, some doubt has been cast over this assignment [205] with recent LEED studies claiming its has (113) orientation [206] and high resolution STM work indicating that the surface may in fact have a (77 10) orientation with the triple step being a combination of a double step and a single step [207]. Recent work by Chaika *et al* may have explained some of these discrepancies, as they found that the Si(557) surface can form several regular step reconstructions, depending on the preparation conditions [208].

The RAS signal from the clean Si(557) shows the usual step modified bulk states at 3.4 eV and 4.25 eV, but also shows a large peak at 1.2 eV (figure 6.1). The origin of this peak is unknown. An optical response in the IR is seen for Pandey chain structures on Si(111)-2×1 [203], however the RAS signal from these chains are seen at lower energy (∼0.45 eV) [140]. An attempt has been made to calculate the RAS signal from first principles from this surface, and Si(775), using DFT-LDA [209]. Since the Si(111)-7×7 surface is isotropic, it was assumed that the RAS signal would be dominated by the Si(112) orientated triple step response, or a state at the step edge.

As RAS is a local probe of the surface electronic structure, it is sensitive to structural features that may be present on the Si(557) surface. These features could include dimers (both parallel and perpendicular to the step edge), adatoms, buckling, π-like chain states, and dangling bond states localised at the step edge. *Ab initio* calculations of the optical response may help to suggest or reject possible surface structures [209].

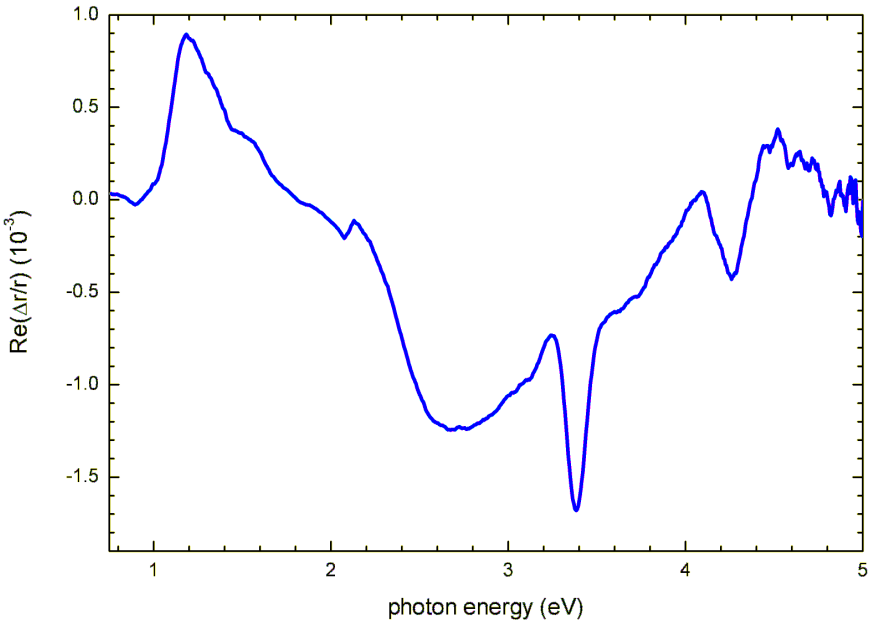

Figure 6.1: RAS spectra of clean Si(557).

6.1 Details of the calculations

Two different approaches were taken for modeling the clean Si(557) surface. The simplest approach took reconstructed and relaxed Si(557) surface. For comparison a Si(775) surface, which shows no evidence of step bunching, was also studied using this method. The second approach examined the Si(112) surface structures described by Oh *et al* [117], who studied various bulk truncated models of the Si(112) surface [117]. Several different surface motifs were examined including dimers parallel ($D_{\parallel}$) and perpendicular ($D_{\perp}$) to the step edge and a variation of $D_{\parallel}$ containing adatoms in a regular ($AD_{\parallel}$) or oblique ($AD'_{\parallel}$) cell.

Using DFT-LDA simulations of these models and some similar variations, the total energy of the system and the optical properties were computed. The total energy was calculated using the PWscf code [210] and the optical properties were calculated using the Yambo code [211]. A slab approach was employed where seven Si(111) double layers were included and this was separated by 1 nm of vacuum from the next slab, to prevent interference affects. A 1×2 cell was used for the Si(112) surface and the symmetry was not restricted during the calculation. Hydrogen atoms were used to terminate the back surface and their nearest and next nearest neighbours were fixed to the Si bulk positions during the structural relaxation. When the surface had converged, a 72 k-point computation of optical properties was used, and the optical signal was extracted from the first five layers using the

method described by Hogan *et al* [212]. Larger numbers of k-points were also tested to determine the convergence of the optical properties. It was found that more k-points were often needed to accurately reproduce features at higher energy.

Many body corrections were accounted for, in an approximate way, by using a rigid band shift of +0.5 eV to the conduction bands. This method was developed by Del Sole and Girlanda [213] and accounts for both single particle self energy corrections and two particle excitonic effects in an approximate way. The value of +0.5 eV works well for bulk Si, but may not produce accurate shifts in conduction band for localised surface states, in particular at energies near the Fermi level [105].

6.2 Results

For Si(557), the truncated bulk model, after relaxing the structure, predicted two surface motifs, a π bonded Pandey chain, running parallel to the steps on the surface, and a dangling bond state localised on the step edge. For the Si(775) surface, a chain-like structure perpendicular to the steps was predicted. The different motifs on the two similar surfaces could come from the slightly different width of the terrace or, more likely, from the opposite orientation and the different bonding of the step atoms (figure 3.1). The Si(557) and Si(775) reconstructed surfaces were both found to be metallic with weakly dispersive surface bands crossing the Fermi level. In both cases there are many states inside the bulk band gap of the Si, while Si(557) was found to have fewer surface states than Si(775).

The surface energies for the various models of the Si(112) surface, were computed using

$$E_{\text{surf}} = E_{\text{slab}} - N_{\text{Si}} E_{\text{bulk}}. \tag{6.1}$$

where E_{slab} is the total energy of the slab obtained from the super-cell calculation, N_{Si} is the number of Si atoms and E_{bulk} is the energy (chemical potential) of a bulk silicon atom. The results are presented in table 6.1 and match well with what was found by Oh *et al*, indicating that the most stable structures are the ones with adatoms [117]. However, in contrast to the work by Oh *et al*, it was found that the difference between oblique and regular cells is small. The result could be due to a buckling of the dimers at the step edge that was seen here but not observed in Oh *et al*'s work. The buckling could be related to a similar buckling that has been observed experimentally on Si(557)-Au [95].

Table 6.1: Computed surface energies of different Si(112) structural models, including the reordered bulk truncated (RBT) model.

	RBT	$D_\perp$	$D_\parallel$	$AD_\parallel$	$AD'_\parallel$
ΔE_{surf} (eV)	0.00	-0.58	-0.62	-0.78	-0.79

6.3 Predicted optical spectra

As is often the case with Si surfaces, the computed RAS response has amplitudes significantly larger than those observed experimentally. The RAS data are therefore scaled by a factor of 5 for comparison with the predicted spectra. The predicted RAS signal from the Si(557) relaxed truncated bulk model is compared to the experimental in figure 6.2. Analysis of the main peaks shows that there are four main contributions S_2, S_3, M_4 and M_5. The S_2 structure derives from π-bonded Pandey-like chains. The S_3 structure comes from a dangling bond state localised on the step edge. The M_4 transition comes from a mix of bulk states and surface resonances. The M_5 transition, is a surface modified bulk state. It is only reproduced in the calculation when a high density of k-points are used. The signal at 4.25 eV in the RAS spectra is thought to be of a similar origin but is not reproduced in the calculations. In figure 6.4 the oscillations in this region are not related to the transitions at 3.4 eV and 4.25 eV, but are an artifact of a low number of k-points used and the slab approach. Although the agreement between theory and experiment is good for these initial calculations, the uncertainty in the self-energy correction means that the experimental peak at 1.2 eV could be assigned to either S_2 or S_3.

Preliminary results for the Si(775) truncated bulk model do not compare well to the experimental spectrum (figure 6.3). The calculated spectra show a large negative peak at low energies associated with the chain-like structures running perpendicular to the steps. No experimental RAS features were seen in this region. It is possible by that by adding adatoms or other defects that this structure will be quenched, but further work is clearly required.

The predicted optical spectra for the various Si(112) models are shown in figure 6.4. It is clear that overall agreement with the experimental RAS signal is quite poor. The energetically most stable models, those with the adatoms, show no significant positive anisotropy in the region of 1.2 eV, in fact both show a slight negative anisotropy in this region (figure 6.4 (b)). Of the other 3 models, only the dimer rows parallel model ($D_\parallel$), is similar to the experimentally observed signal below 2 eV (figure 6.4 (a)). While this is promissing and would justify calculations at higher k-point density, it is clear that other surface motifs need to be explored, and this is

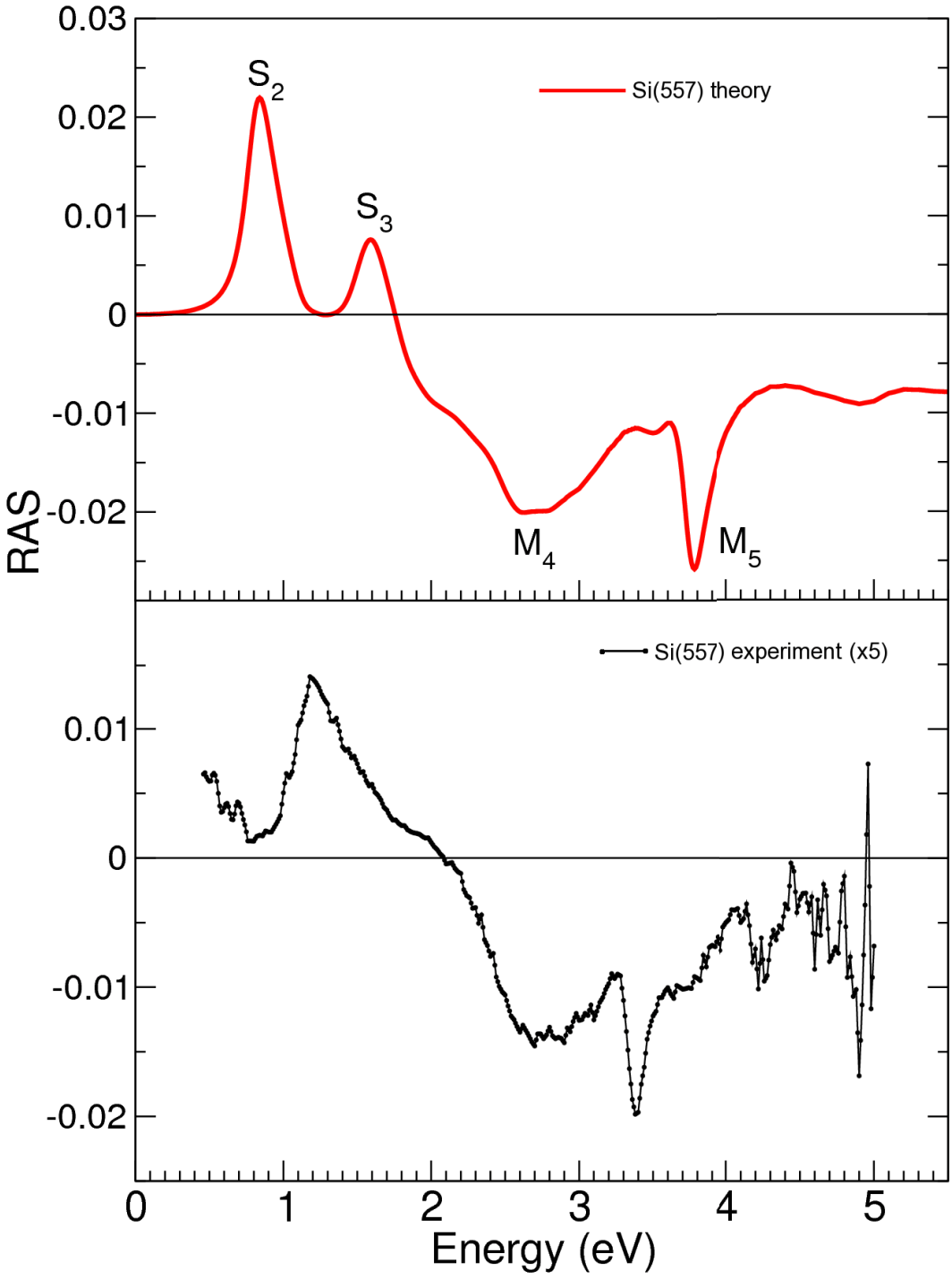

Figure 6.2: A comparison between the experimental RAS spectra and the theoretical response, calculated using a *ab initio* DFT-LDA approach for bulk truncated and relaxed Si(557).

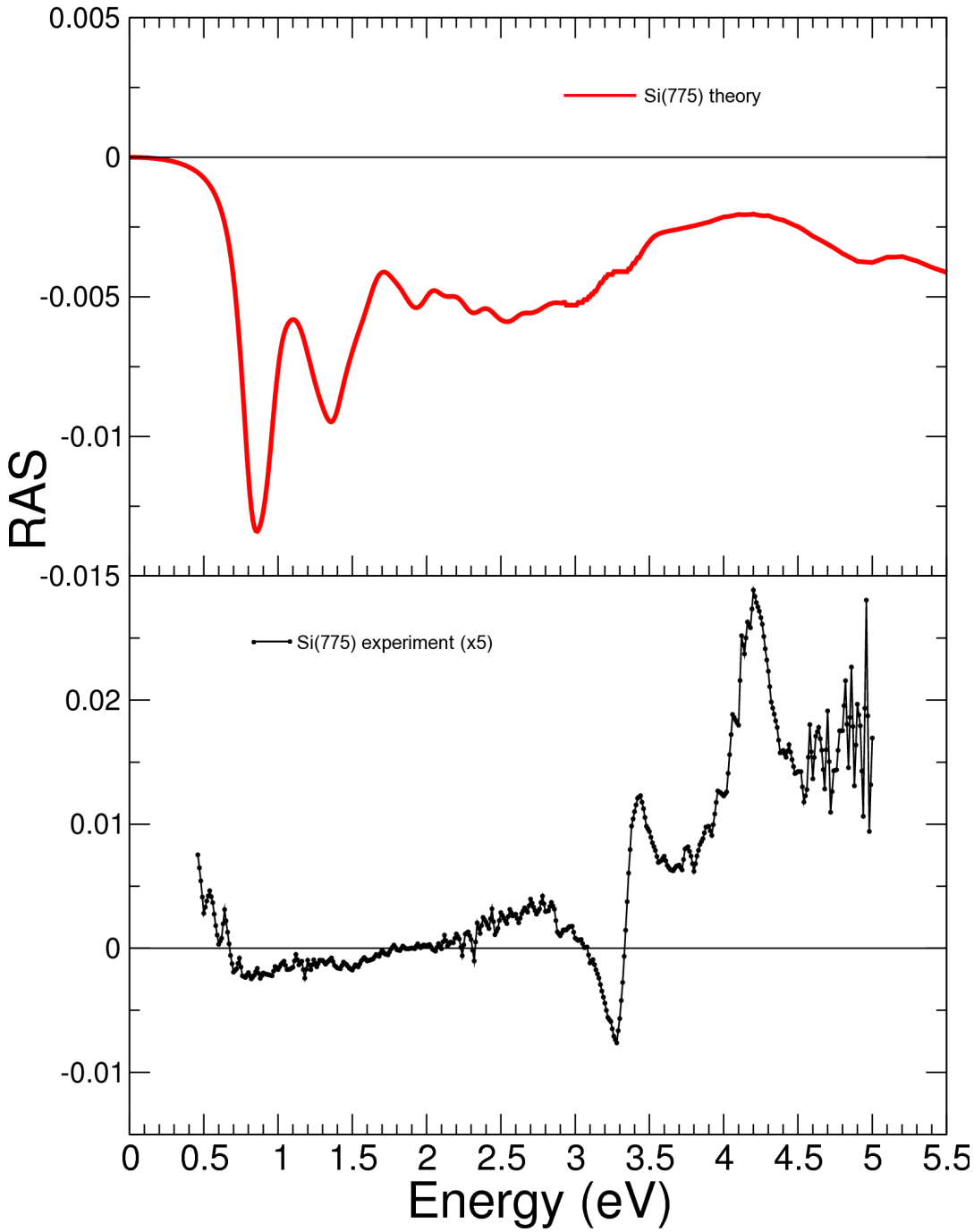

Figure 6.3: A comparison between the experimental RAS spectra and the theoretical response, calculated using a *ab initio* DFT-LDA approach for bulk truncated and relaxed Si(775).

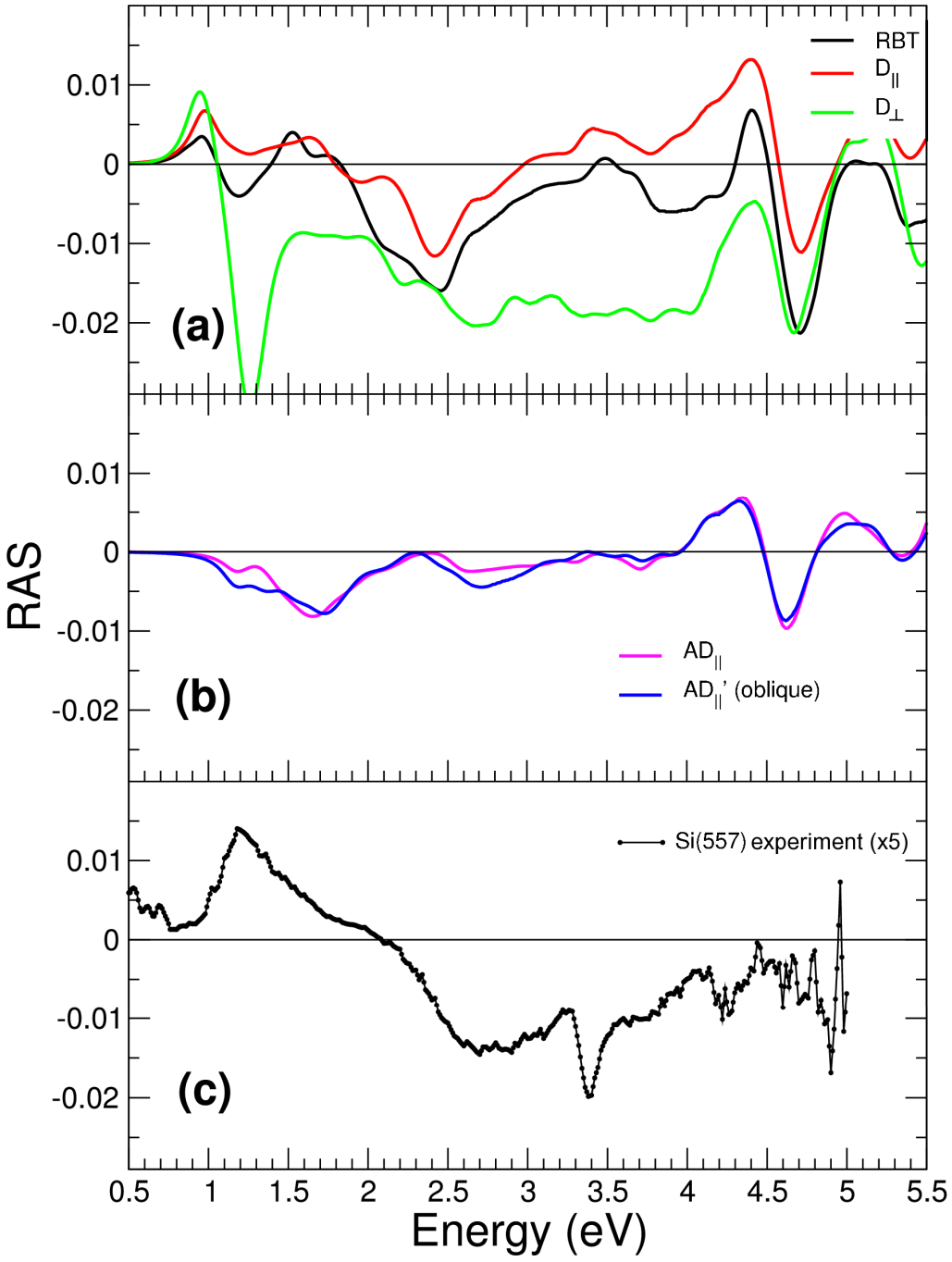

Figure 6.4: A comparison of theory, for various reconstructed Si(112) surfaces, with the experimental Si(557) spectrum.

on-going.

6.4 Conclusions

Given the difficulty of *ab initio* optical response calculations, this initial work has been quite successful in reproducing the RAS spectra from Si(557). A bulk terminated and relaxed Si(557) surface provided the best fit. The structure at 1.2 eV may come from either a Pandey-type chain or a dangling bond state at the step edge. As Pandey-type chain structures have produced RAS signatures at significantly lower energy than the structure recorded here, the dangling bond state at the step edge is the more likely candidate. There is good experimental evidence for the triple step structure, however, even though calculations of various Si(112) structures appear less promising more surface motifs need to be explored and a large unit cell calculation of the complete surface with triple height steps and total energy minimisation appears necessary. This is an essential first step in modelling the other surfaces discussed in chapter 5. Successful theoretical modelling of the Si(557 and Si(775) optical response will provide the RAS spectra from Si(557)-Au, Si(775)-Au, adatom free Si(111)-5×2-Au and adatom decorated Si(111)-5×2-Au.

7 Metallic nanoislands

7.1 Growth of nanowires by anisotropic diffusion

When metals are deposited on some well ordered semiconductor surfaces there can be a large anisotropy in the metals diffusion barrier in orthogonal directions. When a metal is deposited on such surfaces it can form elongated islands with length to width ratio > 25. These elongated islands show very interesting optical and electrical properties. They potentially have some interesting uses in fields such as optical computing and communications. Some materials grown by this method have shown anisotropies in reflectance of >20%, which means the material will be a different colour depending on the polarisation of light that is used to view it.

7.1.1 Silver islands

There are several examples of Ag forming anisotropic islands on Si and other surfaces. When Ag is deposited on vicinal Si(100) it can form ~ 5 μm long and ~ 50 nm wide islands [214]. When Ag is deposited on Si(111)-3×1-Ag it will also form highly anisotropic islands which show a strong reflectance anisotropy [7]. RAS spectra from these ellipsoidal islands show a large minimum at about 1 eV depending on the off-cut of the Si and the amount of Ag deposited (figure 7.1). When these structures are capped the minimum shifts to the IR and increases in intensity (figure 7.2). These results will be discussed further in section 7.4.2, with regard to the modelling of the optical response from metallic islands.

7.1.2 Lead islands on Si(557)-Au and Si(335)-Au

Lead was initially found to form anisotropic structures on Si(335)-Au by Jalochowski *et al* in 1998 [215]. They found a polarised reflectance difference that increased up to about 10 ML of Pb, with a minimum around 0.9 eV and a maximum below 0.5 eV. This work was extended in 2002 by depositing at low temperatures (100 K). They again found a large optical anisotropy with a minimum around 0.9 eV and a maximum at 0.5 eV [216]. They also investigated the behavior at higher temperatures and found the optimum optical anisotropy when the samples were held around 260 K during Pb deposition [39, 217]. STM images of the islands that were being formed showed that they were ∼12 nm high, 60 nm wide and could be up to 1500 nm long. Other Si off-cuts were also found to produce elongated islands of Pb, these include Si(100)-Au, Si(110)-Au and Si(557)-Au [39]. Si(557)-Au showed

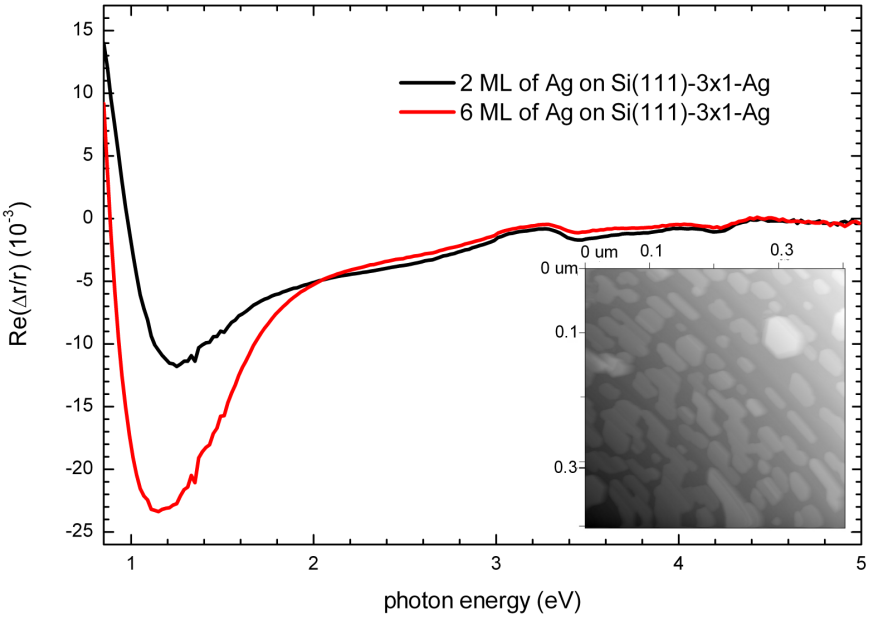

Figure 7.1: RAS spectra from Ag ellipsoids grown on Si(111)-3×1-Ag (recorded by Dr Julie Jacob in this research group [7]). The inset shows an AFM image of the ellipsoids. The AFM image was recorded by Dr Sandhya Chandola in the Technische Universität Berlin.

the islands with the greatest ratio of length/diameter. RAS measurements of these systems have not been published.

The growth process of the Pb islands can be divided into two phases. Up to an average coverage of ∼1.5 ML of Pb, a wetting layer is formed, then a nucleation of islands. This is followed by anisotropic growth around room temperature as Pb cannot diffuse up and down steps so the nucleated islands grow in length rather than width. Growth of the elongated islands continues up to 12 ML, with the width remaining fairly constant at around 60 nm [39]. The whole process strongly depends on the mobility of the Pb atoms and thus the temperature. In the range between 260 and 280 K the islands with the largest aspect ratios length/diameter are produced [39]. Under ideal conditions these wires can grow to several micrometers while their width remains constant at 60 nm (figure 7.3). When the substrate is warmer than this Pb can diffuse across the steps and islands will grow in width as well as length.

7.2 Modeling the optical response from metallic nanowires

Modeling the RAS signal from anisotropic islands on Si has been attempted using several different anisotropic models. These models are discussed in the next few

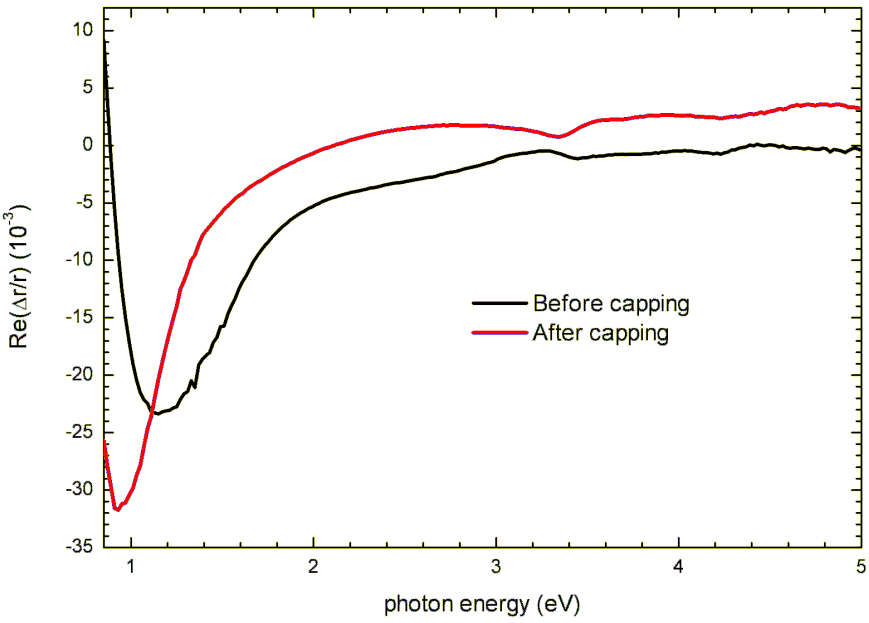

Figure 7.2: RAS spectra from Ag ellipsoids grown on Si(111)-3×1-Ag before and after capping (after [7]).

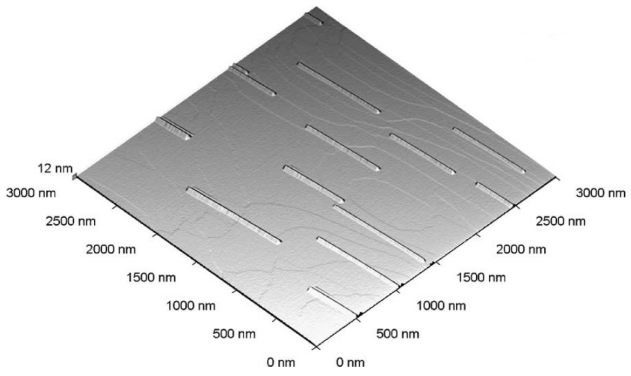

Figure 7.3: STM image of Pb nanowires grown on Si(335)-Au at 260 K (after [216]).

sections. The RAS signal they predict is shown and the effect of changing several parameters is explored. Limitations of each model will also be discussed.

7.2.1 Anisotropic Drude free electron model

The Drude free electron model is a simple model that predicts the optical, electrical and thermal properties of metals. It assumes that electrons are completely detached from the ion core of the metal and have negligible interactions with each other. Despite its simplicity it is reasonably successful and quite widely used. The dielectric function of a metal can be calculated using the Drude model if the plasma frequency (ω_p) and scattering rate (ω_τ) are known:

$$\epsilon(\omega) = \epsilon_b - \frac{\omega_p^2}{\omega^2 + i\omega\omega_\tau} \tag{7.1}$$

where ϵ_b is the static dielectric function of the metal, normally set to 1 for a good free electron metal, and $\omega_p = N_e e^2/m_e\epsilon_0$, where N_e is the free electron density.

The plasma frequency of a real metal does not change much as the size of the metal cluster is reduced [218]. However, the scattering rate of the electrons in the metal can have significant size dependence. In particular, as the metal clusters are reduced in size below the bulk scattering length, the scattering rate increases because electrons can scatter off the surface of the cluster. The size dependent scattering rate can be given as:

$$\omega_\tau = \omega_{\tau,b} + C\frac{V_f}{R} \tag{7.2}$$

where $\omega_{\tau,b}$ represents the bulk scattering rate, V_f is the Fermi velocity of an electron in the metal (it is assumed not to have a size dependence), R is the radius of the cluster and C is a constant ~ 1 [219–221]. The value of C depends on the details of the scattering at the metal surface and for this work was always set to 1 [222, 223]. The RAS response from anisotropic islands can be modelled by assuming different scattering rates in the x and y directions in the surface plane [10]. Equation 7.2 is simply extended by replacing the radius of the cluster by half the length and width of the anisotropic island, and then the RAS response calculated with equation 4.20.

Figure 7.4 shows the expected RAS signal from different metal nanoislands on Si: the nanoislands are 500 nm long, 10 nm wide and 1 nm high. Table 7.1 gives the plasma frequency, bulk scattering rate and Fermi velocity for the metals considered. The spectra have a broad minimum below 1 eV for each metal that is broadest for metals with the highest bulk scattering rate. The spectra also show a large peak towards 0 eV, and again this peak is broader for metals with a higher bulk scattering rate. The minimum position is shifted slightly for each metal and is found to depend

Table 7.1: The plasma frequencies, bulk scattering rates and Fermi velocities for the relevant metals (from [224])

	ω_p (eV)	$\omega_{\tau,b}$ (eV)	V_f (ms^{-1})
Au	9.0	0.080	1.4×10^6
Pb	7.7	0.180	1.83×10^6
Ag	9.0	0.018	1.39×10^6
Cu	7.9	0.034	1.57×10^6
Al	14.8	0.080	2.03×10^6

mainly on the scattering rate with larger scattering rates shifting the minimum to higher energies.

Figure 7.5 shows the dependence of the predicted RAS spectra on the island width. The width was varied from 1 nm to 500 nm, while the length was held constant at 1000 nm. The RAS spectra have been normalised so that comparisons can be easily made between different island widths. As the island width increases the minimum position shifts to lower energy and becomes significantly sharper. This is exactly what one might expect as the small islands will have a very large scattering rate in the direction perpendicular to the wires, while the wide islands will have a similar scattering rate to the bulk material.

There are several limitations with the anisotropic Drude free electron model. The main limitation is that a capping layer will have no effect on the RAS structure. The model is also unrealistic for most metallic systems as it completely neglects Mie resonance type effects such as increased dipole strength at points of high curvature [225].

7.2.2 Anisotropic polarisability

The anisotropic polarisability model was developed to remove some of the limitations of the Drude free electron model. By representing the anisotropic layer with a Bruggerman mixing formula the dielectric function of the capping material has an effect on the peak positions of the predicted RAS spectrum and, by using depolarising factors as detailed in [226, 227], the effects of the curvature of the islands are accounted for. This model however assumes that there is no interaction between islands and there is no image charge formed in the substrate. The discussion below is limited to the dipolar case: A detailed discussion of quadrupolar and higher order terms is given in the book by D. Bedeaux [227]. The equation for the polarisability

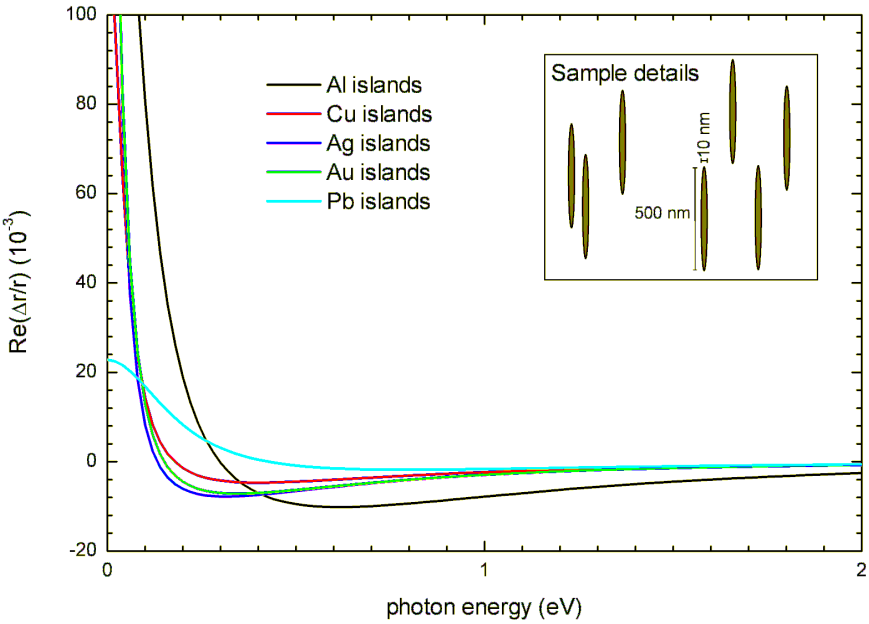

Figure 7.4: Calculated RAS spectra for metallic nanowires that are 500 nm long and 10 nm wide, for various metals.

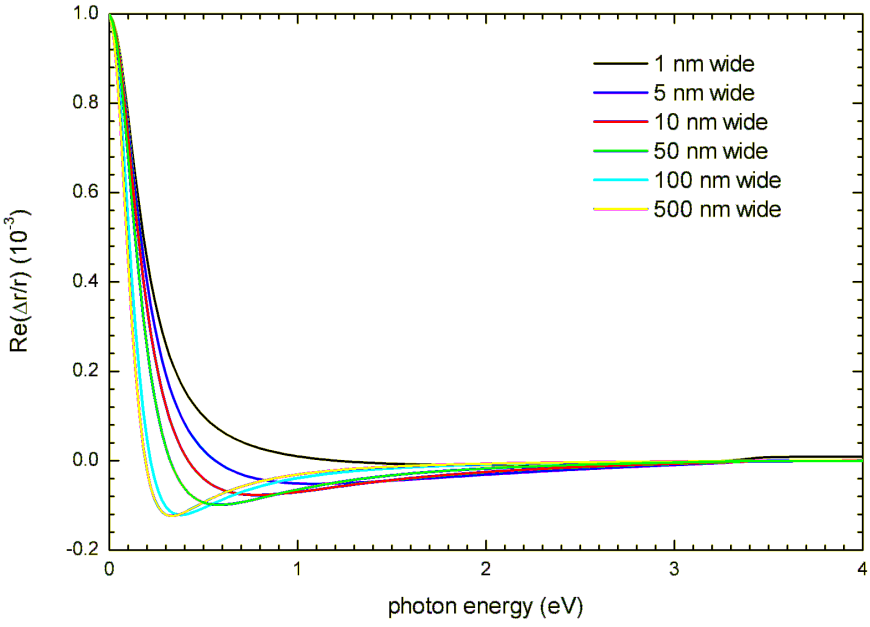

Figure 7.5: Calculated RAS structure for Pb nanowires that are 1000 nm long and have a width from 1 nm to 500 nm.

of the islands in each direction is:

$$\alpha_i = \frac{4\pi xyz}{3}\left(\frac{\epsilon - \epsilon_a}{\epsilon_a + N_i(\epsilon - \epsilon_a)F_i}\right) \tag{7.3}$$

where ϵ_a is the dielectric function of the embedding medium, ϵ is the dielectric function of the metal, N_i is the depolarisation factor (equation 7.4) in the direction i and F_i is a correction factor arising from the modified long wavelength approximation (MLWA) (equation 7.5) [228].

$$N_x = \frac{xyz}{2}\int_0^\infty \frac{dq}{(x^2+q)\sqrt{(x^2+q)(y^2+q)(z^2+q)}} \tag{7.4}$$

where x, y and z are the semi-axis of the islands in each direction. $N_x + N_y + N_z = 1$, and there are several simplifications that can be used for regular shaped islands, discussed in the book by A. Sihvola [229]. The *quasi*-static approximation ($F_i = 1$) can be used where island dimensions are much less than λ, but for long islands MLWA should be used:

$$F_x = 1 - (kx)^2 - \frac{2}{3}i(kx)^3 \tag{7.5}$$

where k is the wave vector of the incidence light and x is the semi-axis in the direction of interest. The second term arises from dynamic depolarisation effects and the third term from radiative damping [228].

To convert the individual island polarisability α_x and α_y into a predicted RAS signal they must be scaled using $\gamma_x = \varphi\alpha_x$, where φ is the volume fraction. The ellipsometry equations for a optically dense polarisable material on a less dense substrate are then used [41]:

$$r_{s,x} = \frac{\cos\theta - n_s\cos\theta' + ik\gamma_x}{\cos\theta + n_s\cos\theta' - ik\gamma_x} \tag{7.6}$$

and

$$r_{p,x} = \frac{(n_s\cos\theta - \cos\theta')\left(1 - \frac{k^2}{4}\gamma_x\gamma_z\sin^2\theta\right) - ik\gamma_x\cos\theta\cos\theta' + ikn_s\gamma_z\sin^2\theta}{(n_s\cos\theta + \cos\theta')\left(1 - \frac{k^2}{4}\gamma_x\gamma_z\sin^2\theta\right) - ik\gamma_x\cos\theta\cos\theta' - ikn_s\gamma_z\sin^2\theta} \tag{7.7}$$

where n_s is the refractive index of the substrate, k is the wave vector of the incidence light ($2\pi/\lambda$), θ is the angle of incidence and θ' is the angle of refraction. For normal incidence $r_{p,x} = r_{s,y}$ and $r_{s,x} = r_{p,y}$. The RAS response can now simply be calculated from:

$$RAS = \frac{2(r_{p,x} - r_{p,y})}{r_{p,x} + r_{p,y}} = \frac{2(r_{s,x} - r_{s,y})}{r_{s,x} + r_{s,y}} \tag{7.8}$$

The metal dielectric function for these islands is taken from the modified Drude model discussed in section 7.2.1, which includes anisotropic scattering rates.

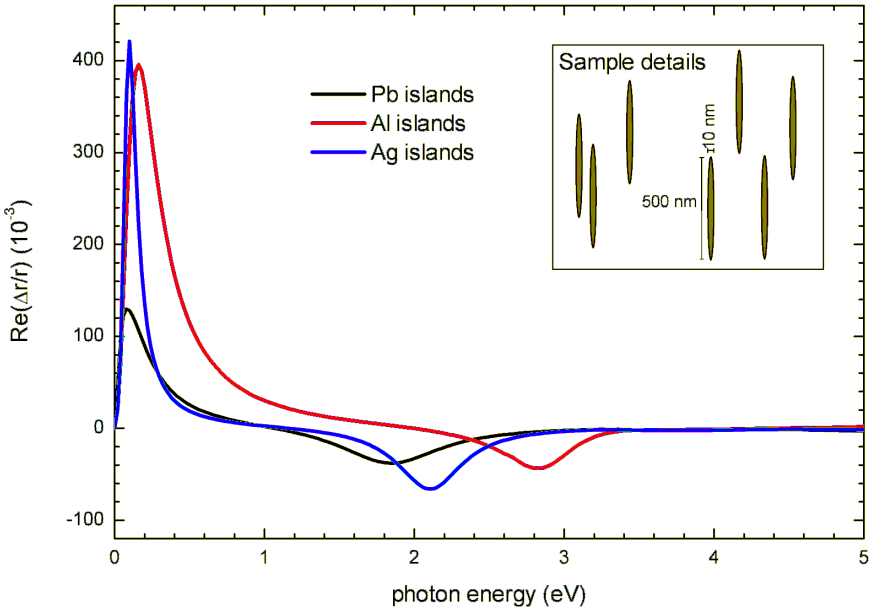

Figure 7.6: Calculated RAS spectra for metallic ellipsoids that are 500 nm long, 10 nm wide and 5 nm high for various metals. The embedding medium was taken as a linear combination of 50% Si and 50% vacuum.

RAS spectra were calculated for several island shapes, capping materials, and metals using an Excel worksheet (appendix C). Figure 7.6 shows islands of Al, Ag and Pb. Two large features are seen, one related to a plasmon dipole oscillation in the length of the islands (the large maximum in the IR) and one related to a plasmon dipole oscillation in the width (the smaller minimum). The embedding dielectric function was taken to be a linear combination of 50% Si and 50% vacuum [226], as approximately half the island will be in contact with the Si substrate. The main features to note are that, as the plasma frequency of the metal increases, the features shift to higher energy and that, as the scattering rate increases, the features broaden (table 7.1).

Figure 7.7 shows the effect of island width on the predicted RAS spectra. Spectra are calculated for islands with widths from 5 nm to 100 nm. The length and height of the islands was kept constant at 500 nm and 5 nm, respectively. As the width is increased the minimum shifts to the IR and sharpens. The shift arises from the change in the depolarisation factor (equation 7.4), and the sharpening is a direct effect of the decrease in the scattering rate as the width is increased. There is a small shift to the UV in the maximum but this is mainly due to the subtraction in the RAS equations.

Figure 7.8 shows the effect of changing the island length on the predicted RAS

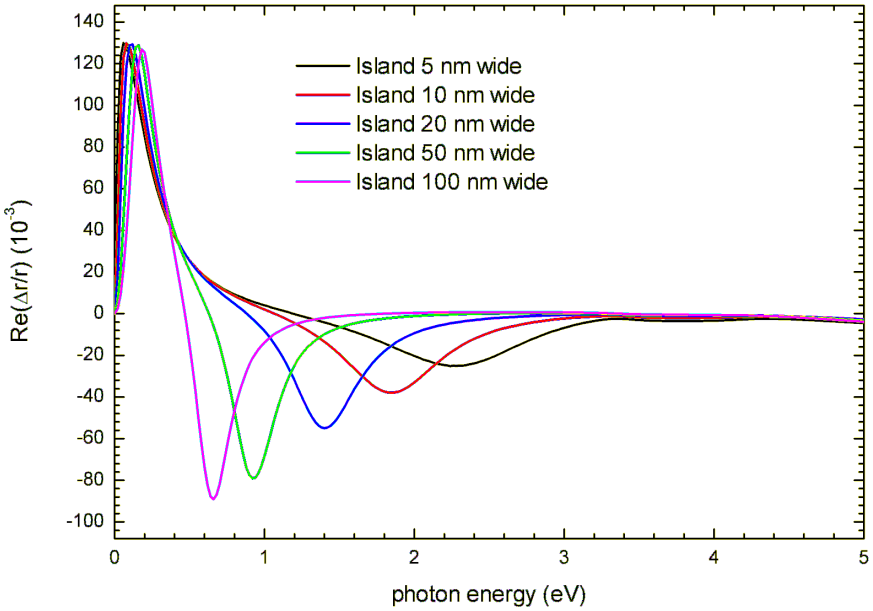

Figure 7.7: Calculated RAS spectra for metallic Pb ellipsoids that are 500 nm long, 5 nm high and have widths varying from 5 nm to 100 nm. The islands are embedded in a dielectric medium that is a linear combination of 50% Si and 50% vacuum.

spectra. Islands with a length of 75 nm, 100 nm, 200 nm and 500 nm were modelled while the width and height were held constant at 50 nm and 5 nm respectfully. The maximum is seen to shift to the IR as the islands are made longer. The minimum also shifts slightly to the UV as the islands get longer but as discussed above this is mainly an affect of the subtraction in the RAS calculation. There is also a slight sharpening of the maximum as the length of the islands increases, due to the decrease in scattering rate.

The final experiment with this model was the effect of capping the islands with different materials. To understand this three RAS spectra were generated with different embedding medium dielectric functions, 100% vacuum, 50% vacuum-50% Si and 50% a-Si-50% Si. Figure 7.9 shows the effect for Pb islands with a length of 500 nm, a width of 50 nm and a height of 5 nm. As the optical density of the capping layer increases, both features shift to the IR and reduce in intensity.

This model addresses many of the issues with the simple Drude model. It allows for an embedding medium and accounts for the island shape. It also has several limitations: it does not account for an inter-island dipole interaction, image charge formation, or quadrupolar interactions. The islands discussed below show no sign of the quadrupolar structure observed in the optical response of small potassium particles grown on oxidised Si [230]. Inter-island dipole interactions could be significant

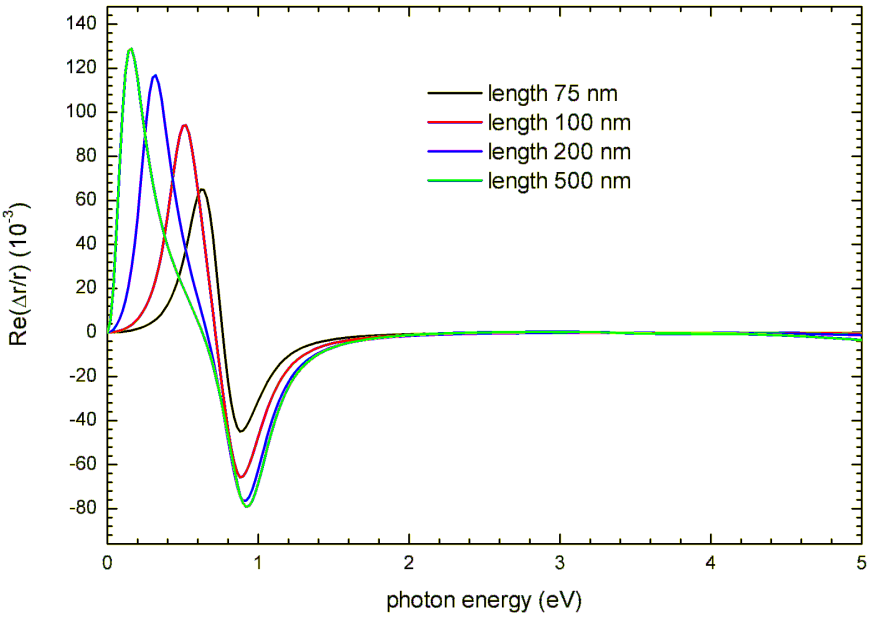

Figure 7.8: Calculated RAS spectra for metallic Pb ellipsoids that are 5 nm high and 50 nm wide. The lengths were varied from 75 nm to 500 nm. The islands are embedded in a dielectric medium that is a linear combination of 50% Si and 50% vacuum.

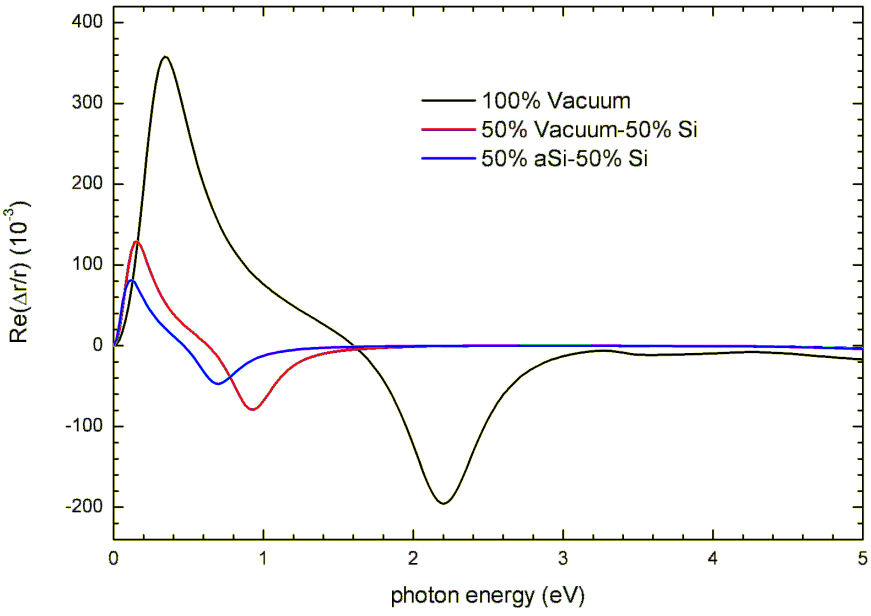

Figure 7.9: Calculated RAS spectra for Pb ellipsoids that are 500 nm long, 5 nm high and 50 nm wide for various embedding media.

at high island densities, however, and the image charge formed in the uncapped system could shift or broaden the features seen. The image charge effect is expected to be important when studying the difference between capped and uncapped systems. For an uncapped system, the image charge will be present but when the system is capped with a-Si, the image charge will be largely removed (a-Si and Si have a very similar dielectric function in the region of the features). Both of these effects can in some way be dealt with by modifying the depolarisation factor N_i.

7.2.3 Image charge model

A simple model has been developed that helps to account for image charge effects. There are two modifications that must be made to the anisotropic polarisability model discussed in the previous section. The depolarisation factor N_i is reformulated and the optical response from the metal island dipole must be coupled to the optical response from the image dipole [231, 232]. The image charge strength is given by:

$$S = \frac{\epsilon_s - \epsilon_a}{\epsilon_s + \epsilon_a} \tag{7.9}$$

where ϵ_s is the dielectric function of the surface and, as above, ϵ_a is the dielectric function of the embedding medium. The depolarisation factor can then be modified to include an image charge effect using:

$$N_i^{'} = N_i \left(1 - \left(\frac{d}{2R_z} \right)^3 S \right) \tag{7.10}$$

where d is the distance between the center of the island and the surface and R_z is the radius of the island in the z (surface normal) direction. For the calculations discussed here $d = R_z$, as the theoretical surface and experimental surface are assumed to coincide.

The polarisability is now modified to include the two coupled dipoles, the dipole in the metal and the image dipole.

$$\alpha_i = \frac{4\pi xyz}{3} \left(\frac{\epsilon - \epsilon_a}{\epsilon_a + N_i^{'}(\epsilon - \epsilon_a)F_i} \frac{2\epsilon_s}{\epsilon_s + \epsilon_a} \right) \tag{7.11}$$

By using this equation to predict the RAS spectra from metallic islands it is possible to study the effect of the image charge for both uncapped islands (figure 7.10) and capped islands (figure 7.11). The Pb islands were 500 nm long, 100 nm wide and 10 nm high. For the uncapped case the image charge has a significant effect, shifting the signal to the UV and increasing the intensity of the peak. It does not seem to broaden the peak. For the capped case there is almost no effect from

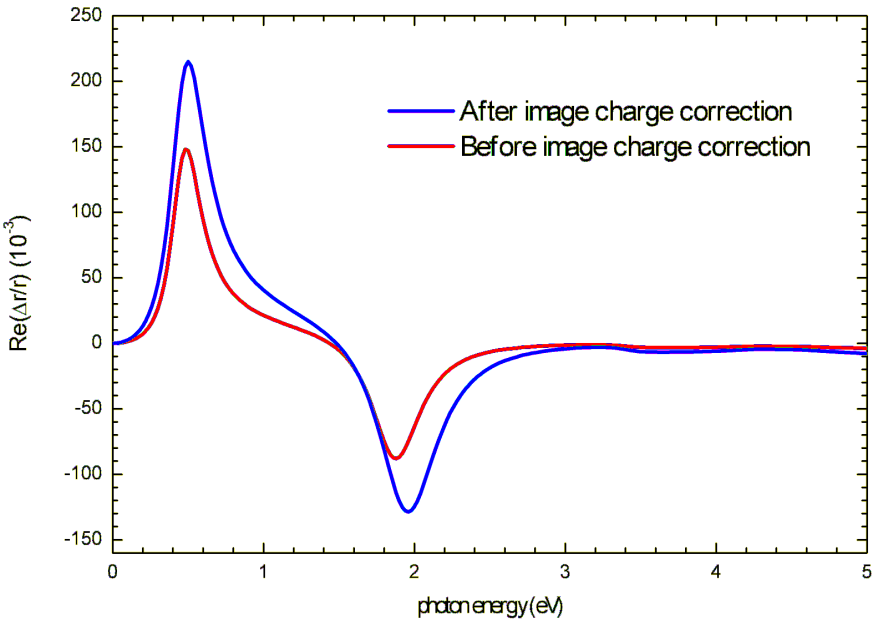

Figure 7.10: Calculated RAS spectra for uncapped Pb ellipsoids that are 500 nm long, 100 nm wide and 10 nm high, before and after applying the image charge correction.

the image charge. This is easily explained because the dielectric function of Si and a-Si are so similar that $S \approx 1$. There is a very small difference in the peak in the IR with the image charge slightly increasing the intensity of the maximum.

7.2.4 Anisotropic dipole-dipole interactions

The dipole-dipole interaction between islands can be included in the model by modifying the depolarisation constants [233]. However, this cannot be done for ellipsoidal particles where the interaction between particles in the x direction will be significantly stronger than interactions in the y direction due to the much greater radius of curvature at the ends of the ellipsoids.

For spherical particles the depolarisation constant can be rewritten as $N_i^{'} = N_i + \beta_i$ where β_x depends on the distance between islands in the x direction and β_y depends on the distance between islands in the y direction. Yamaguchi *et al* [233] calculated β_i as:

$$\beta_i = -\frac{C}{a_i} \tag{7.12}$$

where C is a constant depending on the material, embedding medium, lattice shape and thickness of the islands and, a_i is the lattice constant (island separation) in the i direction. For the calculation here C was fixed at 0.5 nm.

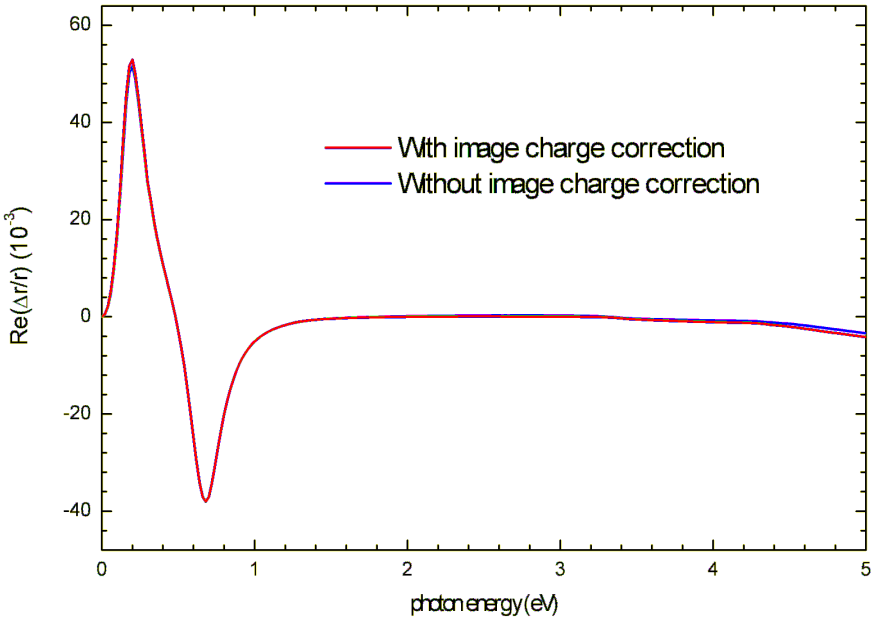

Figure 7.11: Calculated RAS spectra for Pb ellipsoids that are 500 nm long, 100 nm wide and 10 nm high, capped by a-Si, before and after applying the image charge correction.

Figure 7.12 shows the effect of changing the a_y value from 20 nm to 1000 nm while the a_x is held constant at 10 nm (islands just touching but no electrical contact). The island dimensions are 10 nm in x and y and 1 nm in z. The Pb islands capped by 50% Si and 50% vacuum. No image charge contribution was included. As the distance between islands is increased the effect of the dipole interaction is reduced until at $\sim$ 100 nm no significant dipolar-dipolar interaction remains in the a_y direction. The effect of the interaction is to create a large structure with a maximum at 0.15 eV and a minimum that shifts from 0.68 eV to 0.76 eV as the distance between the islands is increased.

Figure 7.13 shows the effect of changing the a_x value from 10 nm to 200 nm while a_y is held constant at 1000 nm. The island dimensions and dielectric functions are the same as in figure 7.12. The RAS spectrum is found to decrease significantly as the distance between islands is reduced and the lattice becomes more isotropic. The minimum position is found to shift from 0.76 eV to 0.88 eV while the maximum signal shifts from 0.18 eV to 0.3 eV.

This simplistic treatment of dipole-dipole interactions of isotropic islands gives a qualitative idea of the effect they will have on the RAS spectra. The effect is expected to be seen only when the islands are significantly closer than 100 nm. If the embedding dielectric is also included the value of C would be expected to reduce

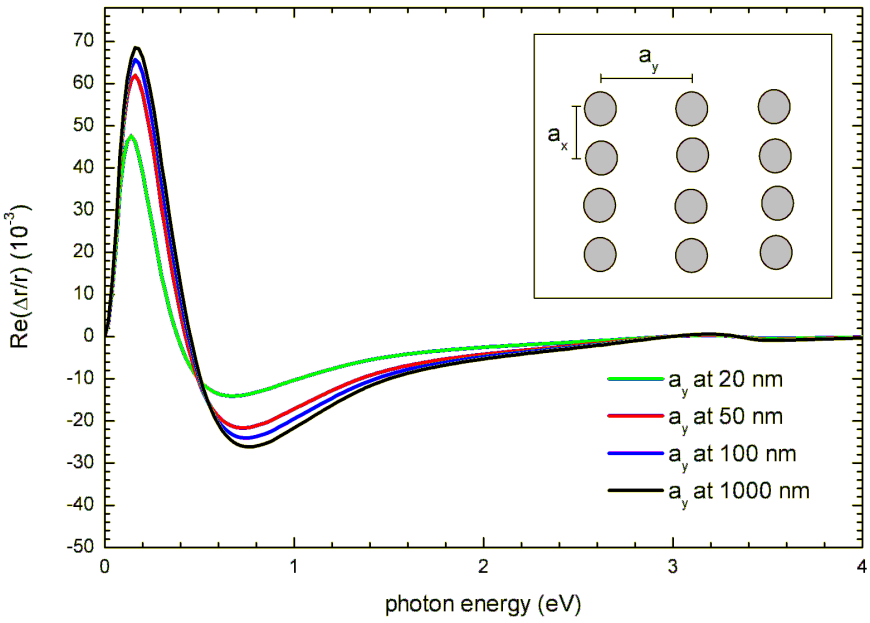

Figure 7.12: Calculated RAS spectra from spherical Pb islands in a square lattice separated by a lattice constant of 10 nm in the x direction, and a lattice constant varying from 20 nm to 1000 nm in the y direction.

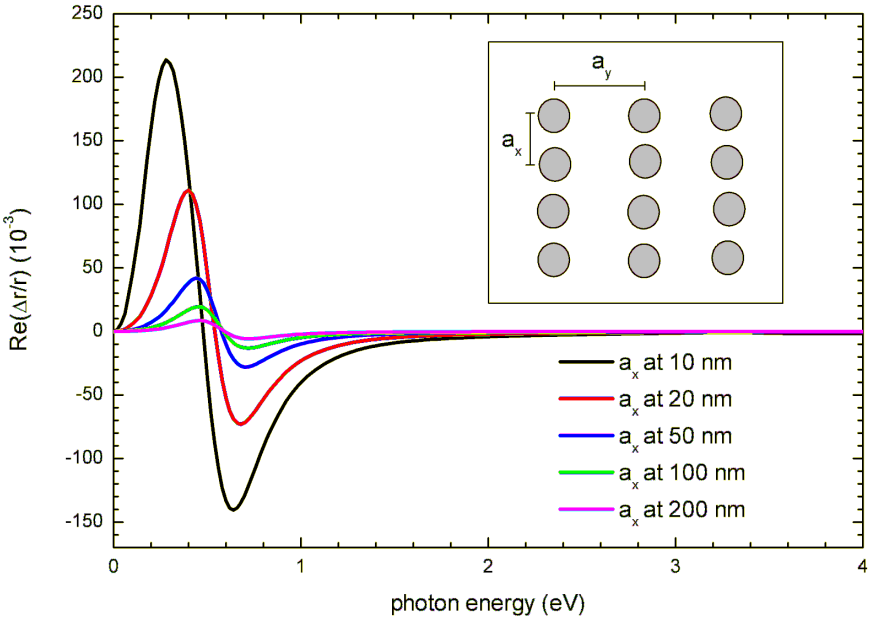

Figure 7.13: Calculated RAS spectra from spherical Pb islands in a square lattice separated by a lattice constant of 1000 nm in the y direction, and a lattice constant varying from 10 nm to 200 nm in the x direction.

[222, 223, 232], meaning the islands would have to be even closer together to interact strongly. The Pb islands that were created in this work are anisotropic and, as such, modelling the true dipole-dipole interaction is significantly more complicated than discussed here. For these reasons the dipole-dipole interaction was not included while modelling the RAS signal from the Pb islands. For the anisotropic Ag islands created by Fleischer *et al* [7] the dipole interaction could be important due to the small distance between islands.

7.2.5 Nanoantenna model

Elongated metallic islands can act as nanoantennae with strong resonances in the IR. IR antenna resonances have been observed for single gold elongated nanoislands [234]. In the gold antennae case it turned out that their resonance curves deviate from that of ideal antennae in vacuum because of the effect of the substrate dielectric function. However, the substrate effect can be taken into account by calculating an effective refractive index, a linear combination of the substrate dielectric function and surrounding medium dielectric function [226]. The nanoantenna model can be used to give a first approximation of the length of the islands if the width, metal plasma frequency ω_p and surrounding dielectric function are known.

$$2L = \lambda_{eff} = 2\pi R \left(13.74 - \frac{0.12(1 + 141.04\epsilon_s)}{\epsilon_s} - \frac{2}{\pi} + \frac{\lambda}{\lambda_p}\frac{0.12}{\epsilon_s}\sqrt{1 + 141.04\epsilon_s} \right) \tag{7.13}$$

where λ_p is the wavelength of the plasma resonance in the metal, ϵ_s is the embedding medium dielectric function, R is the radius of the island, and λ is the wavelength of the maximum. The numerical values in this equation were calculated by Novotny [235]. Since the islands did not have a circular cross section the radius was taken as:

$$R = \sqrt{\frac{WH}{\pi}} \tag{7.14}$$

where W is the width and H is the height of the metallic islands. This could be a potential source of inaccuracy in calculations involving the antenna model.

In section 7.4.1 equation 7.13 is used to give an estimate of the length of the Pb islands that were created on Si(557)-Au. These equations, however, do not predict anything about the line shape of the resonance nor do they predict the minimum that was routinely seen around 1 eV. It does, however, predict a shift in the peak position as a material is capped. This shift is smaller than the shift that was observed during capping of the Pb nanoislands.

7.3 RAS from Pb islands grown on Si(557)-Au

Lead islands were grown on Si(557)-Au. During deposition the sample was kept at room temperature. Although this meant that optimum isolated nanowires were not produced, elongated islands with a large RAS signal were produced. RAS spectra were recorded at various stages during deposition to gauge when a maximum optical anisotropy had been achieved. Some samples were removed from the UHV chamber before capping and transferred under low vacuum ($\sim 10^{-2}$ mbar) to a SEM. Images were then taken of the islands. These samples were also taken to the DFG laser for measurement using rotating sample RAS. It was found that after about 1 week in ambient the RAS signal was completely removed. Other samples were capped with 4.5 nm of a-Si and then removed from the chamber. They were also measured using rotating sample RAS. Capped samples were found to retain their RAS signal for several weeks in ambient conditions.

7.3.1 Uncapped islands

The RAS signal monitored during the growth of the Pb islands is shown in figure 7.14. RAS spectra were recorded every 0.5 ML from 1.5 ML until 6 ML of Pb had been deposited. Initially the Pb quenches the Si(557)-Au signal, supporting the idea that the first ML forms a wetting layer on the surface which is then followed by anisotropic island growth [40, 236, 237]. The minimum that is formed slowly grows in amplitude and shifts slightly to the IR. The shift can be explained by considering that islands will get slightly wider as Pb is deposited, as shown in figure 7.7. The increase in signal can be explained as an increase in density of Pb islands on the surface. Unfortunately, with the current UHV chamber it is impossible to monitor the IR maximum below 0.5 eV, which should give information about how the length of the islands is changing with Pb coverage (figure 7.8). This limitation is mainly due to absorption in the low strain fused silica window. Above 6 ML of Pb only small changes in the RAS signal were seen in the spectral range from 0.85 eV to 4 eV. However, as Klevenz *et al* have reported for Pb islands on Si(335)-Au, the maximum below 0.5 eV is expected to keep growing until about 15 ML [40].

The RAS signal from the uncapped islands formed after 8 ML of Pb had been deposited is shown in figure 7.15. It shows two large structures; a minimum at 1.15 eV and a maximum at 0.47 eV. The laser RAS, while quite noisy, confirms that the presence of the maximum at 0.47 eV. The maximum is approximately 7 times larger than the minimum and is significantly narrower. The anisotropy due to Si(557)-Au reconstruction has been completely removed by the Pb, but the Si bulk critical point

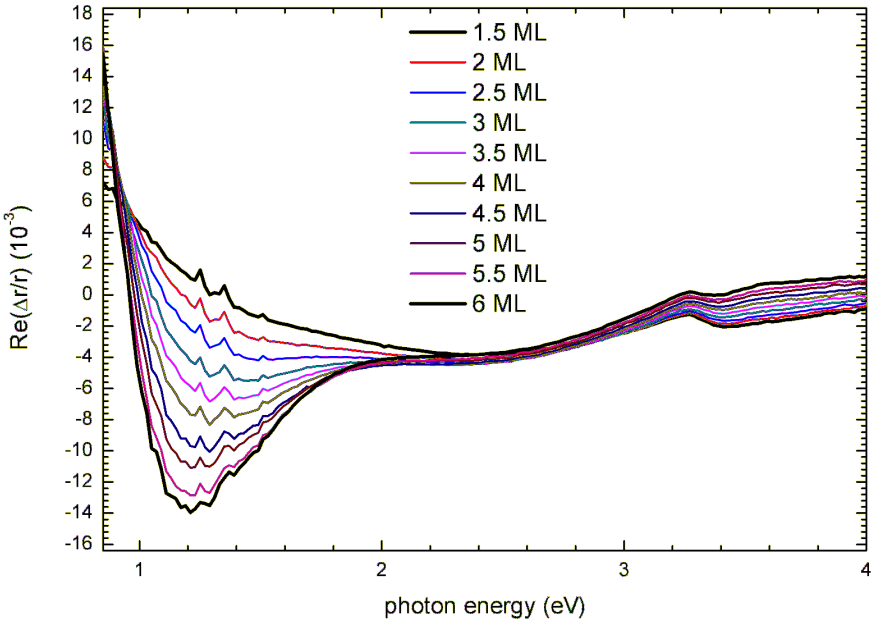

Figure 7.14: RAS signal monitored during the growth of Pb islands.

at 3.4 eV is still visible.

Klevenz *et al* [40] and Chung *et al* [237] have both performed polarisation dependent Fourier transform IR (FTIR) absorption spectroscopy. Their results can be converted into a RAS signal (figure 7.16), and have been plotted on the same scale used in this work to allow comparison. They observe a similar maximum to those presented here, but shifted to the IR. The shift could be explained by the larger quantity of Pb that they deposited, which would mean that, on average, their islands are larger than those presented here. This is confirmed by comparing their AFM images to the SEM images presented later (figures 7.19 and 7.20). The difference in the shape of the maxima indicates that RAS could be a useful *in situ* probe of anisotropic nanoisland shape, if a suitable model can be developed.

7.3.2 Capped islands

Islands were capped by depositing 4.5 nm of a-Si on top of them. RAS spectra were recorded after capping to establish if the capping procedure had altered the island structure. The RAS spectrum after capping is shown in figure 7.17. It shows a similar structure to the uncapped islands, with both features shifted slightly to the IR. The minimum is now at 0.90 eV and the maximum is at 0.39 eV. The minimum has increased in size significantly.

There are several possible scenarios that could happen when the islands are

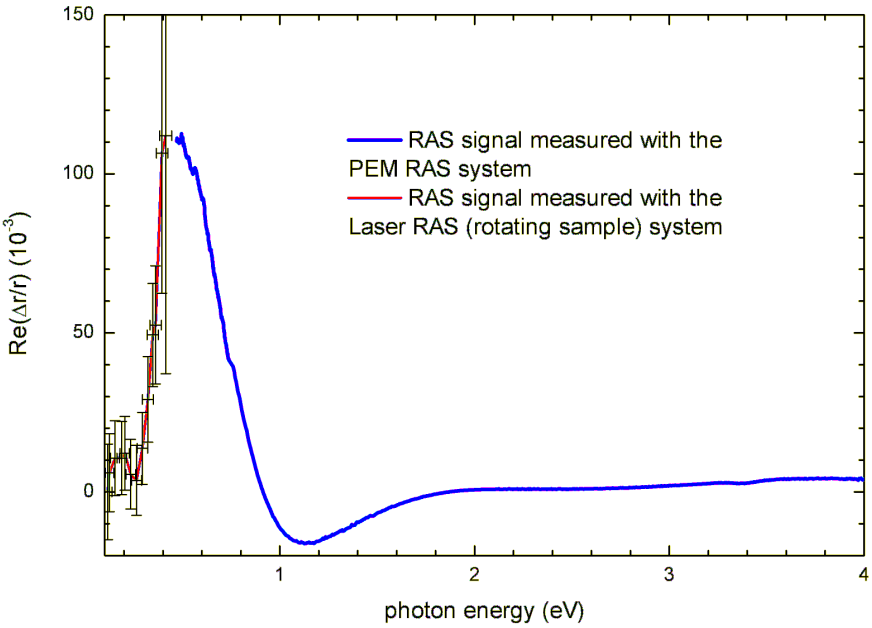

Figure 7.15: RAS signal from uncapped Pb islands after 8 ML of Pb had been deposited on Si(557)-Au. The PEM RAS signal was recorded through a low strain UHV window and the laser RAS signal was recorded soon after the sample was removed from the chamber, before significant oxidation could occur.

capped. The a-Si could alloy with the Pb islands, the Pb could defuse through the a-Si or the islands could Ostwald ripen due to the rise in temperature of the sample when it is exposed to the Si flux. Alloying and diffusion does not occur during island growth at room temperature, and is unlikely to occur during capping. However, the island shape could alter and RAS could probe this. The optical response of the islands could be modelled before and after capping, the only change being in the embedding medium dielectric function.

The success of capping was judged by how long the sample could be kept at ambient conditions before significant changes in the RAS spectra could be measured. Figure 7.18 shows the RAS signal of Pb islands on Si(557)-In (this explains the shifted energy position of the peaks) up to five weeks after removing from the vacuum chamber. After five weeks the peaks have significantly reduced in intensity. Both peaks have also got broadened. A large peak has also formed in the UV that is most likely related to scattering in the capping layer.

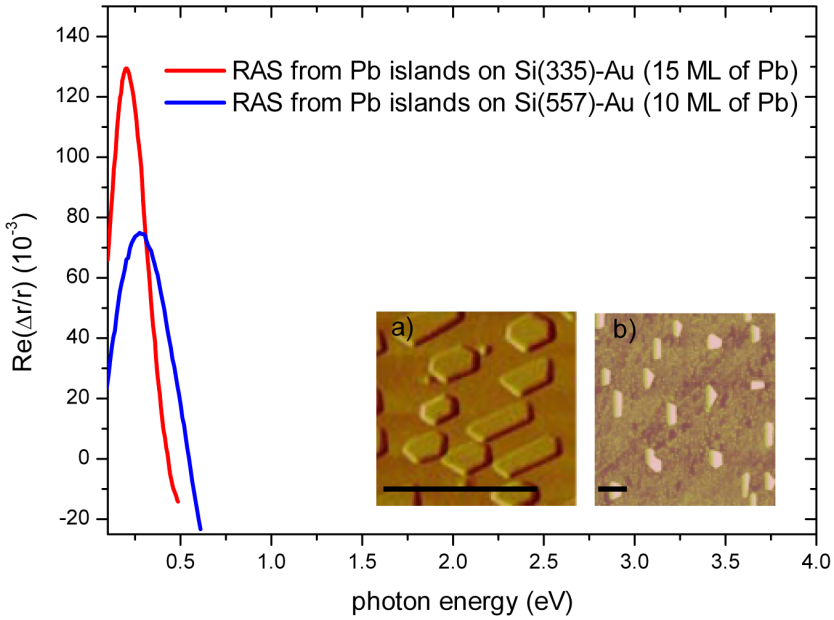

Figure 7.16: RAS spectra converted from the FTIR spectra of by Klevenz *et al* [40] and Chung *et al* [237] of Pb islands grown on Si(335)-Au and Si(557)-Au. The inset shows two AFM images a) Pb islands on Si(335)-Au and b) Pb islands on Si(557)-Au. The black bar in the images represents 1 μm.

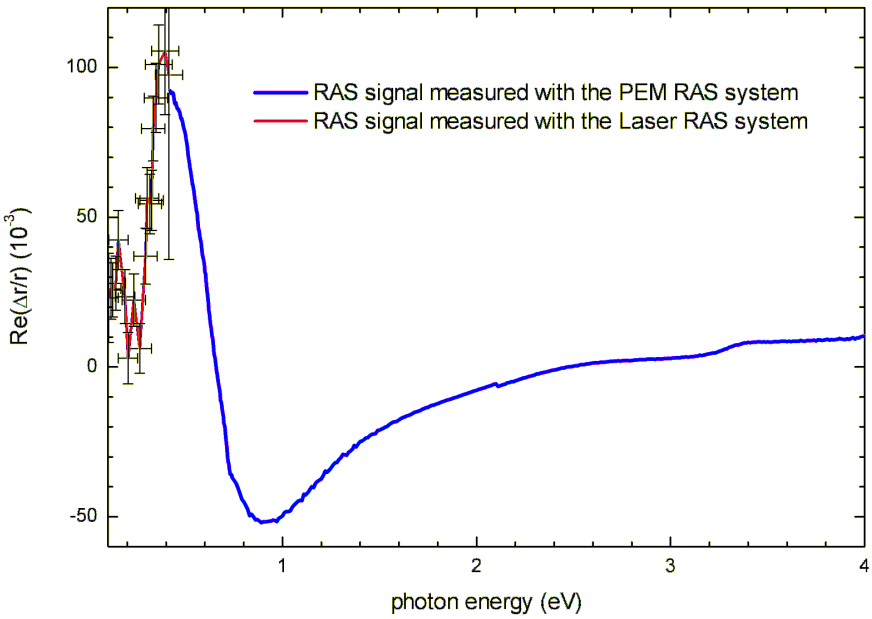

Figure 7.17: RAS signal from a-Si capped Pb islands after 8 ML of Pb had been deposited on Si(557)-Au. The PEM RAS signal was recorded *exsitu* and the laser RAS signal was recorded soon after the sample was removed from the chamber.

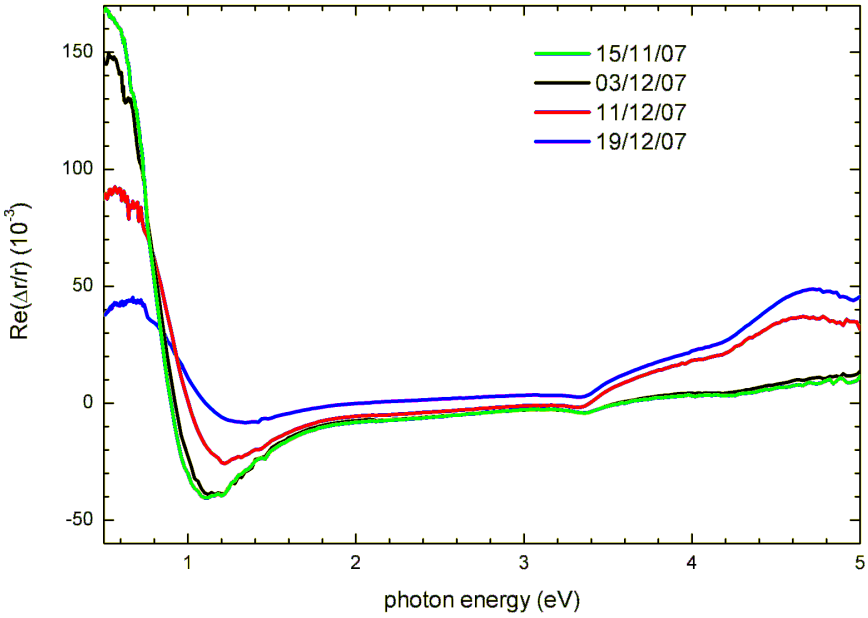

Figure 7.18: RAS signal from a-Si capped Pb islands, grown on Si(557)-In, on various dates after removal from the vacuum chamber.

7.3.3 SEM images from Pb wires grown on Si(557)-Au

To investigate the dimensions of the Pb islands grown, SEM images were recorded after removing the uncapped samples from the UHV chamber. Images were then analysed using Gwyddion image analysis software to find out average length and width. Figures 7.19 and 7.20 show the islands after 8 ML of Pb and 2.5 ML of Pb respectively. The high coverage shows islands with a typical width of 60 nm, with some islands coalescing into islands of double or triple that width. The length distribution is from 170 nm to 430 nm. For the lower coverage, islands have a average width of 45 nm and a length distribution from 50 nm to 260 nm. This indicates that the islands are growing mainly in length as Pb is deposited. Previous work has indicated that the height of the islands is relatively uniform (∼12nm) in this coverage region [40]. For the high coverage 34% of the surface was covered in islands and each island was found to have a mean area of $\sim 10^4$ nm^2, giving an island density of $\sim 3 \times 10^{-5}$ nm^{-2}. For the lower coverage of islands, the coverage was 31% and and each island was found to have a mean area of $\sim 5 \times 10^3$ nm^2, giving an island density of $\sim 6 \times 10^{-5}$ nm^{-2}. The average inter-island distance was estimated $\sim$ 100 nm for both coverges. However, it is clear from the SEM images of the high coverage that the distance is not uniform between the x and y direction. The islands are spaced $\sim$ 50 nm in the y direction and $\sim$ 190 nm in the x direction.

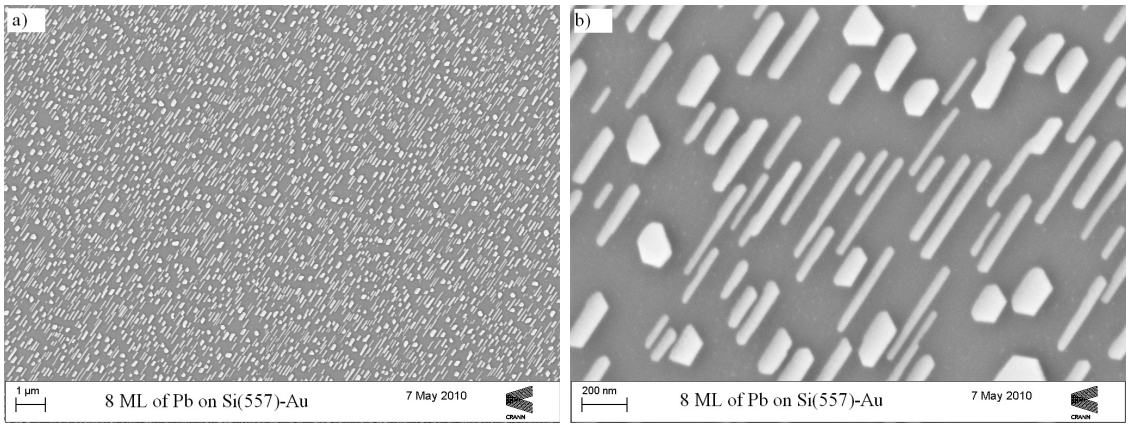

Figure 7.19: SEM image of 8 ML of Pb on Si(557)-Au, recorded with an electron energy of 3 keV. a) A large area of the surface, demonstrating the surface uniformity achieved with little or no defects. b) A close up image of a cluster of several islands.

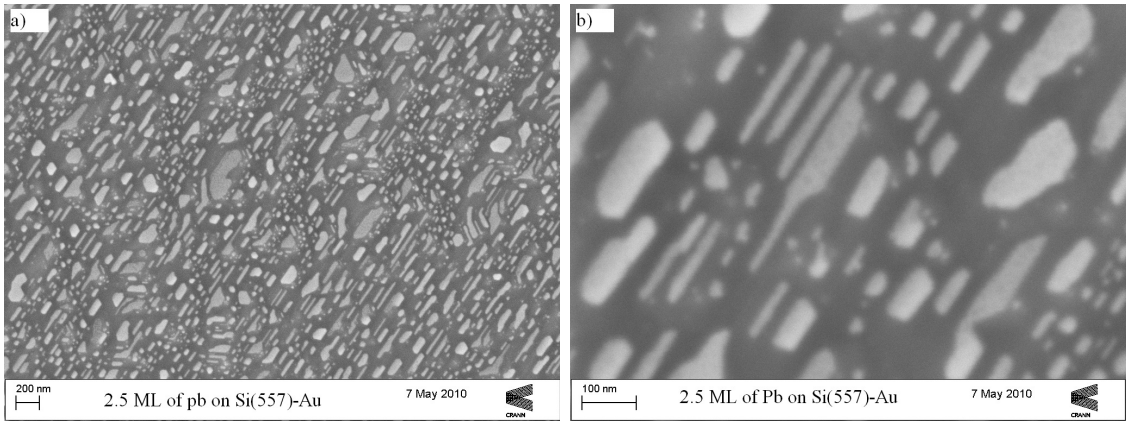

Figure 7.20: SEM image of 2.5 ML of Pb on Si(557)-Au, recorded with an electron energy of 3 keV. a) A large area of the surface. b) A close up image of a cluster of several islands.

For the low coverage the inter-island distance seems to be more uniform between the x and y directions. At these separations the dipole-dipole interaction is not expected to be large.

7.4 Fitting of the RAS results to the model

Using the information gathered from the SEM images the RAS spectra were fitted using equation 7.11 which neglects the dipole-dipole interaction. Fits were first modified by eye to acquire good initial values for a least squares fit, using Excel's "Solver" application to minimise the square of the difference between the experimental result and the predicted RAS spectra. Limitations were put on several values to prevent non-physical solutions. Values for the width and length were only allowed

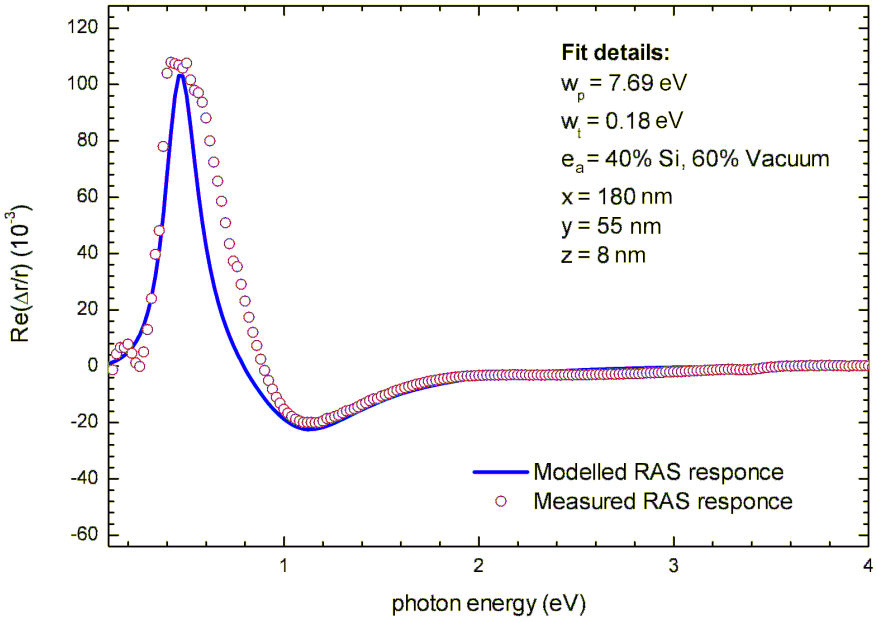

Figure 7.21: RAS spectrum from uncapped Pb islands, compared to the anisotropic ellipsoid model, including an image charge.

to vary within the range of values seen in the SEM images, while the values of ω_p and $\omega_{\tau,b}$ were fixed at the bulk values for the metal in question. However, the value of C in equation 7.2 was allowed to change between the capped and uncapped case. Increasing C has the effect of broadening the negative peak while leaving the positive peak largely unchanged. It is known that C depends on the scattering from the surface of the islands, so it would be expected to change as the dielectric function embedding medium changes [222, 223].

7.4.1 Fitting the RAS spectra from Pb islands

Figure 7.21 shows the fit for the uncapped islands. The best fit was for islands with a length of 180 nm, width of 55 nm and height of 8 nm. This shows good agreement with the SEM images and previous work reporting a width of 60 nm [39]. The predicted maximum is, however, significantly narrower than the measured RAS spectrum, while the minimum is reasonably well reproduced. Given that the major variation observed is in the length of the islands, and figure 7.8 shows that this will alter the position of the maximum, the broadening of the maximum may originate in the length distribution. The density of islands was allowed to vary freely within a certain range, and the best fit value came out as $\sim 5 \times 10^{-5}$ nm^{-2}, which is consistent with the density of islands seen in the SEM images.

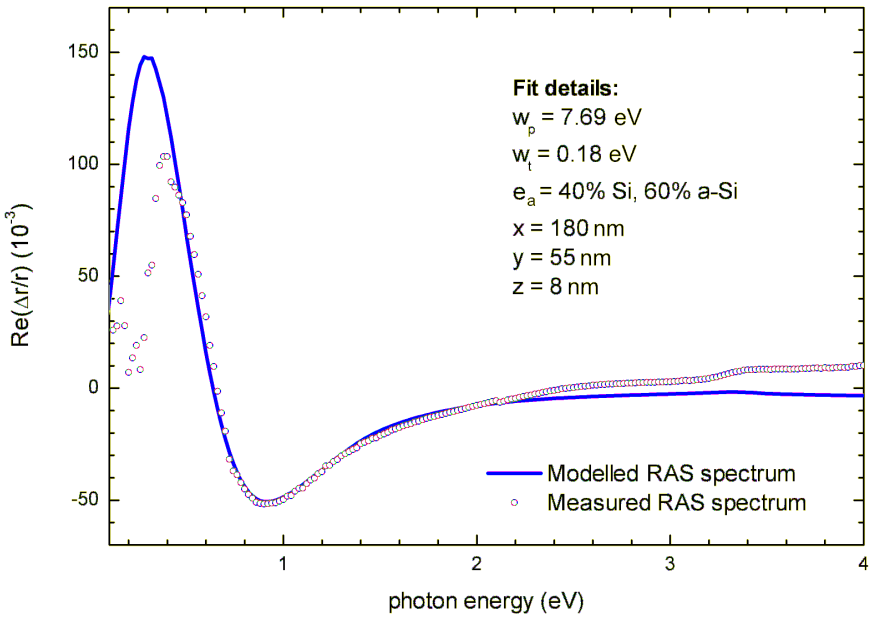

Figure 7.22: RAS spectrum from capped Pb islands, compared to the anisotropic ellipsoid model including an image charge.

The peak position observed for the Pb islands of 0.47 eV was also used to calculate the antenna length of the islands from the nanoantenna model (equation 7.13). This came out as $\sim$ 220 nm, which is in reasonable agreement with the SEM images.

Figure 7.22 shows the fit for the capped islands. The same length, width and height were used as the uncapped case. The capping dielectric function was changed to a combination of Si and a-Si and the value of C in equation 7.2, was used as a variable in the fitting routine. It was found that the signal produced was approximately 10 times smaller than the signal observed in the RAS spectra, and in the models for the uncapped system. This is mainly due to the numerator in equation 7.11, $(\epsilon - \epsilon_a)$, getting significantly smaller as ϵ_a is increased. This result underlines that comparison of the uncapped and capped response is a severe test of the theoretical modelling, particularly where the substrate material is used for capping, as this eliminates the image charge. The results presented are simply scaled to the negative peak intensity.

The negative peak position and shape match the spectra well, but the shift in the positive peak is significantly greater than the shift that was observed in the RAS experiment.

The peak position observed for the capped Pb islands of 0.39 eV was used to calculate the antenna length of the islands. This came out as $\sim$ 180 nm, which is reasonable, but differs significantly from the uncapped value of 220 nm. While this

might indicate an average length change due to Ostwald ripening, it may also reflect the limitations of the nanoantenna model, particularly the effective medium model applied.

7.4.2 Fitting the RAS spectra from Ag islands grown on Si(111)-3×1-Ag

The RAS spectra of the Ag Islands were recorded by Dr Julie Jacob in this research group and the AFM images were recorded by Dr Sandhya Chandola in the Technische Universität Berlin at the request of this research group. The length and width of the Ag islands can be estimated from the AFM image in figure 7.1. Values of 80 nm for the length and 40 nm for the width were calculated. Using the bulk plasma frequency (ω_p) and scattering rate ($\omega_{\tau,b}$) for Ag (table 7.1), the RAS spectra were fitted using equation 7.11. Similar to the Pb case, the embedding dielectric function for the uncapped system was taken as a combination of Si and vacuum, while for the capped case it was taken as a combination of Si, a-Si and vacuum. The value of C in equation 7.2 was used as a fitting parameter and a scaling factor was included for the capped case so that the observed RAS signal matched the calculated RAS signal amplitude. Figure 7.23 shows the fits for the uncapped Ag islands. The fits are less constrained than fits for the Pb case because no information on the maximum amplitude or position is available. However, good agreement is found for the minimum shape and position for islands that are 90 nm long, 40 nm wide and 5 nm high. The error on the length will be very large because the maximum position could not be recorded at the time. The values are close to those measured in the AFM images.

When the islands are capped with a-Si the minimum position is found to shift to the IR and increase in amplitude, similar to the Pb island case. When modelling the spectrum the embedding medium was changed from 40 % Si, 60% vacuum to 40 % a-Si, 40 % Si, 20 % vacuum. The 20 % vacuum was introduced to reduce the IR shift on capping, discussed in the previous section. A 20% void in the a-Si layer is unlikely and it is more likely that the limitations of the model are being exposed. The spacing of the Ag islands is much less than that of the Pb islands, and so the dipole-dipole interaction, neglected in the model, is likely to be more significant.

The main conclusion from this section is that it is essential to extend the RAS measurements as far as possible into the IR, if RAS is to be used as a quantitative tool for these surfaces.

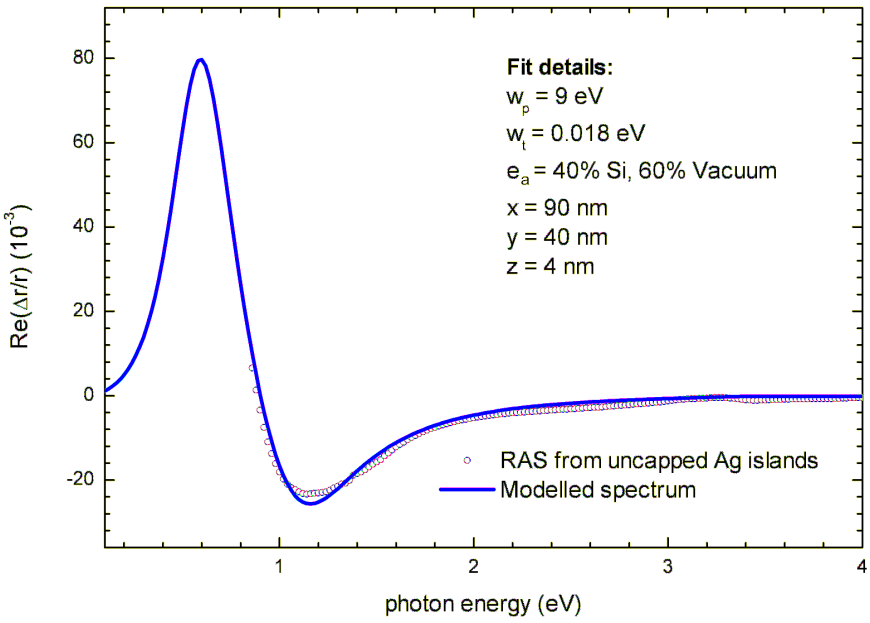

Figure 7.23: Comparison between the modelled and recorded RAS spectra for uncapped Ag islands, grown on Si(111)-3×1-Ag (data from [7]).

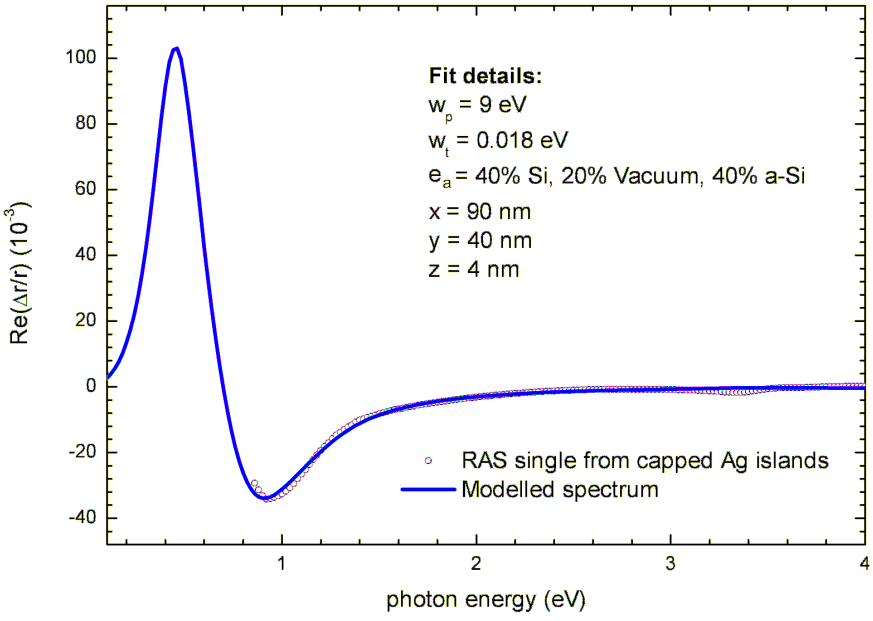

Figure 7.24: Comparison between the modelled and recorded RAS spectra for a-Si capped Ag islands, grown on Si(111)-3×1-Ag (data from [7]).

7.4.3 Limitations of the different models

These experiments have shown that RAS is very sensitive to nanoisland structure and the surrounding medium. In developing the model, image charge effects were introduced for the uncapped system, anisotropic scattering rates were introduced into the free electron plasmon response, and a simple average was taken as the effective medium response of the surrounding medium. Quadrupolar and higher order effects were neglected and, although no distinct quadrupolar structure was observed, these effects might produce a peak shift, even for these relatively small islands citebeitia99. The neglect of the dipole-dipole interaction between islands may be more significant, particularly for the more closely spaced Ag islands. The neglect of interband transitions in the model is not expected to be significant in the spectral area of interest. The SEM and AFM images show that assuming ellipsoidal islands is also an approximation and, where the shapes are significantly faceted, it is possible that quadrupolar effects will become more important.

7.5 Summary

Elongated Pb islands with lengths of up to 430 nm, and widths of 60 nm, were grown on Si(557)-Au. The islands showed a strong RAS signal with a negative peak at 1.1 eV and a positive peak at 0.47 eV. The islands were stable in ambient for approximately one week. The Pb islands were also capped and their RAS signal was retained with only small changes. Both peaks shifted to the IR. Capped samples retained their RAS signal for several weeks. The experimental results showed that the capping with a-Si was largely successful. Modelling of the RAS spectra was less successful.

The nanoantenna approach gave reasonable values of the average length of the Pb islands using the position of the maximum, but provided no information about the minimum or the line shape. Also, the differences in the uncapped and capped average lengths is likely to be due to limitations of the model. The other approach, which attempted to predict the full spectral line shape, neglected both quadrupolar effects and dipole-dipole interactions between islands.

The problem of calculating the optical response of anisotropic metallic islands arranged in anisotropic arrays on a surface, and subsequently capped, remains in practical terms unsolved. The discrete dipole approximation [238] can be used with a very fine mesh, but the computer time is prohibitive. The main conclusions of this chapter are that it is possible to cap nanoislands and retain useful anisotropic

optical properties, that RAS is a sensitive *in situ* probe of the nanoislands structure, provided the spectral response is extended as far as possible into the IR, and that the comparison of uncapped and capped spectra are a severe test for models of the optical response.

8 Conclusions and future work

8.1 Overview

The main objectives of this thesis were to use linear optical techniques to study the characteristics of *quasi* 1-D structures grown on Si(111) and secondly, to study the capping of 1-D structures with a-Si. Optical techniques are an ideal technique for studying the capping of materials because light has a large penetration depth and can probe buried interfaces.

The linear optic technique used in this thesis was RAS. It measures the reflectance anisotropy in two orthogonal polarisation directions at normal incidence. It achieves surface and interface sensitivity when the bulk material is isotropic and only the surface or interface has an anisotropic signal. For studying the 1-D structures in this work the RAS system was extended into the IR. Two systems were developed, a PEM RAS system which could work from 0.42 eV to 5 eV, and a rotating sample based system which worked from 0.12 eV to 0.4 eV

A strong optical anisotropy was seen on the Si(111)-5×2-Au surface, which is related to the Au chain structures on the surface. This consisted of a broad negative peak from 1.5 eV to 2.5 eV, and a positive peak at 1 eV. The monolayer coverage of Au required for this surface is controversial with values of 0.4 ML and 0.6 ML both being suggested. By taking into account the areas of the surface associated with steps, the coverage for a perfect singular Si(111)-5×2-Au surface has been calculated from the RAS response. Coverages of 0.59 ML ± 0.08 ML were found, consistent with the new three chain model proposed by Erwin *et al* [24]. The optical anisotropy was removed upon capping the Si(111)-5×2-Au surface with as little as 0.5 ML of a-Si.

When adatoms were deposited on the Si(111)-5×2-Au surface at room temperature the RAS spectra was consistent with the adatoms being immobile. Subsequent heating caused the RAS signal to change drastically, as the adatom decorated "5×4" reconstruction was formed. Temperature dependent studies allowed 100% and 0% adatom filled sites RAS spectra to be extracted. These spectra will be particularly useful for comparison with future *ab initio* LDA-DFT optical response calculations. The optical signatures from this surface could prove to be very interesting in the study of defect induced CDWs.

A strong optical anisotropy was also seen on the Si(775)-Au and Si(557)-Au surface. It had many of the same features as the Si(111)-5×2-Au RAS signature, but the line shape was significantly different. Upon capping the Si(775)-Au surface

most of the optical anisotropy was also removed, but the signal around the bulk critical points of Si remained and shifted to lower energy as the capping layer got thicker.

The RAS response of Si(557) and Si(775) was compared with preliminary *ab initio* LDA-DFT calculations. Given the difficulty of *ab initio* optical response calculations, this initial work has been quite successful in reproducing the RAS spectra from Si(557). A bulk terminated and relaxed Si(557) surface provided the best fit. The structure at 1.2 eV may come from either a Pandey-type chain or a dangling bond state at the step edge. As Pandey-type chain structures have produced RAS signatures at significantly lower energy than the structure recorded here, the dangling bond state at the step edge is the more likely candidate. However, on this surface there is good experimental evidence that a triple step structure is formed with the triple step having a Si(112) orientation. None of the various Si(112) reconstructed surfaces tested showed promising RAS signals in the region of 1.2 eV. It is therefore necessary to use a larger unit cell covering the full triple step and Si(111)-7×7 terrace.

Elongated Pb islands with lengths of up to 430 nm and widths of 60 nm were grown on Si(557)-Au. The wires showed a strong RAS signal with a negative peak at 1.1 eV and a positive peak at 0.47 eV. The Pb islands were capped with a-Si and their reflection anisotropy was retained with only small changes. Both peaks shifted to the IR. Capped samples retained their RAS signal for several weeks. The results showed that capping with a-Si was largely successful.

The modelling of the RAS response from the elongated Pb islands was, however, less successful. The nanoantenna approach gave reasonable values of the average length of the Pb islands using the position of the maximum, but provided no information about the minimum or the lineshape, and was not able to fully reproduce the shift to the IR on capping the islands. Other models which attempted to predicted the line shape could reproduce either the minimum or maximum accurately, but not both. However, the models neglected both quadrupolar effects and dipole-dipole interactions between islands.

8.2 Outlook

RAS has been shown to be an extremely sensitive tool for *quasi*-1-D surfaces, especially in the IR. Studies of the temperature dependence of the RAS signal on all the Si(111)-Au systems would be interesting and could put further limits on the current structural models. Using RAS it may be possible to study important metallic to

insulating phase transitions in the Si(111)-Au systems. Using *ab initio* methods to calculate the optical properties of these surfaces is very important not only to gain a full understanding of the RAS signal, but also because probing both filled and empty states provides a severe test of structural models and has the potential to resolve at least some of the current controversies surrounding *quasi*-1-D structures grown on Si [25]. The work in chapter 6 should lay a firm foundation for future work on Si(111)-Au surfaces.

The Pb islands discussed in chapter 7 show strong plasmon resonances in the IR. These resonances are mainly related to their dimensions. It has been shown by others that an optimum length to width ratio is achieved at temperatures slightly below room temperature. RAS could be used to optimise this system if the peak in the IR can be monitored during growth. The problem of calculating the optical response of anisotropic metallic islands arranged in anisotropic arrays on a surface, and subsequently capped, remains in practical terms unsolved. A solution would be to use the discrete dipole approximation with a very fine mesh of dipoles, but the computation time would be prohibitive. Ideally an analytical model of the optical response should be found. The comparison of uncapped and capped spectra would be a severe test for this new model of the optical response.

A Jones matrices

The Jones matrix method is a useful method to help understand optical systems where polarisation is important. It was first described by R.C. Jones in 1941 [239, 240]. Each different input polarisation of light is assigned a 1×2 matrix (vector) and each component is assigned a 2×2 matrix. The effect of a series of components can be established by multiplying the matrices. The Jones method does have some limitations, it cannot deal with depolarised or partially polarised light. For this the more general Muller matrix method should be used. The Jones vector is generally defined as:

$$\begin{pmatrix} E_x e^{i\phi} \\ E_y e^{i\phi} \end{pmatrix} \tag{A.1}$$

Where E_i is the electric field intensity and $e^{i\phi}$ is the phase. It is normal to normalize the magnitude of this vector. The following are the most common input vectors that can be used.

Linear (x-direction) $\begin{pmatrix} 1 \\ 0 \end{pmatrix}$

Linear (y-direction) $\begin{pmatrix} 0 \\ 1 \end{pmatrix}$

Linear (45° from axis) $\frac{1}{\sqrt{2}} \begin{pmatrix} 1 \\ 1 \end{pmatrix}$

Right Circular $\frac{1}{\sqrt{2}} \begin{pmatrix} 1 \\ -i \end{pmatrix}$

Left Circular $\frac{1}{\sqrt{2}} \begin{pmatrix} 1 \\ i \end{pmatrix}$

Common components are:

Linear polariser (x-direction) $\begin{pmatrix} 1 & 0 \\ 0 & 0 \end{pmatrix}$

Linear polariser (y-direction) $\begin{pmatrix} 0 & 0 \\ 0 & 1 \end{pmatrix}$

Linear polariser (45° from axis) $\frac{1}{2} \begin{pmatrix} 1 & 1 \\ 1 & 1 \end{pmatrix}$

Half Wave Plate $\begin{pmatrix} Cos2\theta & Sin2\theta \\ Sin2\theta & -Cos2\theta \end{pmatrix}$

Quarter wave plate $\begin{pmatrix} Cos^2\theta + iSin^2\theta & (1-i)Sin\theta Cos\theta \\ (1-i)Sin\theta Cos\theta & Sin^2\theta + iCos^2\theta \end{pmatrix}$

Here θ is the angle between the fast axis and the x axis.

B FlexRAS LabView Program

A LabView program was written to record RAS spectra. This program was designed to be flexible in allowing the user to exchange many of the components to suit the samples being tested. Its basic logic was quite simple, it proceeded as follows.

1.	Initialise Components	1. Set PEM voltage for required start energy
		2. Set to detector for required start energy
		3. Set time constant
		4. Set filter to dark
		5. Read dark DC
		6. Set filter for required energy
		7. Set monochromator for required energy
		8. Read AC voltage and optimise sensitivity
2.	Measuring	1. Set PEM voltage for required energy
		2. Set monochromator for required energy
		3. Set filter for required energy
		4. Check detector (If needs to be changed go to 4.1)
		5. Read AC
		6. Check sensitivity (optimise if needed and read AC again)
		7. Read DC
3.	Calculating RAS	1. Take AC value and scale by any damping factor
		2. Take DC value and subtract dark DC
		3. Divide corrected AC by corrected DC
		4. Save energy, RAS, AC and DC
		5. Step energy and return to point 2.1, until finish energy is reached
4	Changing detector	1. Change to detector needed
		2. Set filter to Dark
		3. Record Dark DC
		4. Set filter to required for energy
		5. Return to point 2.4

Included here are some screen shots of the various modes of operation of the RAS LabView program.

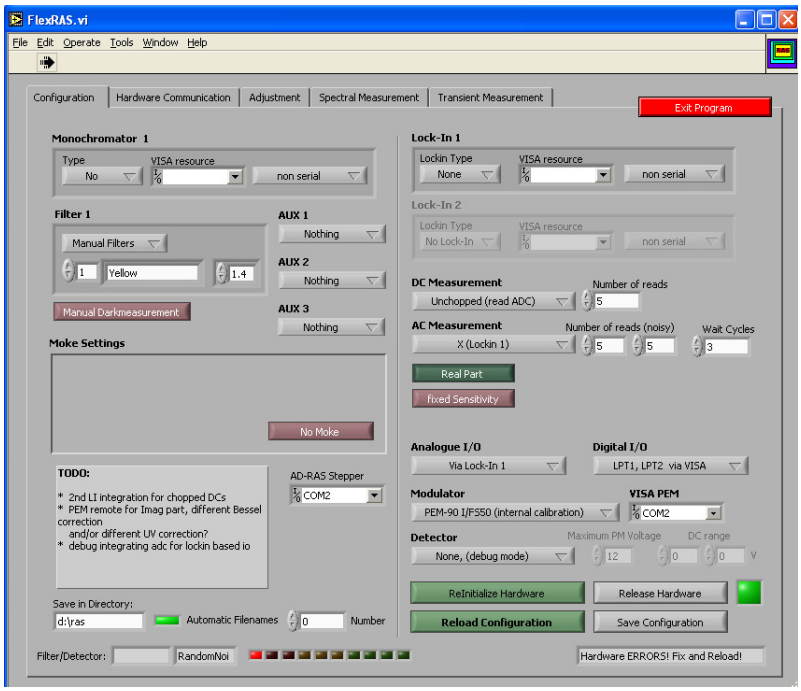

Figure B.1: The front panel of the RAS LabView code, options are selected to do with the different components being used and various measurement options such as wait times between readings and number of times to record each point can also be adjusted.

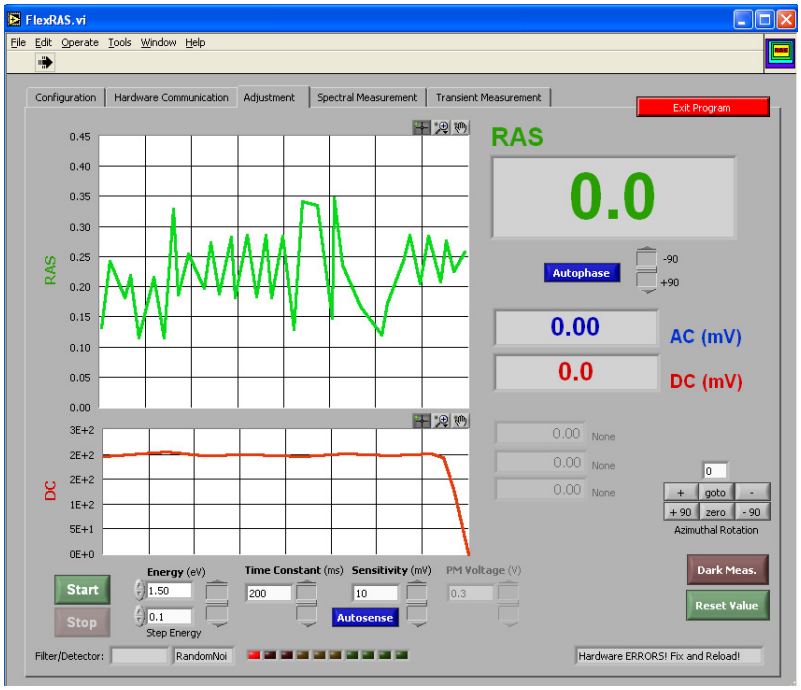

Figure B.2: The Adjustment mode, this mode is used for alignment

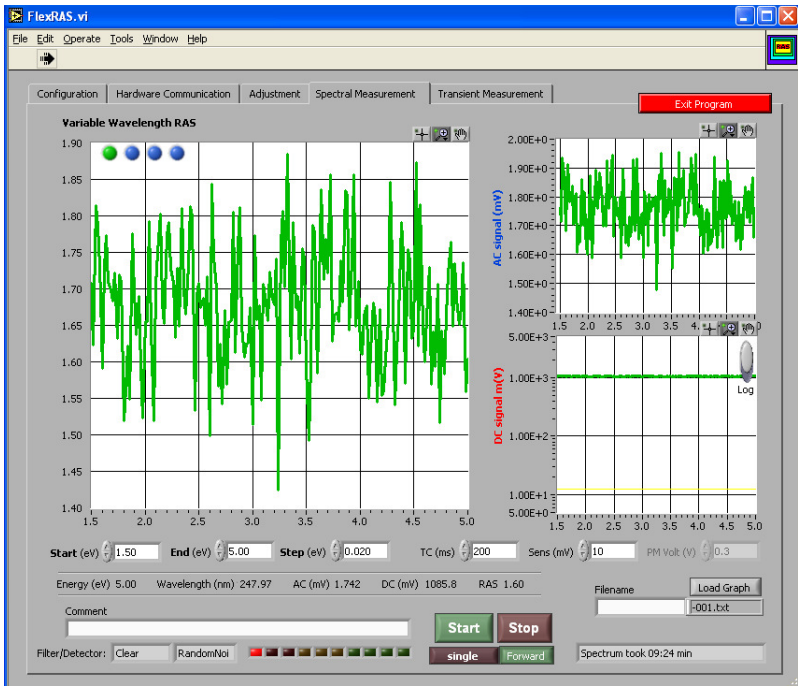

Figure B.3: Main Spectral mode, the energy is stepped and points are recorded. Changes can be made to energy step size, time constant, start and finish energy. Spectra can be recorded both forwards (IR-UV) and backwards (UV-IR). Multiple spectra can also be recorded. The sensitivity is optimised automatically as the spectra is recorded.

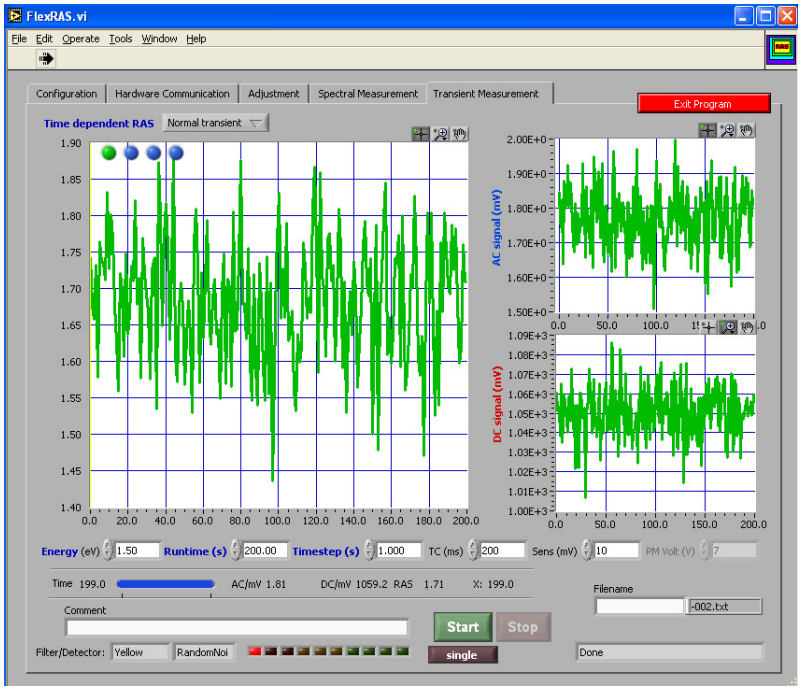

Figure B.4: Transient mode allows changes at a particular energy to be monitored over time. Any energy can be chosen and the lenght of time to record for can be changed.

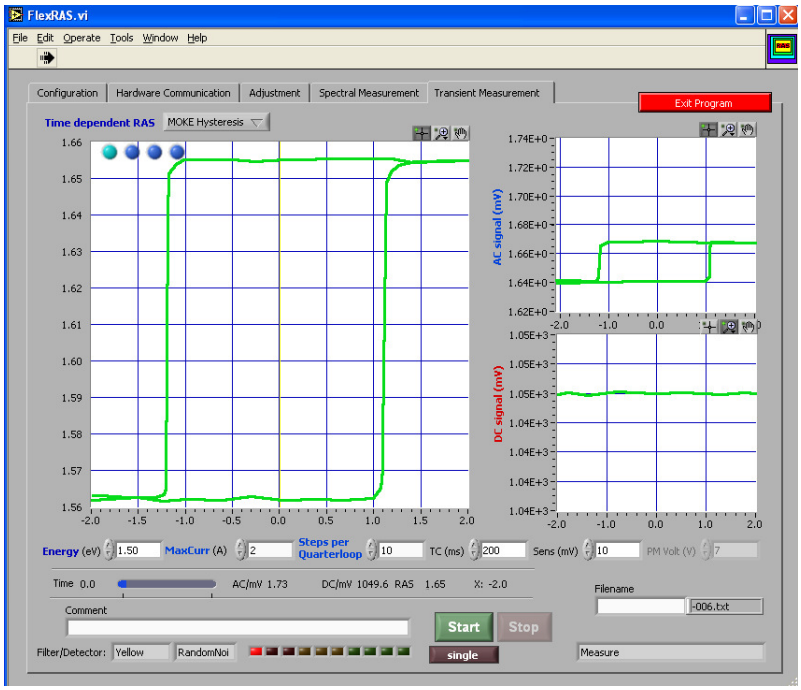

Figure B.5: Hysteresis mode allows changes in RAS signal at a particular energy to be monitored as the magnetic field changes. This mode is used for MOKE measurements. Spectroscopic measurements can also be recorded with a constant magnetic field

C Excel fitting worksheet

An excel worksheet was created to model the RAS response from anisotropic islands on a Si surface. It was made to be extremely flexible and could output a variety of different measurable parameters such as the real and imaginary part of the RAS signal and the ellipsometric parameters $\tan\Phi$ and $\cos\Delta$. The program has a set of initial varribles that are used to calculate firstly the dielectric functions for the metals and capping layer as well as depolarisation factors. These are then used to calculate $r_{s,x}$, $r_{s,y}$, $r_{p,x}$ and $r_{p,y}$. Which can be used in combination with angular inputs to calculate the RAS signal and the ellipsometric parameters $\tan\Phi$ and $\cos\Delta$.

Initial Variables

The following are the initial variables that control the dielectric function of the metals, the depolarisation factors and other aspects of the system
Plasma Frequency of bulk metal: ω_p
Scattering Frequency of bulk metal: $\omega_{\tau,b}$
Fermi velocity of an electron in the metal: V_f
The dimensions of the wires: x, y and z
The coverage of the wires in ML was also used as an input
The scattering frequency for the x, y and z directions are then calculated with equation 7.2.
Using the values of x, y and z the depolarisation constants can be calculated, however excel had trouble solving the integral in equation 7.4. To get around this problem a look-up table for various values of x, y and z was created. The depolarisation constants were found to depend on the ratio of $x : y : z$ so to reduce the number of tables needed the value that was used for the lookup table was $x/z : y/z : 1$. The look-up tables had problems when multiple cells could have the same number, for example if you tell excel to look-up 8, it will find, 8, 18, 28 etc. To prevent this 1000 was added to each number before being used in the look-up table.
The volume of a single islands was calculated as was the RAS pre-factor ($4\pi i$) and density of the islands (based on the coverage)

Dielectric functions

Several dielectric functions are included in the worksheet, not all of them are used all the time. The real, imaginary and combination of the two are always included as it made later calculations slightly easier. The dielectric functions included were

Si, a-Si and Vacuum.
The metal dielectric function in direction x, y and z are calculated using the Drude dielectric function (equation 7.1).
The dielectric function of the embedding medium is calculated by combining an average of the substrate and the cap. This is done with two variables where the fraction of the islands covered by the substrate and the fraction covered by the cap are included.
The substrate refractive index is also needed for calculating $r_{s,x}$, $r_{s,y}$, $r_{p,x}$ and $r_{p,y}$ so it is calculated using : $n = \sqrt{\epsilon}$

Energy

The energy of the light is taken from 0.0001 to 7 eV. This is then converted into a wavelength (λ) and wavenumber (k). 0 energy is not used to prevent a divide by 0 error.

Polarisability

The depolarisation constants $N_i^{'}$ are first calculated using equation 7.10. The MLWA correction is also calculated using equation 7.5.
These depolarisation constants are used to calculate the polarisability in x, y and z using equation 7.11.

Output

To calculate the RAS and ellipsometric parameters $\tan\Phi$ and $\cos\Delta$ first $r_{s,x}$, $r_{s,y}$, $r_{p,x}$ and $r_{p,y}$ are calculated using the standard ellipsometry formula (equations 7.6 and 7.7). In the case of the normal incidence $r_{s,x} = r_{p,y}$ and $r_{s,y} = r_{p,x}$. This can be used to check for typos in the excel equations. As the excel does not handle complex numbers in an intuitive, tidy or consistent way this check was very useful.
Finally the real and imaginary part of the RAS signal and $\tan\Phi$ and $\cos\Delta$ could be calculated using:

$$RAS = \frac{2(r_{p,x} - r_{p,y})}{r_{p,x} + r_{p,y}} = \frac{2(r_{s,x} - r_{s,y})}{r_{s,x} + r_{s,y}} \tag{C.1}$$

$$\tan\Phi_i = Re\left(\frac{r_{p,i}}{r_{s,i}}\right) \tag{C.2}$$

$$\cos\Delta_i = Im\left(\frac{r_{p,i}}{r_{s,i}}\right) \tag{C.3}$$

References

[1] N. Oncel. Atomic chains on surfaces. *Journal of Physics Condensed Matter*, 20(39), 2008.

[2] H. Hirayama, R. Horie, and K. Takayanagi. Nucleation of Ag nanodots at the Si(111)-3×1-Ag surfaces. *Surface Science*, 482-485(Part 2):1277 – 82, 2001.

[3] J. Kuntze, A. Mugarza, and J. E. Ortega. Ag-induced zero- and one-dimensional nanostructures on vicinal Si(111). *Applied Physics Letters*, 81(13):2463–2465, 2002.

[4] S. Chandola, J. Jacob, K. Fleischer, P. Vogt, W. Richter, and J.F. McGilp. Optical and electronic properties of Ag nanodots on Si(111). *Journal of Physics Condensed Matter*, 18(30):6979 – 86, 2006.

[5] W. Lu and C. M Lieber. Semiconductor nanowires. *Journal of Physics D: Applied Physics*, 39(21):R387, 2006.

[6] N. McAlinden and J.F. McGilp. Using surface and interface optics to probe the capping, with amorphous Si, of Au atom chains grown on vicinal Si(111). *Journal of Physics: Condensed Matter*, 21(47):474208 – 13, 2009.

[7] K. Fleischer, J. Jacob, S. Chandola, N. Esser, and J.F. McGilp. Using reflectance anisotropy spectroscopy to characterize capped silver nanostructures grown on silicon. *Physica Status Solidi C*, 5(8):2556 – 60, 2008.

[8] J.F. McGilp and Y. Yeh. Probing the buried metal-semiconductor interface by optical second harmonic generation: Au on Si(111) and Si(100). *Solid State Communications*, 59(2):91 – 4, 1986.

[9] J.F. McGilp. Probing surface and interface structure using optics. *Journal of Physics: Condensed Matter*, 22(8):084018–34, 2010.

[10] K. Fleischer, S. Chandola, Th. Herrmann, N. Esser, W. Richter, and J. F. McGilp. Free-electron response in reflectance anisotropy spectra. *Phys. Rev. B*, 74(19):195432, 2006.

[11] T. Ito and S. Okazaki. Pushing the limits of lithography. *Nature*, 406(6799):1027 – 31, 2000.

[12] M. Kiffner, J. Evers, and M. S. Zubairy. Resonant interferometric lithography beyond the diffraction limit. *Phys. Rev. Lett.*, 100(7):073602, 2008.

[13] Wei Lu and C.M. Lieber. Nanoelectronics from the bottom up. *Nature Materials*, 6(11):841 – 50, 2007.

[14] A. Voigt. Growth mechanisms on stepped surfaces, from atomistic to step-flow models. *Journal of Crystal Growth*, 275(1-2):2251 – 55, 2005.

[15] J.N. Crain and F.J. Himpsel. Low-dimensional electronic states at silicon surfaces. *Applied Physics A: Materials Science and Processing*, 82, 2006.

[16] D. E. Aspnes and A. A. Studna. Anisotropies in the above band-gap optical spectra of cubic semiconductors. *Phys. Rev. Lett.*, 54(17):1956–9, 1985.

[17] P. Weightman, D.S. Martin, R.J. Cole, and T. Farrell. Reflection anisotropy spectroscopy. *Reports on Progress in Physics*, 68(6):1251 – 341, 2005.

[18] D. E. Aspnes, J. P. Harbison, A. A. Studna, and L. T. Florez. Application of reflectance difference spectroscopy to molecular-beam epitaxy growth of GaAs and AlAs. *Journal of Vacuum Science and Technology A: Vacuum, Surfaces, and Films*, 6(3):1327–32, 1988.

[19] P. Gambardella, S. Rusponi, T. Cren, N. Weiss, and H. Brune. Magnetic anisotropy from single atoms to large monodomain islands of Co/Pt(111). *Academie des Sciences. Comptes Rendus, Physique*, 6(1):75 – 87, 2005.

[20] T. Kizuka. Atomic configuration and mechanical and electrical properties of stable gold wires of single-atom width. *Phys. Rev. B*, 77(15):155401, 2008.

[21] A.K. Geim and K.S. Novoselov. The rise of graphene. *Nature Materials*, 6(3):183 – 191, 2007.

[22] A.A. Baski, S.C. Erwin, and L.J. Whitman. The structure of silicon surfaces from (001) to (111). *Surface Science*, 392(1-3):69 – 85, 1997.

[23] F. Jentzsch and M. Henzler. LEED investigations on pure and metal treated vicinal silicon(111). *Applied Physics A (Solids and Surfaces)*, A46(2):119 – 23, 1988.

[24] S. C. Erwin, I. Barke, and F. J. Himpsel. Structure and energetics of Si(111)-5×2-Au. *Phys. Rev. B*, 80(15):155409, 2009.

[25] S. Chandola, K. Hinrichs, M. Gensch, N. Esser, S. Wippermann, W. G. Schmidt, F. Bechstedt, K. Fleischer, and J. F. McGilp. Structure of Si(111)-In nanowires determined from the midinfrared optical response. *Phys. Rev. Lett.*, 102(22):226805, 2009.

[26] J. Jacob, A.G. Silva, K. Fleischer, and J.F. McGilp. Optical second-harmonic generation studies of Si(111)-$\sqrt{3} \times \sqrt{3}$-Ag and Si(111)-3×1-Ag grown on vicinal Si(111). *Physica Status Solidi C*, 5(8):2649 – 52, 2008.

[27] J.D. O'Mahony, J.F. McGilp, F.M. Leibsle, P. Weightman, and C.F.J. Flipse. Control of terrace width and atomic step distribution on vicinal Si(111) surfaces by thermal processing. *Semiconductor Science and Technology*, 8(4):495 – 501, 1993.

[28] J.-L. Lin, D. Y. Petrovykh, J. Viernow, F. K. Men, D. J. Seo, and F. J. Himpsel. Formation of regular step arrays on Si(111)7×7. *Journal of Applied Physics*, 84(1):255–260, 1998.

[29] I. R. Collins, J. T. Moran, P. T. Andrews, R. Cosso, J. D. Omahony, J. F. McGilp, and G. Margaritondo. Angle-resolved photoemission from an unusual *quasi*-one-dimensional metallic system - a single-domain Au-induced 5×2 reconstruction of Si(111). *Surface Science*, 325(1-2):45–49, 1995.

[30] J. N. Crain, J. L. McChesney, Fan Zheng, M. C. Gallagher, P. C. Snijders, M. Bissen, C. Gundelach, S. C. Erwin, and F. J. Himpsel. Chains of gold atoms with tailored electronic states. *Phys. Rev. B*, 69(12):125401, 2004.

[31] P. Segovia, D. Purdie, M. Hengsberger, and Y. Baer. Observation of spin and charge collective modes in one-dimensional metallic chains. *Nature*, 402(6761):504 – 7, 1999.

[32] R. Losio, K. N. Altmann, A. Kirakosian, J.-L. Lin, D. Y. Petrovykh, and F. J. Himpsel. Band splitting for Si(557)-Au: Is it spin-charge separation? *Phys. Rev. Lett.*, 86(20):4632–5, 2001.

[33] A. A. Baski, J. Nogami, and C. F. Quate. Si(111)-5 × 1-Au reconstruction as studied by scanning tunneling microscopy. *Phys. Rev. B*, 41(14):10247–9, 1990.

[34] Hasegawa T. Yagi K. and Hosoki S. Stable phase boundaries between the 7×7 and the 5×2 Au structures on a Si(111) surface studied by high-temperature STM. *Surface Science*, 355, 1996.

[35] S. C. Erwin. Self-doping of gold chains on silicon: A new structural model for Si(111)-5 × 2-Au. *Phys. Rev. Lett.*, 91(20):206101, 2003.

[36] R Bennewitz, J N Crain, A Kirakosian, J-L Lin, J L McChesney, D Y Petrovykh, and F J Himpsel. Atomic scale memory at a silicon surface. *Nanotechnology*, 13(4), 2002.

[37] F.-C. Chuang, C.-H. Hsu, C.-Z. Wang, and K.-M. Ho. Honeycomb chain structure of the Au-Si(111) - 5×2 surface reconstruction: A first-principles study. *Phys. Rev. B*, 77(15):153409, 2008.

[38] J. R. Power, P. Weightman, and J. D. O'Mahony. Strong optical anisotropy of the single-domain 5 × 2-Au reconstruction on vicinal Si(111). *Phys. Rev. B*, 56(7):3587–90, 1997.

[39] Jalochowski M. and Bauer E. Growth of metallic nanowires on anisotropic Si substrates: Pb on vicinal Si(001), Si(755), Si(533), and Si(110). *Surface Science*, 480:109–17, 2001.

[40] M. Klevenz, F. Neubrech, R. Lovrincic, M. Jalochowski, and A. Pucci. Infrared resonances of self-assembled Pb nanorods. *Applied Physics Letters*, 92(13):133116, 2008.

[41] J. M. Flores-Camacho, L. D. Sun, N. Saucedo-Zeni, G. Weidlinger, M. Hohage, and P. Zeppenfeld. Optical anisotropies of metal clusters supported on a birefringent substrate. *Phys. Rev. B*, 78(7):075416, 2008.

[42] Y. Iwasawa, W. Voegeli, T. Shirasawa, K. Sekiguchi, T. Nojima, R. Yoshida, T. Takahashi, M. Matsumoto, T. Okano, K. Akimoto, H. Kawata, and H. Sugiyama. Study of buried Si(111)-5 × 2-Au by surface X-ray diffraction. *Applied Surface Science*, 254(23):7803–6, 2008.

[43] S. Tomonaga. Remarks on Bloch's method of sound waves applied to many-fermion problems. *Progress of Theoretical Physics*, 5(4):544–569, 1950.

[44] J. M. Luttinger. An exactly soluble model of a many-fermion system. *Journal of Mathematical Physics*, 4(9):1154–1162, 1963.

[45] C. Kittel. *Introduction to Solid State Physics*. Wiley, 7th edition edition, 1996.

[46] J. Lefebvre, J.M. Fraser, Y. Homma, and P. Finnie. Photoluminescence from single-walled carbon nanotubes: a comparison between suspended and micelle-encapsulated nanotubes. *Applied Physics A: Materials Science & Processing*, 78:1107–1110, 2004.

[47] R. E. Peierls. *Quantum Theory of Solids*. Clarendon: Oxford, 1955.

[48] H. W. Yeom, S. Takeda, E. Rotenberg, I. Matsuda, K. Horikoshi, J. Schaefer, C. M. Lee, S. D. Kevan, T. Ohta, T. Nagao, and S. Hasegawa. Instability and charge density wave of metallic quantum chains on a silicon surface. *Phys. Rev. Lett.*, 82(24):4898–4901, 1999.

[49] C. González, J. Guo, J. Ortega, F. Flores, and H. H. Weitering. Mechanism of the band gap opening across the order-disorder transition of Si(111)-4×1-In. *Phys. Rev. Lett.*, 102(11):115501, 2009.

[50] M. Hashimoto, Y. Fukaya, A. Kawasuso, and A. Ichimiya. Phase transition of In/Si(111) surface studied by reflection high-energy positron diffraction. *e-Journal of Surface Science and Nanotechnology*, 7:436–440, 2009.

[51] K. Fleischer, L. Carroll, C. Smith, and J.F. McGilp. Optical reflectance anisotropy of buried Fe nanostructures on vicinal W(110). *Journal of Physics Condensed Matter*, 19(26), 2007.

[52] W. Voegeli, T. Takayama, K. Kubo, M. Abe, Y. Iwasawa, T. Shirasawa, T. Takahashi, K. Akimoto, H. Sugiyama, H. Tajiri, and O. Sakata. Surface X-ray diffraction study of the metal-insulator transition on the Si(553)-Au surface. *e-Journal of Surface Science and Nanotechnology*, 6:281–285, 2008.

[53] J. R. Ahn, P. G. Kang, K. D. Ryang, and H. W. Yeom. Coexistence of two different Peierls distortions within an atomic scale wire: Si(553)-Au. *Phys. Rev. Lett.*, 95(19):196402, 2005.

[54] J. L. McChesney, J. N. Crain, V. Pérez-Dieste, Fan Zheng, M. C. Gallagher, M. Bissen, C. Gundelach, and F. J. Himpsel. Electronic stabilization of a 5×4 dopant superlattice on Si(111)-5×2-Au. *Phys. Rev. B*, 70(19):195430, 2004.

[55] W. H. Choi, P. G. Kang, K. D. Ryang, and H. W. Yeom. Band-structure engineering of gold atomic wires on silicon by controlled doping. *Phys. Rev. Lett.*, 100(12):126801, 2008.

[56] V. Vescoli, L. Degiorgi, M. Dressel, A. Schwartz, W. Henderson, B. Alavi, G. Grüner, J. Brinckmann, and A. Virosztek. Spin-density-wave gap in the bechgaard salts $(TMTSF)_2X$. *Phys. Rev. B*, 60(11):8019–8027, 1999.

[57] N. Matsunaga, K. Yamashita, H. Kotani, K. Nomura, T. Sasaki, T. Hanajiri, J. Yamada, S. Nakatsuji, and H. Anzai. Spin-density-wave transition of $(TMTSF)_2PF_6$ at high magnetic fields. *Phys. Rev. B*, 64(5):052405, 2001.

[58] S. Watanabe, R. Kondo, S. Kagoshima, and R. Shimano. Spin-density-wave gap in $(TMTSF)_2PF_6$ probed by reflection-type terahertz time-domain spectroscopy. *Physica Status Solidi B*, 245(12):2688 – 91, 2008.

[59] A M Gabovich, A I Voitenko, J F Annett, and M Ausloos. Charge- and spin-density-wave superconductors. *Superconductor Science and Technology*, 14(4):R1, 2001.

[60] S. C. Erwin and F.J. Himpsel. Intrinsic magnetism at silicon surfaces. *Nature Communications*, 1(58), 2010.

[61] S. O. Koswatta, S. Hasan, M. S. Lundstrom, M. P. Anantram, and D. E. Nikonov. Ballisticity of nanotube field-effect transistors: Role of phonon energy and gate bias. *Applied Physics Letters*, 89(2):023125, 2006.

[62] S. Frank, P. Poncharal, Z. L. Wang, and W. A. Heer. Carbon Nanotube Quantum Resistors. *Science*, 280(5370):1744–1746, 1998.

[63] N. Agrat, A. Levy Yeyati, and J. M. van Ruitenbeek. Quantum properties of atomic-sized conductors. *Physics Reports*, 377(2-3):81 – 279, 2003.

[64] J Voit. One-dimensional Fermi liquids. *Reports on Progress in Physics*, 58(9):977, 1995.

[65] V. Vescoli, F. Zwick, W. Henderson, L. Degiorgi, M. Grioni, G. Gruner, and L.K. Montgomery. Optical and photoemission evidence for a Tomonaga-Luttinger liquid in the Bechgaard salts. *The European Physical Journal B - Condensed Matter and Complex Systems*, 13:503–511, 2000.

[66] H. Ishii, H. Kataura, H. Shiozawa, H. Yoshioka, H. Otsubo, Y. Takayama, T. Miyahara, S. Suzuki, Y. Achiba, M. Nakatake, T. Narimura, M. Higashiguchi, K. Shimada, H. Namatame, and M. Taniguchi. Direct observation of Tomonaga-Luttinger-liquid state in carbon nanotubes at low temperatures. *Nature*, 426(6966):540 – 4, 2003.

[67] H. Rauf, T. Pichler, M. Knupfer, J. Fink, and H. Kataura. Transition from a Tomonaga-Luttinger liquid to a Fermi liquid in potassium-intercalated bundles of single-wall carbon nanotubes. *Phys. Rev. Lett.*, 93(9):096805, 2004.

[68] C G Hwang, N D Kim, S Y Shin, and J W Chung. Possible evidence of non-Fermi liquid behaviour from *quasi*-one-dimensional indium nanowires. *New Journal of Physics*, 9(8):249, 2007.

[69] S. Sugai, N. Kaji, A. Osuka, K. Takenaka, S. Horii, and H. Ikuta. Tomonaga–Luttinger liquid–Fermi liquid transition in chain of $PrBa_2Cu_4O_8$. *Journal of the Physical Society of Japan*, 74(3):871–874, 2005.

[70] M Grioni, S Pons, and E Frantzeskakis. Recent ARPES experiments on *quasi*-1D bulk materials and artificial structures. *Journal of Physics: Condensed Matter*, 21(2):023201, 2009.

[71] S. Hasegawa. *Quasi*-one-dimensional metals on semiconductor surfaces with defects. *Journal of Physics: Condensed Matter*, 22(8):084026, 2010.

[72] Jérome, D., Mazaud, A., Ribault, M., and Bechgaard, K. Superconductivity in a synthetic organic conductor $(TMTSF)_2PF_6$. *J. Physique Lett.*, 41(4):95–98, 1980.

[73] V. Vescoli, L. Degiorgi, K. P. Starkey, and L. K. Montgomery. Anisotropy in the optical response of $(TMTTF)_2X$ (X=PF_6 and Br) Bechgaard salts. *Solid State Communications*, 111(9):507 – 512, 1999.

[74] A B Kaiser. Electronic transport properties of conducting polymers and carbon nanotubes. *Reports on Progress in Physics*, 64(1):1, 2001.

[75] A. Rahman and M. K. Sanyal. Observation of charge density wave characteristics in conducting polymer nanowires: Possibility of Wigner crystallization. *Phys. Rev. B*, 76(4):045110, 2007.

[76] K. Lee and A.J. Heeger. Optical reflectance studies of conducting polymers on the metal-insulator boundary. *Synthetic Metals*, 84(1-3):715 – 718, 1997.

[77] R. Turcu, M. Brie, G. Leising, A. Niko, V. Tosa, A. Mihut, and A. Bot. Correlation between the electrochemical synthesis conditions and the optical properties of polypyrrole. *Synthetic Metals*, 84(1-3):825 – 826, 1997.

[78] P. Poncharal, C. Berger, Y. Yi, Z. L. Wang, and W. A. de Heer. Room temperature ballistic conduction in carbon nanotubes. *The Journal of Physical Chemistry B*, 106(47):12104–12118, 2002.

[79] K. Iakoubovskii, N. Minami, Y. Kim, K. Miyashita, S. Kazaoui, and B. Nalini. Midgap luminescence centers in single-wall carbon nanotubes created by ultraviolet illumination. *Applied Physics Letters*, 89(17):173108, 2006.

[80] K. Mizuno, J. Ishii, H. Kishida, Y. Hayamizu, S. Yasuda, D.N. Futaba, M. Yumura, and K. Hata. A black body absorber from vertically aligned single-walled carbon nanotubes. *Proceedings of the National Academy of Sciences of the United States of America*, 106(15):6044 – 7, 2009.

[81] K. Kamaras, A.G. Rinzler, D.B. Tanner, and D.A. Walters. Polarization-dependent optical reflectivity in magnetically oriented carbon nanotube networks. *Physica Status Solidi B*, 243(13):3126 – 9, 2006.

[82] K. W. Schwarz and J. Tersoff. From droplets to nanowires: Dynamics of vapor-liquid-solid growth. 102(20):206101, 2009.

[83] P. R. Bandaru and P. Pichanusakorn. An outline of the synthesis and properties of silicon nanowires. *Semiconductor Science and Technology*, 25(2):024003, 2010.

[84] M. Kiguchi, N. Sekiguchi, and K. Murakoshi. Electric conductance of metal nanowires at mechanically controllable break junctions under electrochemical potential control. *Surface Science*, 601(22):5262 – 5265, 2007.

[85] X.-S. Zhou, Y.-M. Wei, L. Liu, Z.-B. Chen, J. Tang, and B.-W. Mao. Extending the capability of STM break junction for conductance measurement of atomic-size nanowires: An electrochemical strategy. *Journal of the American Chemical Society*, 130(40):13228–13230, 2008.

[86] H. Ohnishi, Y. Kondo, and K. Takayanagi. Quantized conductance through individual rows of suspended gold atoms. *Nature*, 395(6704):780 – 3, 1998.

[87] I. Matsuda, M. Hengsberger, F. Baumberger, T. Greber, H. W. Yeom, and J. Osterwalder. Reinvestigation of the band structure of the Si(111)-5×2-Au surface. *Phys. Rev. B*, 68(19):195319, 2003.

[88] Snijders, P. C., Rogge, S., and Weitering, H. H. Density waves in atomic necklaces. *Europhysics News*, 37(5):27–30, 2006.

[89] S. S. Lee, J. R. Ahn, N. D. Kim, J. H. Min, C. G. Hwang, J. W. Chung, H. W. Yeom, S. V. Ryjkov, and S. Hasegawa. Adsorbate-induced pinning of a charge-density wave in a *Quasi*-1D metallic chains: Na on the In/Si(111)-4×1 surface. *Phys. Rev. Lett.*, 88(19):196401, 2002.

[90] J. R. Ahn, H. W. Yeom, H. S. Yoon, and I.-W. Lyo. Metal-insulator transition in Au atomic chains on Si with two proximal bands. *Phys. Rev. Lett.*, 91(19):196403, 2003.

[91] D. Sánchez-Portal, S. Riikonen, and R. M. Martin. Role of spin-orbit splitting and dynamical fluctuations in the Si(557)-Au surface. *Phys. Rev. Lett.*, 93(14):146803, 2004.

[92] H. S. Kim, S. Y. Shin, S. H. Uhm, C. C. Hwang, D. Y. Noh, and J. W. Chung. Evidence of metallic nature of the surface bands of Au/Si(557). *Phys. Rev. B*, 80(3):033412, 2009.

[93] M. Krawiec, T. Kwapiński, and M. Jalochowski. Double nonequivalent chain structure on a vicinal Si(557)-Au surface. *Phys. Rev. B*, 73(7):075415, 2006.

[94] H. W. Yeom, J. R. Ahn, H. S. Yoon, I.-W. Lyo, H. Jeong, and S. Jeong. Real-space investigation of the metal-insulator transition of Si(557)-Au. *Phys. Rev. B*, 72(3):035323, 2005.

[95] J.-H. Han, H. S. Kim, H. N. Hwang, B. Kim, S. Chung, J. W. Chung, and C. C. Hwang. Direct evidence of the step-edge buckling at the Au/Si(557)-1×2 surface. *Phys. Rev. B*, 80(24):241401, 2009.

[96] P. C. Snijders and H. H. Weitering. Electronic instabilities in self-assembled atom wires. *Rev. Mod. Phys.*, 82(1):307–329, 2010.

[97] M. Krawiec. Structural model of the Au-induced Si(553) surface: Double Au rows. *Phys. Rev. B*, 81(11):115436, 2010.

[98] I. Barke, F. Zheng, S. Bockenhauer, K. Sell, V. v. Oeynhausen, K. H. Meiwes-Broer, S. C. Erwin, and F. J. Himpsel. Coverage-dependent faceting of Au chains on Si(557). *Phys. Rev. B*, 79(15):155301, 2009.

[99] C. Kumpf, O. Bunk, J. H. Zeysing, Y. Su, M. Nielsen, R. L. Johnson, R. Feidenhans'l, and K. Bechgaard. Low-temperature structure of indium quantum chains on silicon. *Phys. Rev. Lett.*, 85(23):4916–4919, 2000.

[100] J. Wang, Huasheng Wu, Ricky So, Y. Liu, M. H. Xie, and S. Y. Tong. Structure determination of indium-induced Si(111)-In-4×1 surface by LEED patterson inversion. *Phys. Rev. B*, 72(24):245324, 2005.

[101] G. Lee, S.-Y. Yu, H. Kim, J.-Y. Koo, H.-I. Lee, and D. W. Moon. Absolute In coverage and bias-dependent STM images of the Si(111)4×1-In surface. *Phys. Rev. B*, 67(3):035327, 2003.

[102] T. Shibasaki, N. Nagamura, T. Hirahara, H. Okino, S. Yamazaki, W. Lee, H. Shim, R. Hobara, I. Matsuda, G. Lee, and S. Hasegawa. Phase transition temperatures determined by different experimental methods: Si(111)-4×1-In surface with defects. *Phys. Rev. B*, 81(3):035314, 2010.

[103] T. Abukawa, M. Sasaki, F. Hisamatsu, T. Goto, T. Kinoshita, A. Kakizaki, and S. Kono. Surface electronic structure of a single-domain Si(111)-4×1-In surface: a synchrotron radiation photoemission study. *Surface Science*, 325(1-2):33 – 44, 1995.

[104] J. R. Ahn, J. H. Byun, H. Koh, E. Rotenberg, S. D. Kevan, and H. W. Yeom. Mechanism of gap opening in a triple-band Peierls system: In atomic wires on Si. *Phys. Rev. Lett.*, 93(10):106401, 2004.

[105] S. Chandola, K. Hinrichs, M. Gensch, N. Esser, S. Wippermann, W. G. Schmidt, F. Bechstedt, K. Fleischer, and J. F. McGilp. Structure of Si(111)-In nanowires determined from the midinfrared optical response. *Phys. Rev. Lett.*, 102(22):226805, 2009.

[106] A. A. Stekolnikov, K. Seino, F. Bechstedt, S. Wippermann, W. G. Schmidt, A. Calzolari, and M. Buongiorno Nardelli. Hexagon versus trimer formation in In nanowires on Si(111): Energetics and quantum conductance. *Phys. Rev. Lett.*, 98(2):026105, 2007.

[107] C. González, F. Flores, and J. Ortega. Soft phonon, dynamical fluctuations, and a reversible phase transition: Indium chains on silicon. *Phys. Rev. Lett.*, 96(13):136101, 2006.

[108] X. López-Lozano, A. Krivosheeva, A. A. Stekolnikov, L. Meza-Montes, C. Noguez, J. Furthmüller, and F. Bechstedt. Reconstruction of *quasi*-one-dimensional In/Si(111) systems: Charge- and spin-density waves versus bonding. *Phys. Rev. B*, 73(3):035430, 2006.

[109] J.D. O'Mahony, J.F. McGilp, F.M. Leibsle, P. Weightman, and C.F.J. Flipse. Control of terrace width and atomic step distribution on vicinal Si(111) surfaces by thermal processing. *Semiconductor Science and Technology*, 8(4):495 – 501, 1993.

[110] C. Herring. Some theorems on free energies of crystal surfaces. *Physical Review*, 82(1):87 – 93, 1951.

[111] B.S. Swartzentruber, Y.-W. Mo, M.B. Webb, and M.G. Lagally. Scanning tunneling microscopy studies of structural disorder and steps on Si surfaces. volume 7, pages 2901 – 5, 1989.

[112] H. Hibino and T. Ogino. Transient step bunching on a vicinal Si(111) surface. *Phys. Rev. Lett.*, 72(5):657–660, 1994.

[113] A. V. Latyshev, H. Minoda, Y. Tanishiro, and K. Yagi. Electromigration and gold-induced step bunching on the Si(111) surface. *Surface Science*, 401(1):22 – 33, 1998.

[114] S. Stoyanov. Electromigration induced step bunching on Si surfaces – how does it depend on the temperature and heating current direction? *Japanese Journal of Applied Physics*, 30(Part 1, No. 1):1–6, 1991.

[115] T. Satō. Spectral emissivity of silicon. *Japanese Journal of Applied Physics*, 6(3):339–347, 1967.

[116] A. Kirakosian, R. Bennewitz, J.N. Crain, Th. Fauster, J.-L. Lin, D.Y. Petrovykh, and F.J. Himpsel. Atomically accurate Si grating with 5.73 nm period. *Applied Physics Letters*, 79(11):1608 – 10, 2001.

[117] D.-H. Oh, M. K. Kim, J. H. Nam, I. Song, C.-Y. Park, S. H. Woo, H.-N. Hwang, C. C. Hwang, and J. R. Ahn. Atomic structure model of the reconstructed Si(557) surface with a triple step structure: Adatom-parallel dimer model. *Phys. Rev. B*, 77(15):155430, 2008.

[118] J. B. Pendry. *Low Energy Electron Diffraction*. Academic, New York, 1974.

[119] F. Moresco, M. Rocca, T. Hildebrandt, and M. Henzler. Growth of ultrathin nanostructured Ag films on Si(111)7 × 7: a SPA-LEED study. *Surface Science*, 463(1):22 – 8, 2000.

[120] V.L. Berkovits, I.V. Makarenko, T.A. Minashvili, and V.I. Safarov. Optical transitions on GaAs(110) surface. *Solid State Communications*, 56(5):449 – 450, 1985.

[121] D. E. Aspnes and A. A. Studna. Reflectance-difference spectroscopy of (110) GaAs and InP. *Journal of Vacuum Science & Technology A: Vacuum, Surfaces, and Films*, 5(4):546–9, 1987.

[122] I. Bozovic, K. Char, S. J. B. Yoo, A. Kapitulnik, M. R. Beasley, T. H. Geballe, Z. Z. Wang, S. Hagen, N. P. Ong, D. E. Aspnes, and M. K. Kelly. Optical anisotropy of $YBa_2Cu_3O_{7-x}$. *Phys. Rev. B*, 38(7):5077–80, 1988.

[123] D. E. Aspnes, J. P. Harbison, A. A. Studna, and L. T. Florez. Application of reflectance difference spectroscopy to molecular-beam epitaxy growth of GaAs and AlAs. *Journal of Vacuum Science & Technology A: Vacuum, Surfaces, and Films*, 6(3):1327–32, 1988.

[124] D. E. Aspnes, J. P. Harbison, A. A. Studna, and L. T. Florez. Optical reflectance and electron diffraction studies of molecular-beam-epitaxy growth transients on GaAs(001). *Phys. Rev. Lett.*, 59(15):1687–90, 1987.

[125] Y. Sakuma, K. Kodama, and M. Ozeki. Atomic layer epitaxy of GaP and elucidation for self-limiting mechanism. *Applied Physics Letters*, 56(9):827–9, 1990.

[126] S. M. Koch, O. Acher, F. Omnes, M. Defour, M. Razeghi, and B. Drévillon. In situ investigation of InAs metalorganic chemical vapor deposition growth using reflectance anisotropy. *Journal of Applied Physics*, 68(7):3364–9, 1990.

[127] D. E. Aspnes, J. P. Harbison, A. A. Studna, and L. T. Florez. Reflectance-difference spectroscopy system for real-time measurements of crystal growth. *Applied Physics Letters*, 52(12):957–9, 1988.

[128] J. P. Harbison, D. E. Aspnes, A. A. Studna, L. T. Florez, and M. K. Kelly. Oscillations in the optical response of (001)GaAs and AlGaAs surfaces during crystal growth by molecular beam epitaxy. *Applied Physics Letters*, 52(24):2046–8, 1988.

[129] B. Sheridan, D. S. Martin, J. R. Power, S. D. Barrett, C. I. Smith, C. A. Lucas, R. J. Nichols, and P. Weightman. Reflection anisotropy spectroscopy: A new probe for the solid-liquid interface. *Phys. Rev. Lett.*, 85(21):4618–21, 2000.

[130] D. S. Martin, R. J. Cole, and P. Weightman. Effects of ion bombardment on the optical and electronic properties of Cu(110). *Phys. Rev. B*, 72(3), 2005.

[131] D. S. Martin, A. Maunder, and P. Weightman. Thermal behavior of the Cu(110) surface studied by reflection anisotropy spectroscopy and scanning tunneling microscopy. *Phys. Rev. B*, 63(15):155403, 2001.

[132] D. S. Martin, N. P. Blanchard, and P. Weightman. The effect of surface morphology upon the optical response of Au(110). *Surface Science*, 532-535:1 – 7, 2003.

[133] L. D. Sun, M. Hohage, P. Zeppenfeld, R. E. Balderas-Navarro, and K. Hingerl. Enhanced optical sensitivity to adsorption due to depolarization of anisotropic surface states. *Phys. Rev. Lett.*, 90(10):106104, 2003.

[134] Ph. Hofmann, K. C. Rose, V. Fernandez, A. M. Bradshaw, and W. Richter. Study of surface states on Cu(110) using optical reflectance anisotropy. *Phys. Rev. Lett.*, 75(10):2039–42, 1995.

[135] J. Bremer, J. K. Hansen, K. Stahrenberg, and T. Worren. The influence of surface steps on the optical and electronic anisotropy of Ag(110). *Surface Science*, 459(1-2):39 – 48, 2000.

[136] Z. Sobiesierski, D.I. Westwood, and C.C. Matthai. Aspects of reflectance anisotropy spectroscopy from semiconductor surfaces. *Journal of Physics: Condensed Matter*, 10(1):1 – 43, 1998.

[137] R. Forker and T. Fritz. Optical differential reflectance spectroscopy of ultrathin epitaxial organic films. *Physical Chemistry Chemical Physics*, 11(13):2142 – 55, 2009.

[138] R. Passmann, P. Favero, W. G. Schmidt, R. Miotto, W. Braun, W. Richter, M. Kneissl, N. Esser, and P. Vogt. Adsorption structure of cyclopentene on InP(001)-2 × 4. *Phys. Rev. B*, 80(12):125303, 2009.

[139] T. Yasuda, L. Mantese, U. Rossow, and D. E. Aspnes. Surface-induced optical anisotropies of single-domain (2×1) reconstructed (001) Si and Ge surfaces. *Phys. Rev. Lett.*, 74(17):3431–4, 1995.

[140] G. Bussetti, C. Goletti, P. Chiaradia, and G. Chiarotti. Infrared reflectance anisotropy spectroscopy of Si(111) - 2×1 : Surface excitons and polarons. *Phys. Rev. B*, 72(15):153316, 2005.

[141] G. Bussetti, C. Goletti, P. Chiaradia, and T. Derry. Optical gap between dangling-bond states of a single-domain diamond C(111)-2 × 1 by reflectance anisotropy spectroscopy. *Europhysics Letters*, 79(5):57002, 2007.

[142] F. Pedreschi, J. D. O'Mahony, P. Weightman, and J. R. Power. Evidence of electron confinement in the single-domain 4 × 1-In superstructure on vicinal Si(111). *Applied Physics Letters*, 73(15):2152–4, 1998.

[143] J. Jacob, N. McAlinden, K. Fleischer, S. Chandola, and J.F. McGilp. Reflectance anisotropy studies of 5 × 2-Au structures grown on Si(111) surfaces with different step formations. *Physica Status Solidi C*, 5(8):2569 – 72, 2008.

[144] L. F. Lastras-Martínez, M. Chavira-Rodríguez, R. E. Balderas-Navarro, J. M. Flores-Camacho, and A. Lastras-Martínez. Reflectance difference spectroscopy of GaAs(001) under a [110] uniaxial stress. *Phys. Rev. B*, 70(3):035306, 2004.

[145] D. Papadimitriou and W. Richter. Highly sensitive strain detection in silicon by reflectance anisotropy spectroscopy. *Phys. Rev. B*, 72(7):075212, 2005.

[146] E. Liarokapis, D. Papadimitriou, J. Rumberg, and W. Richter. Raman and ras measurements on uniaxially strained thin semiconductor layers. *Physica Status Solidi B*, 211(1):309 – 16, 1999.

[147] C. G. Tang, Y. H. Chen, X. L. Ye, Z. G. Wang, and W. F. Zhang. Strain-induced in-plane optical anisotropy in (001) GaAs/AlGaAs superlattice studied by reflectance difference spectroscopy. *Journal of Applied Physics*, 100(11):113122, 2006.

[148] J.D.E. McIntyre and D.E. Aspnes. Differential reflection spectroscopy of very thin surface films. *Surface Science*, 24(2):417 – 434, 1971.

[149] F. Manghi, R. Del Sole, A. Selloni, and E. Molinari. Anisotropy of surface optical properties from first-principles calculations. *Phys. Rev. B*, 41(14):9935–46, 1990.

[150] U. Rossow, L. Mantese, and D. E. Aspnes. Interpretation of surface-induced optical anisotropy of clean, hydrogenated, and oxidized vicinal silicon surfaces investigated by reflectance-difference spectroscopy. volume 14, pages 3070–3074, 1996.

[151] J. R. Power and P. Weightman. Au-induced superstructure formation on vicinal Si(001) studied by low-energy electron diffraction and reflectance anisotropy spectroscopy. *Phys. Rev. B*, 58(16):10532–39, 1998.

[152] F. Bechstedt and R. Del Sole. Analytical treatment of band-gap underestimates in the local-density approximation. *Phys. Rev. B*, 38(11):7710–6, 1988.

[153] A. I. Shkrebtii and R. Del Sole. Microscopic calculation of structure and optical properties of Ge(001)c4 $\times$ 2. *Surface Science*, 331-333(Part 2):1288 – 1293, 1995.

[154] P. Hohenberg and W. Kohn. Inhomogeneous electron gas. *Phys. Rev.*, 136(3B):B864–B871, 1964.

[155] Zachary H. Levine and Douglas C. Allan. Linear optical response in silicon and germanium including self-energy effects. *Phys. Rev. Lett.*, 63(16):1719–22, 1989.

[156] Lars Hedin. New method for calculating the one-particle green's function with application to the electron-gas problem. *Phys. Rev.*, 139(3A):A796–A823, 1965.

[157] P. H. Hahn, W. G. Schmidt, and F. Bechstedt. Bulk excitonic effects in surface optical spectra. *Phys. Rev. Lett.*, 88(1):016402, 2001.

[158] W. G. Schmidt, S. Glutsch, P. H. Hahn, and F. Bechstedt. Efficient $\sigma(n^2)$ method to solve the Bethe-Salpeter equation. *Phys. Rev. B*, 67(8):085307, 2003.

[159] M. Palummo, N. Witkowski, O. Pluchery, R. Del Sole, and Y. Borensztein. Reflectance-anisotropy spectroscopy and surface differential reflectance spectra at the Si(100) surface: Combined experimental and theoretical study. *Phys. Rev. B*, 79(3):035327, 2009.

[160] W.G. Schmidt. Calculation of reflectance anisotropy for semiconductor surface exploration. *Physica Status Solidi B*, 242(13):2751 – 64, 2005.

[161] W. G. Schmidt, F. Bechstedt, and J. Bernholc. Terrace and step contributions to the optical anisotropy of Si(001) surfaces. *Phys. Rev. B*, 63(4):045322, 2001.

[162] W. G. Schmidt, N. Esser, A. M. Frisch, P. Vogt, J. Bernholc, F. Bechstedt, M. Zorn, Th. Hannappel, S. Visbeck, F. Willig, and W. Richter. Understanding reflectance anisotropy: Surface-state signatures and bulk-related features in the optical spectrum of InP(001)2 $\times$ 4. *Phys. Rev. B*, 61(24):R16335–R16338, 2000.

[163] C. B. Collins, R. O. Carlson, and C. J. Gallagher. Properties of gold-doped silicon. *Phys. Rev.*, 105(4):1168–73, 1957.

[164] E. A. Taft and F. Hubbard Horn. Gold as a donor in silicon. *Phys. Rev.*, 93(1):64, 1954.

[165] T. Markussen, R. Rurali, X. Cartoixà, A.-P. Jauho, and M. Brandbyge. Scattering cross section of metal catalyst atoms in silicon nanowires. *Phys. Rev. B*, 81(12):125307, 2010.

[166] T. Bozhi, Z. Xiaolin, T.J. Kempa, F. Ying, Y. Nanfang, Y. Guihua, H. Jinlin, and C.M. Lieber. Coaxial silicon nanowires as solar cells and nanoelectronic power sources. *Nature*, 449(7164):885 – 9, 2007.

[167] H E Bishop and J C Rivire. Segregation of gold to the silicon (111) surface observed by Auger emission spectroscopy and by LEED. *Journal of Physics D: Applied Physics*, 2(12):1635, 1969.

[168] H Lipson and K E Singer. Disorder in a film of gold deposited on silicon: investigation by low-energy electron diffraction. *Journal of Physics C: Solid State Physics*, 7(1):12, 1974.

[169] P. Perfetti, S. Nannarone, F. Patella, C. Quaresima, A. Savoia, F. Cerrina, and M. Capozi. Energy loss spectroscopy (ELS) on the Si-Au system. *Solid State Communications*, 35(2):151 – 153, 1980.

[170] D. Grozea, E. Bengu, and L. D. Marks. Surface phase diagrams for the Ag-Ge(111) and Au-Si(111) systems. *Surface Science*, 461(1-3):23 – 30, 2000.

[171] S. M. Durbin, L. E. Berman, B. W. Batterman, and J. M. Blakely. X-ray standing-wave determination of surface structure: Au on Si(111). *Phys. Rev. B*, 33(6):4402–4405, 1986.

[172] L. E. Berman, B. W. Batterman, and J. M. Blakely. Structure of submonolayer gold on silicon (111) from X-ray standing-wave triangulation. *Phys. Rev. B*, 38(8):5397–5405, 1988.

[173] Y. Yabuuchi, F. Shoji, K. Oura, and T. Hanawa. Surface structure of the Si(111)-5×1-Au studied by low-energy ion scattering spectroscopy. *Surface Science Letters*, 131(2-3):L412 – L418, 1983.

[174] Ch. Schamper, W. Moritz, H. Schulz, R. Feidenhansĺ, M. Nielsen, F. Grey, and R. L. Johnson. Static lattice distortions and the structure of Au/Si(111)-(5×1): An x-ray-diffraction study. *Phys. Rev. B*, 43(14):12130–12133, 1991.

[175] J. D. O'Mahony, J. F. McGilp, C. F. J. Flipse, P. Weightman, and F. M. Leibsle. Nucleation and evolution of the Au-induced 5×2 structure on vicinal Si(111). *Phys. Rev. B*, 49(4):2527–2535, 1994.

[176] T. Hasegawa, K. Takata, S. Hosaka, and S. Hosoki. Au-induced reconstructions of the Si(111) surface. *Journal of Vacuum Science & Technology A: Vacuum, Surfaces, and Films*, 8(1):241–4, 1990.

[177] E. Bauer. The Si(111)-(5×1) Au structure. *Surface Science*, 250(1-3):L379 – L382, 1991.

[178] Y. Tanishiro, K. Yagi, and K. Takayanagi. Gold adsorption processes on Si(111)7×7 studied by in-situ reflection electron microscopy. *Surface Science*, 234(1-2):37 – 42, 1990.

[179] S. Riikonen and D. Sánchez-Portal. First-principles study of the atomic and electronic structure of the Si(111) - (5×2) -Au surface reconstruction. *Phys. Rev. B*, 71(23):235423, 2005.

[180] H. S. Yoon, S. J. Park, J. E. Lee, C. N. Whang, and I.-W. Lyo. Novel electronic structure of inhomogeneous quantum wires on a Si surface. *Phys. Rev. Lett.*, 92(9):096801, 2004.

[181] E. Bussmann, S. Bockenhauer, F. J. Himpsel, and B. S. Swartzentruber. One-dimensional defect-mediated diffusion of Si adatoms on the Si(111)-5×2-Au surface. *Phys. Rev. Lett.*, 101(26):266101, 2008.

[182] K. Sakamoto and R. I. G. Uhrberg. Atomic and electronic structures of metal induced Si(111)-(3×1) reconstructed surfaces. *e-Journal of Surface Science and Nanotechnology*, 2:210–221, 2004.

[183] S. C. Erwin and H. H. Weitering. Theory of the "honeycomb chain-channel" reconstruction of M/Si(111)- (3×1). *Phys. Rev. Lett.*, 81(11):2296–2299, 1998.

[184] Y. L. Wang, H.-J. Gao, H. M. Guo, H. W. Liu, I. G. Batyrev, W. E. McMahon, and S. B. Zhang. Tip size effect on the appearance of a STM image for complex surfaces: Theory versus experiment for Si(111)-7×7. *Phys. Rev. B*, 70(7):073312, 2004.

[185] L. Seehofer, S. Huhs, G. Falkenberg, and R. L. Johnson. Gold-induced facetting of Si(111). *Surface Science*, 329(3):157 – 166, 1995.

[186] M. Shibata, I. Sumita, and M. Nakajima. Scanning-tunneling-microscopy study of initial stages of Au adsorption on vicinal Si(111) surfaces. *Phys. Rev. B*, 53(7):3856–3860, 1996.

[187] M. Shibata, I. Sumita, and M. Nakajima. Quantization of Au-adsorbed 5×2 domains on vicinal Si(111). *Phys. Rev. B*, 57(4):2310–2314, 1998.

[188] M. Jaochowski, M. Strozak, and R. Zdyb. Gold-induced ordering on vicinal Si(111). *Surface Science*, 375(2-3):203 – 209, 1997.

[189] R. Zdyb, M. Strozak, and M. Jaochowski. Gold-induced faceting on Si(5 3 3) surface studied by RHEED. *Vacuum*, 63(1-2):107 – 112, 2001.

[190] T. Yasuda, D. E. Aspnes, D. R. Lee, C. H. Bjorkman, and G. Lucovsky. Optical anisotropy of singular and vicinal Si–Sio_2 interfaces and H-terminated Si surfaces. volume 12, pages 1152–1157, 1994.

[191] L.J. Pedri, L. Toppozini, and M.C. Gallagher. Au-induced nanofaceting and the stoichiometry of the Si(775)-Au surface. *Surface Science*, 601(4):924 – 930, 2007.

[192] T. Hasegawa and S. Hosoki. Intrarow diffusion of Au atoms in the Si(111)-5×2-Au structure. *Phys. Rev. B*, 54(15):10300–10303, 1996.

[193] A. Kirakosian, J. N. Crain, J. L. Lin, J. L. McChesney, D. Y. Petrovykh, F. J. Himpsel, and R. Bennewitz. Silicon adatoms on the Si(1 1 1)-5×2-Au surface. *Surface Science*, 532-535:928 – 933, 2003.

[194] C.-Y. Ren, S.-F. Tsay, and F.-C. Chuang. First-principles study of the atomic and electronic structure of the Si(111)-5×2-Au surface reconstruction. *Phys. Rev. B*, 76:075414, 2007.

[195] H. Okino, I. Matsuda, T. Tanikawa, and S. Hasegawa. Formation of facet structures by Au adsorption on vicinal Si(111) surfaces. *e-Journal of Surface Science and Nanotechnology*, 1, 2003.

[196] A. Pashkin, M. Dressel, M. Hanfland, and C. A. Kuntscher. Deconfinement transition and dimensional crossover in the Bechgaard-Fabre salts: Pressure- and temperature-dependent optical investigations. *Phys. Rev. B*, 81(12):125109, 2010.

[197] S. Wippermann and W.G. Schmidt. Optical anisotropy of the In/Si(111)-4×1/8×2 nanowire array. *Surface Science*, 603(1):247 – 250, 2009.

[198] K. Fleischer, L. Carroll, C. Smith, and J.F. McGilp. Optical reflectance anisotropy of buried Fe nanostructures on vicinal W(110). *Journal of Physics Condensed Matter*, 19(26), 2007.

[199] I. K. Robinson, P. A. Bennett, and F. J. Himpsel. Structure of quantum wires in Au/Si(557). *Phys. Rev. Lett.*, 88(9):096104, 2002.

[200] D. Snchez-Portal and R. M. Martin. First principles study of the Si(557)-Au surface. *Surface Science*, 532-535:655 – 660, 2003.

[201] T. Nagao, S. Yaginuma, T. Inaoka, and T. Sakurai. One-dimensional plasmon in an atomic-scale metal wire. *Phys. Rev. Lett.*, 97(11):116802, 2006.

[202] D. Sánchez-Portal, S. Riikonen, and R. M. Martin. Role of spin-orbit splitting and dynamical fluctuations in the Si(557)-Au surface. *Phys. Rev. Lett.*, 93(14):146803, 2004.

[203] K. C. Pandey. Reconstruction of semiconductor surfaces: Buckling, ionicity, and π-bonded chains. *Phys. Rev. Lett.*, 49(3):223–226, 1982.

[204] G. Chiarotti. Electronic surface states investigated by optical spectroscopy. *Surface Science*, 299-300:542 – 550, 1994.

[205] R. Zhachuk and S. Pereira. Comment on "Atomic structure model of the reconstructed Si(557) surface with a triple step structure: Adatom-parallel dimer model". *Phys. Rev. B*, 79(7):077401, 2009.

[206] M. Henzler and R. Zhachuk. The step structure of the Si(557) surface. *Thin Solid Films*, 428(1-2):129 – 132, 2003.

[207] S.A. Teys, K.N. Romanyuk, R.A. Zhachuk, and B.Z. Olshanetsky. Orientation and structure of triple step staircase on vicinal Si(111) surfaces. *Surface Science*, 600(21):4878 – 4882, 2006.

[208] A. N. Chaika, D. A. Fokin, S. I. Bozhko, A. M. Ionov, F. Debontridder, V. Dubost, T. Cren, and D. Roditchev. Regular stepped structures on clean Si(hhm)7 x 7 surfaces. *Journal of Applied Physics*, 105(3):034304, 2009.

[209] C. Hogan. *Ab initio* calculations of the optical response of si(557) and si(775). unpublished work, 2010.

[210] P. Giannozzi, S. Baroni, N. Bonini, M. Calandra, R. Car, C. Cavazzoni, D. Ceresoli, G. L. Chiarotti, M. Cococcioni, I. Dabo, A. Dal Corso, S. de Gironcoli, S. Fabris, G. Fratesi, R. Gebauer, U. Gerstmann, C. Gougoussis, A. Kokalj, M. Lazzeri, L. Martin-Samos, N. Marzari, F. Mauri, R. Mazzarello, S. Paolini, A. Pasquarello, L. Paulatto, C. Sbraccia, S. Scandolo, G. Sclauzero, A. P. Seitsonen, A. Smogunov, P. Umari, and R. M. Wentzcovitch. QUANTUM ESPRESSO: A modular and open-source software project for quantum simulations of materials. *Journal of Physics: Condensed Matter*, 21(39):395502, 2009.

[211] A. Marini, C. Hogan, M. Gruning, and D. Varsano. YAMBO: An *ab initio* tool for excited state calculations. *Computer Physics Communications*, 180(8):1392 – 1403, 2009.

[212] C. Hogan, R. Del Sole, and G. Onida. Optical properties of real surfaces from microscopic calculations of the dielectric function of finite atomic slabs. *Phys. Rev. B*, 68(3):035405, 2003.

[213] R. Del Sole and R. Girlanda. Optical properties of semiconductors within the independent-*quasi*particle approximation. *Phys. Rev. B*, 48(16):11789–11795, 1993.

[214] D Wall, S Sindermann, K R Roos, M Horn von Hoegen, and F-J Meyer zu Heringdorf. The influence of anisotropic diffusion on Ag nanowire formation. *Journal of Physics: Condensed Matter*, 21(31):314023, 2009.

[215] M. Jalochowski, M. Strozak, and R. Zdyb. Optical reflectivity of ultrathin Pb layers and the quantum size effect. volume 31, pages 291 – 300, 1998.

[216] M. Jalochowski, M. Strozak, and R. Zdyb. Anomalous optical absorption in ultrathin Pb films. *Phys. Rev. B*, 66(20):205417, 2002.

[217] M. Jalochowski, M. Strzak, and R. Zdyb. Reflectance anisotropy during growth of Pb nanowires on well ordered Si(3 3 5) surface. *Applied Surface Science*, 211(1-4):209 – 215, 2003.

[218] L. B Scaffardi and J. O Tocho. Size dependence of refractive index of gold nanoparticles. *Nanotechnology*, 17(5):1309, 2006.

[219] U. Kreibig and C. v. Fragstein. The limitation of electron mean free path in small silver particles. *Zeitschrift fr Physik A Hadrons and Nuclei*, 224:307–323, 1969.

[220] C. G. Granqvist and O. Hunderi. Optical properties of ultrafine gold particles. *Phys. Rev. B*, 16(8):3513–3534, 1977.

[221] M. M. Alvarez, J. T. Khoury, T. G. Schaaff, M. N. Shafigullin, I. Vezmar, and R. L. Whetten. Optical absorption spectra of nanocrystal gold molecules. *The Journal of Physical Chemistry B*, 101(19):3706–3712, 1997.

[222] P. Yang, H. Portalès, and M.-P. Pileni. Ability to discern the splitting between longitudinal and transverse plasmon resonances in Au compared to Ag nanoparticles in close-packed planar arrays. *Phys. Rev. B*, 81(20):205405, 2010.

[223] H. Hövel, S. Fritz, A. Hilger, U. Kreibig, and M. Vollmer. Width of cluster plasmon resonances: Bulk dielectric functions and chemical interface damping. *Phys. Rev. B*, 48(24):18178–18188, 1993.

[224] M. A. Ordal, L. L. Long, R. J. Bell, S. E. Bell, R. R. Bell, Jr. R. W. Alexander, and C. A. Ward. Optical properties of the metals Al, Co, Cu, Au, Fe, Pb, Ni, Pd, Pt, Ag, Ti, and W in the infrared and far infrared. *Appl. Opt.*, 22(7):1099–1119, 1983.

[225] Mie G. Beitrage zur optik trber medien speziell kolloidaler metallsungen. *Ann. Phys.*, 25:377445, 1908.

[226] U. Kreibig and M. Vollmer. *Optical Properties of Metal Clusters*, volume 25. Springer Series in Materials Science, 1995.

[227] D. Bedeaux and J. Vlieger. *Optical Properties of Surfaces.* World Scientific, 2^{nd} edition, 2004.

[228] K. L. Kelly, E. Coronado, L. L. Zhao, and G. C. Schatz. The optical properties of metal nanoparticles: The influence of size, shape, and dielectric environment. *The Journal of Physical Chemistry B*, 107(3):668–677, 2003.

[229] A. Sihvola. *Electromagnetic mixing formulas and spplications.* Electromagnetic waves series. IEE.

[230] C. Beitia, Y. Borensztein, R. Lazzari, J. Nieto, and R. G. Barrera. Substrate-induced multipolar resonances in supported free-electron metal spheres. *Phys. Rev. B*, 60(8):6018–6022, 1999.

[231] A. Pinchuk, A. Hilger, G. von Plessen, and U. Kreibig. Substrate effect on the optical response of silver nanoparticles. *Nanotechnology*, 15(12):1890, 2004.

[232] T. Yamaguchi, S. Yoshida, and A. Kinbara. Optical effect of the substrate on the anomalous absorption of aggregated silver films. *Thin Solid Films*, 21(1):173 – 187, 1974.

[233] T. Yamaguchi, S. Yoshida, and A. Kinbara. Effect of the dipole interaction between island particles on the optical properties of an aggregated silver film. *Thin Solid Films*, 13(2):261 – 264, 1972.

[234] F. Neubrech, T. Kolb, R. Lovrincic, G. Fahsold, A. Pucci, J. Aizpurua, T. W. Cornelius, M. E. Toimil-Molares, R. Neumann, and S. Karim. Resonances of individual metal nanowires in the infrared. *Applied Physics Letters*, 89(25):253104, 2006.

[235] L. Novotny. Effective wavelength scaling for optical antennas. *Phys. Rev. Lett.*, 98(26):266802, 2007.

[236] A. Pucci, F. Kost, G. Fahsold, and M. Jalochowski. Infrared spectroscopy of Pb layer growth on Si(111). *Phys. Rev. B*, 74(12):125428, 2006.

[237] H. V. Chung, M. Klevenz, R. Lovrincic, F. Neubrech, O. Skibbe, A. Pucci, P. Nita, M. Jalochowski, and T. Nagao. Studies on gold atom chains and lead nanowires on silicon vicinal surfaces. *Journal of Physics: Conference Series*, 187(1):012025, 2009.

[238] M.A. Yurkin and A.G. Hoekstra. The discrete dipole approximation: An overview and recent developments. *Journal of Quantitative Spectroscopy and Radiative Transfer*, 106(1-3):558 – 589, 2007.

[239] R. C. Jones. A new calculus for the treatment of optical systems. *J. Opt. Soc. Am.*, 31(7):488–493, 1941.

[240] H. Hurwitz Jr. and R. C. Jones. A new calculus for the treatment of optical systems. *J. Opt. Soc. Am.*, 31(7):493–495, 1941.